People's Democratic Republic of Algeria
Ministry of Higher Education and Scientific Research
University of Oum El Bouaghi
Faculty of: Exact Sciences and Nature and Life Sciences

Thesis

Presented to obtain

3rdCycle Doctorate

Branch: Matter Sciences

Specialty: Materials Physics

Title :

Elaboration by " spray pyrolysis " and characterization of thin films of zinc oxide (ZnO) and study of the doping effect on photocatalytic efficiency for water depollution.

Presented by :
Loubna HAFSA

Publicly defended on 01/02/2024 in front of the following committee members:

N°	First and last name	Grade	University	Quality
01	Louardi Remache	Prof.	Univ. Larbi Ben M'hidi - Oum El Bouaghi	President
02	Lazhar Hadjeris	Prof.	Univ. Larbi Ben M'hidi - Oum El Bouaghi	Supervisor
03	Labidi Herissi	M.C.A	Univ. Larbi Tebessi–Tebessa.	Co-reporter
04	Nadhir Attaf	Prof.	Univ. Constantine 1 - Constantine	Examiner
05	Abdelkader Djelloul	Prof.	Univ. Abbes Laghrour - Khenchela	Examiner

Acknowledgements

*First, thank to **ALLAH** for his grace and for this help to let me completing my research thesis.*

*I would like to express my deepest gratitude to my advisor Prof. **Lazhar Hadjeris** for his continued support and guidance during my PhD studies, for his patience, motivation, enthusiasm, and immense knowledge. I attribute the level of my PhD degree to his encouragement and effort and without him this thesis, too, would not have been completed or written.*

*I would like also to thank my co. advisor Prof. **Labidi Herissi,** who has supported me throughout my thesis with his patience and knowledge. I have been amazingly fortunate to have a second advisor who gave me the freedom to explore on my PhD thesis and at the same time the guidance to recover when my steps faltered.*

*I would like to thank the director and the technical Group in LMSSEF laboratory. Special thanks to Mr. **Ali Djermane** for their constant help and expertise using XRD characterization technique.*

*I would like to thank Prof. **Foughali Lazhar** from ISTA laboratory for help and characterizing using SEM microscopy.*

*I would like to thank Prof. **Corinne Nouveau** from LaBoMap laboratory, Ecole Nationale des Arts et Métiers， Cluny Campus (France) for everything that I received in my time there, starting from respect, knowledge, and love .I would also like to thank the professors, all administration employees and technicals in LaBoMap Group laboratory, Special thanks to Mr. **Yoann Pinot** for their constant help, expertise and training in developing SEM images, EDX and Profilometer measurements.*

*I address my thanks to Prof. **Louardi Remache**., Prof. **Abdelkader Djelloul** and Prof. **Nadhir ATTAF** for their acceptance to judge this modest work.*

Last but not the least; I would like to thank my family: my parents, for supporting me spiritually throughout my life. I cannot forget my sisters, my brothers, my husband and all my friends.

Contents

Chapter 2. Characterization methods

Chapter 3. Experimental details

Chapter 4. Results and discussion

Figure caption

Table caption

General introduction

General introduction

The tendency to seek technological miniaturization of devices is associated with a reduction in manufacturing costs (smaller amounts of reagents, lower operating times, and lower power consumption) [1]. The use of materials in the form of thin films, therefore, has emerged as an alternative to fulfil these requirements. Thin films can be produced by a variety of processes. Spray-pyrolysis has many advantages. It requires only simple and inexpensive equipment and offers an easy way to add doping materials [2,3].

Nanostructure thin films have attracted considerable research interest over recent decades due to their potential applications in the fields of engineering, science and technology. However, developments in nanotechnology are dependent on the availability of new materials and the ability to design and synthesize new nanostructured materials. Nano-materials, defined as materials of less than 100 nm in one or more dimension, exhibit novel physical properties that are not possessed by bulk forms. Consequently, synthesis, characterization and application of Nanostructure thin films have been widely investigated in recent years [4].

Zinc oxide (ZnO) is a II–VI group semiconductor compound whose ionic nature resides at the borderline between covalent and ionic semiconductors [5]. It possesses promising catalytic, electrical, electronic, and optical properties [5]. The preparation and characterization of ZnO materials at nanometric scale, including the forms of nanowires, nanorods, nanobelts, and nanoparticles, have recently attracted considerable attention due to their physical properties and potential applications [6].The photocatalytic and the electronic properties of ZnO can be improved by doping with different materials such as metal oxide (Al).

Iron oxide in alpha-hematite form (α-Fe_2O_3)is an excellent photomaterial due to ease in synthesis, abundance in nature, low cost and favourable bandgap (~2.1 eV) that can absorb visible light (42% of sun radiations)[7]. The performance of alpha-hematite as photomaterial has been limited by low conductivity, the short electron-hole pair time (<10 ps) and hole diffusion length (2-4 nm), which cause high recombination rates of photo-generated carriers in the bulk [7]. Recent studies [8, 9] have identified that the doping process can enhance the morphology, structure, and shape of the material.

TiO_2 and ZnO, which are highly evaluated for UV photocatalysis, are inactive under visible light due to their wide bandgaps [10]. On the other hand, due to its absorption is in the visible region, hematite is a preferred photocatalytic material but it shows lower photocatalytic efficiency because of corrosion property [10].

The objectives of this thesis are the elaboration, using the ultrasonic spray pyrolysis technique (USP), of thin films of two metal oxides, namely zinc oxide and iron oxide, and to investigate their properties by:

- Comparing the structural, optical, morphological, electrical and photocatalytic properties of ZnO nanowires thin films with Fe_2O_3 thin films.
- Comparing the structural, optical, morphological, electrical and photocatalytic properties of ZnO nanowires thin films with ZnO nanorods thin films.
- Doping ZnO nanorods with transition metal materials such as aluminum (Al).

The outline of this dissertation can be summarized as follows.

Chapter 1 is a literature review that provides a brief overview of transparent conducting oxides (TCOs) properties and their applications. Structural, optical, morphological, thermal and electrical properties of zinc oxide (ZnO) and hematite (Fe_2O_3) materials are discussed for photocatalytic applications. Thin films synthesis by spray-pyrolysis technique and photocatalysis basic principles and its mechanism are also described.

Chapter 2 presents the characterisation techniques employed to examine the synthesised thin films and the methods used to determine some physical parameters from the characterisations results are explained.

Chapter 3 provides the synthesis process of the proposed thin films by using spray pyrolysis and the photocatalytic test conditions are described.

Lastly, Chapter 4 is devoted to the presentation and discussion of results obtained from three different comparative studies,

In the first study, titled “Comparative study between ZnO and Fe_2O_3 thin films”, we compare the structural, optical, morphological, and electrical properties of the sprayed ZnO (prepared with zinc acetate dihydrate precursor) and Fe_2O_3thin films in detail. Then the photocatalytic activity properties of these thin films has been evaluated, by studying the degradation of the methyl green (MG) as a polluting model.

In the second study, titled “Comparative study between ZnO nanowires and ZnO nanorods thin films”, we compare the structural, optical, morphological, and electrical properties of the sprayed ZnO nanowires and ZnO nanorods thin films prepared with different precursors (zinc acetate dihydrate precursor forming ZnO nanowires thin films and zinc chloride precursor forming ZnO nanorods thin films). Then the photocatalytic activity a

property of these thin films has been evaluated by studying the degradation of the same polluting (MG) mentioned above.

Finally, in the third study, titled “Comparative study between undoped ZnO nanorods and 5% Al doped ZnO nanorods thin films», we compare the structural, optical, morphological, and electrical properties of the sprayed undoped ZnO nanorods and 5% Al doped ZnO thin films. Then the photocatalytic activity properties of these thin films has been evaluated, by studying the degradation of the same polluting (MG) mentioned above.

The general conclusion of this thesis summarizes the different results of this research study using the synthesis thin films for photocatalysis applications and some prospects for future development of this research work are proposed.

References of general introduction

[1] A.K. Alves, C.P. Bergmann, F.A. Berutti, Novel synthesis and characterization of nanostructured materials. Engineering materials Book, 1612-1317, Porto Alegre Brazil (August 2013).

[2] D. Perednis, Thin film deposition by spray pyrolysis and the application in solide oxide fuel cells. Ph.D. Thesis, Swiss Federal Institute of Technology Zurich (2003)

[3] L. Hadjeris, L. Herissi, M B. Assouar, T. Easwarakhanthan, J. Bougdira, N. Attaf, M. S. Aida, Transparent and conducting ZnO films grown by spray pyrolysis, Semicond. Sci. Technol. 24 (2009) 035006 (6pp), (2009).

[4] Almeida. T. P, Hydrothermal synthesis and characterisation of α-Fe_2O_3nanorods, Ph.D. Thesis, University of Nottingham (2010).

[5] Morkoc .H, Özgür. U, Zinc oxide: fundamentals, materials and device technology. Wiley-VCH, Weinheim, Germany (2009)

[6] Gomez. JL, Tigli. O, Zinc oxide nanostructures: from growth to application. J Mater Sci 48:612–624. (2013).

[7] H. Alrobei, Synthesis and characterization of alpha-hematite nanomaterials for water-splitting applications. USF Tampa Graduate Theses and Dissertations (2018).

[8] N. Basavegowda, K. Mishra, Y.R. Lee, Synthesis, characterization, and catalytic applications of hematite (α-Fe_2O_3) nanoparticles as reusable nanocatalyst. Advances in Natural Sciences: Nanoscience and Nanotechnology, 2017. 8(2): p. 025017 (2017).

[9] Liu, J., et al., General strategy for doping impurities (Ge, Si, Mn, Sn, Ti) in hematite nanocrystals. The Journal of Physical Chemistry c, 2012. 116(8): p. 4986-4992 (2012).

[10] Fox .MA, Dulay .MT, Heterogeneous photocatalysis. Chem Rev 93(1):341–357 (1993).

Chapter 1

Literature review of TCOs

1.1 Introduction

The main core of this chapter provides a brief overview of transparent conducting oxides (TCOs) properties and their applications and presents the description of ZnO and Fe_2O_3 physical properties. We need to know more about the general properties of these materials. We therefore present on the one hand, a general point of view on zinc oxide "ZnO" and iron oxide "Fe_2O_3", their crystalline, morphological, optical, electrical properties and on the other hand the spray-pyrolysis deposition techniques for thin films formation mechanisms. Finally, we present the photocatalytic method and its basic principles, mechanism, limitations and operating parameters such as the doping effect on the photocatalytic processes.

1.2 Transparent conducting oxides

1.2.1 Introduction

Transparent Conducting Oxides (TCOs) are a unique class of materials that exhibit both transparency and electronic conductivity simultaneously. These materials have found wide spread use in displays, photovoltaics, low-emittance windows, and flexible electronics [1]. In these applications, the role as transparent contacts is enabled by the TCO's. However, increasingly, the demands required extend beyond the combination of conductivity and transparency, where indeed higher performance is needed, but now include work function, morphology, processing and patterning requirements, long term stability, lower cost and elemental abundance/green materials [1]. As these needs have begun to emerge over the last 5 years they have stimulated a dramatic resurgence of research in the field leading to many new materials and processes [2]. The remarkable applications dependent on these materials have continued to make sweeping strides. These include the advent of larger flat screen high-definition televisions (HDTVs including LCD, Plasma and OLED based displays), larger and higher-resolution flat screens for portable computers, the increasing importance of energy-efficient low-emittance, solar control and electrochromic windows, a dramatic increase in the manufacturing of thin film photovoltaics (PV), the advent of oxide based transistors and transparent electronics as well as a plethora of new hand-held, flexible and smart devices, all with smart displays [3]. Driven by the increased importance and potential opportunities for TCO materials in these and other applications, there has been increasing activity in the science of these materials. This has resulted in new n-type materials, the synthesis of p-type materials and novel composite TCO materials as well as an increased set of theoretical and modelling tools for understanding and predicting the behaviour of TCOs. Considering that, over the last

20 years, much of the materials work on TCOs has been empirical with a focus on minor variants of ZnO, In_2O_3 and SnO_2; it is quite remarkable how dramatically this field has grown recently in both basic and applied science. This is reflected in the thousands of papers published over the last years. This may be a function of not only the need to achieve higher performance levels for these devices, but also of the increasing importance of transition-metal based oxides in devices in a broader sense including ferroelectric, piezoelectric, thermoelectric, gas sensing superconducting, Photocatalytics, and other materials applications [1].

Thus, in the last few years, there has been an increasing realization that the conventional TCO material set of substitutionally doped crystalline SnO_2, ZnO and In_2O_3 materials are no longer sufficient to meet the needs of all TCO applications. As is the case in many technological areas, this is a consequence of the acknowledgment of the limitations of the existing materials as well as a realization that new materials can open the way to new and improved devices. Amplifying this is the need for TCO materials with certain specific properties other than just high transparency and conductivity as applications are emerging where work function, surface roughness, nano-structure, thermal and chemical reactivity/diffusivity or ease of patterning are critical TCO functionalities [4].

1.2.2 Unique Properties of TCOs

TCOs are an essential part of technologies that requires both large-area electrical contact and optical access in the visible portion of the light spectrum. High transparency, combined with useful electrical conductivity ($>10^3 \Omega^{-1}$ cm^{-1}), is achieved by selecting a wide-bandgap oxide that is rendered degenerate through the introduction of native or substitutional dopants [5]. Most of the useful oxide-based materials are n-type conductors that ideally have a wide bandgap (3 eV), the ability to be doped to degeneracy, and a conduction band shape (dictating electron effective mass) that ensures that the plasma absorption edge lies in the infrared range. TCOs are also available and find use in specialized applications where ease of deposition, cost, or IR reflectivity is favoured over optimum optical transmission and minimum sheet resistance. For example, heat-efficient windows that reflect in the infrared range are created during the manufacture of architectural glass by means of the direct deposition of SnO_2 using chloride-based spray pyrolysis [6]. In this passive application, good electrical conductivity is sacrificed for IR reflectivity, high transparency in the visible regime, and processing convenience and economics. The production of energy-efficient architectural glass occurs in quantities measured in tens of square kilometres per year. This market is continuing to grow [6].

For optoelectronic applications, the transparent conductor must be carefully processed to maximize optical transmissivity in the visible regime, while achieving minimum electrical resistivity. Optimization of these properties will depend on the application, but in general, achieving the required performance in the as-deposited condition requires careful process control [7].

Furthermore, as the undeveloped world rapidly becomes more technological with the associated increasing energy needs and vehicular traffic, the total global energy consumption will continue to rise rapidly. One clear consequence of this is that global atmospheric CO_2 levels which are a major cause of global warming are increasing dramatically. In (figure 1.1), it is clear that the present on-going rapid increase in CO_2, which appears instantaneous on the 45,000 year time span of the graph, is significantly beyond any previous short term event in the history spanned by the (figure 1.1)[8, 9].

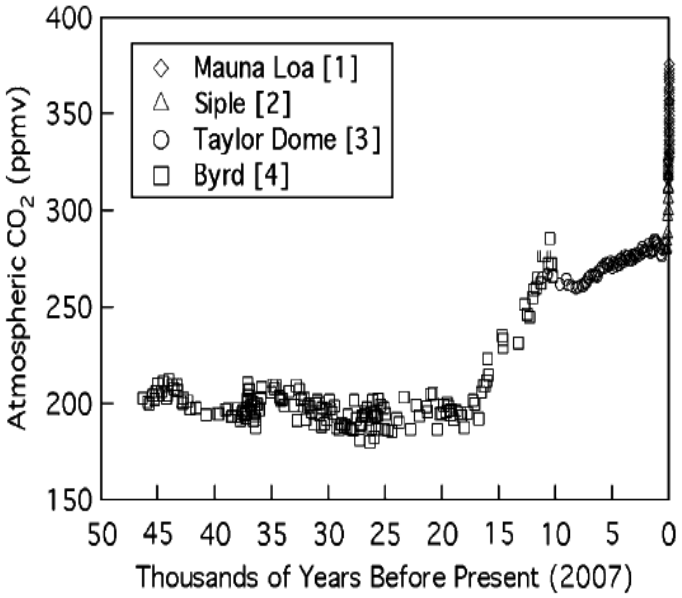

Figure 1.1: Atmospheric CO_2 vs. year.[9, 10]

TCOs are key elements in a number of "green" technologies. In particular, they are critical to low-e and solar control windows, photovoltaics, OLEDs for indoor lighting and vehicle heat management. Collectively, this combination of technologies which depend on TCO materials has the potential to significantly change the energy use balance by both enabling new energy generation technologies and improving energy efficiency technologies. Again, this provides further motivation to move to new TCO materials for less environmental impact, lower cost, sustainability and efficiency improvements in important devices [10].

1.3 Zinc oxide main properties

1.3.1 Introduction

Zinc oxide (ZnO) is a ceramic material and was used early in history, for instance as a precursor material for brass manufacturing in old china. ZnO occurs naturally as the mineral zincite (figure1.2). In 1810 it was discovered by Bruce in Franklin (New Jersey, USA) as red oxide of zinc, in 1845 named as zincite by Haidinger [11].It can be found at different places on earth: Franklin (New Jersey, USA), Sarawezza (Tuscany, Italy), Tsumeb (Namibia), Olkusz (Poland), Spain, Tasmania and Australia. Most of the natural crystals are small, but freely formed crystals up to25 mm were reported, which are exceedingly rare [12]. ZnO is composed of abundant elements; the abundances of Zn and O in the earth crust are 132 ppm and 49.4%, respectively. This is important for large-scale applications of ZnO, for instance as transparent electrodes in thin film solar cells or flat panel displays and an advantage compared to indium tin oxide (ITO), the dominant transparent electrode material today, wherein the metal In has an abundance in the earth crust of only 0.1 ppm [12].

Investigations on the electrical properties of ZnO date back to 1912, when Somerville measured the resistivity of ZnO rods up to a high temperature of about 1,125C [13]. The first electronic characterization of polycrystalline, bulk ZnO samples, of ZnO thin films and even of the first ZnO single crystals was performed by Fritsch in 1935 [14]. He showed that ZnO exhibits a strong thermal activation of the conductivity typical for a semiconductor. He also performed first Hall measurements on his ZnO samples and obtained Hall mobilities between 7 and30 cm^2/V and carrier concentrations in the range of 10^{18} cm^{-3}.Both, from the Hall as well as from Seebeck coefficient measurements he found, that ZnO is an n-type semiconductor [14].

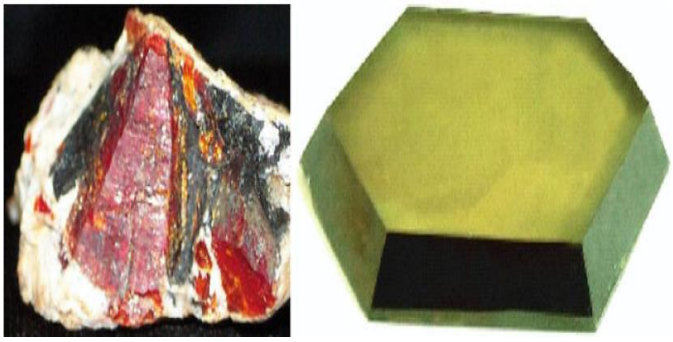

Figure 1.2: Photographs of (left) natural (red colored ZnO size) zinc oxide (zincite) in calcite (ZnO Franklin mineral museum, New Jersey, USA) and of (right) hydrothermally grown ZnO single crystals (Mineral Ltd., Alexandrov, Russia) [14].

After World War II, with the advent of the semiconductor industry, also ZnO was investigated as one of the first compound semiconductors. In the 1950s the ZnO research was focused in the United States at Bell Labs (Hutson, Lander, Thomas) and in Germany at the University of Erlangen (Mollwo,Heiland, Helbig). Hutson discovered the large piezoelectric effect of ZnO, which is higher than that of quartz [15]. This lead to one of the first applications of ZnO as a piezoelectric filter using the principle of surface-acoustic waves [16].

Zinc oxide is a II–VI group semiconductor compound whose ionic nature resides at the borderline between covalent and ionic semiconductors [17]. It possesses promising catalytic, electrical, electronic, and optical properties [17]. The preparation and characterization of ZnO materials at nanometric scale, including the forms of nanowires, nanobelts, and nanoparticles, have recently attracted considerable attention due to their physical properties and potential applications [18].

The common precursors for zinc oxide include inorganic salts such as zinc nitrate ($Zn\cdot(NO_3)_2$), organic compounds such as zinc acetate ($Zn\cdot(COOCH_3)_2$) (also written as ($Zn.(OAc)_2$) which is a carboxylate, the class of precursors most widely used), and zinc chloride ($Zn\cdot(Cl_2$).

1.3.2 Crystallographic structure

Zinc oxide is a semiconductor compound which crystallizes in the hexagonal wurtzite structure (P63mc) (figure 1.3.a), zinc blende (figure 1.3.b), and rock salt (or Rochelle salt) (figure 1.3.c), elucidated by Bragg already in 1914, shortly after the discovery of X-ray diffraction [17]. Under ambient conditions, the wurtzite symmetry is the most thermodynamically stable phase. The zinc blende structure can be stabilized only by growth on cubic substrates, and the rock salt or Rochelle salt (NaCl) structure may be obtained only at relatively high-pressure syntheses (9 GPa). In the hexagonal unit cell of ZnO, which contains two ZnO molecules, the Zn atoms are surrounded tetrahedrally by oxygen atoms. The Zn–O distances in c-direction(0.196 nm) are a little bit shorter than the distances to the other three oxygen atoms (0.198 nm).The ‘low-symmetry’ non polar faces with threefold coordinated atoms are the most stable ones, whereas the polar (002) faces show the highest surface energy, leading to higher growth rate of ZnO nanocrystals along the c-axis direction. Additionally, there is no center of inversion in the wurtzite crystal structure, and therefore an inherent asymmetry along the c-axis is present, allowing the anisotropic growth of the crystal along the [001] direction [19].

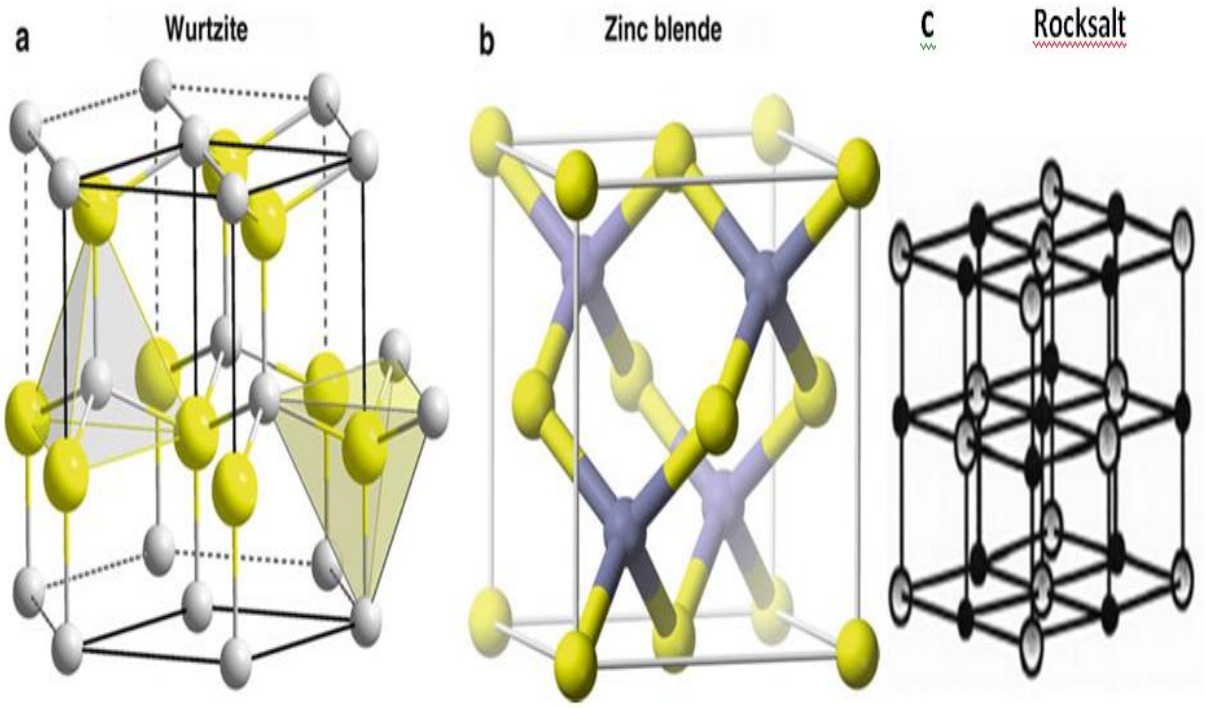

Figure *1*.3: ZnO different crystal structures [20].

Table 1.1: Zinc oxide Structural data [20].

Lattice (normal conditions)	Hexagonal, wurtzite (B4-type, P63mc)
Lattice constants	a=0.32498 nm, c=0.52066 nm, c/a=1.6021, u=0.3832
Density	5.67 g/cm^3, 4.2x10^{22}ZnO molecules/cm^3
Hardness	5 GPa
Bulk modulus [GPa]	142.4
Lattice (high pressure)	Cubic, NaCl (B1-type, Fm3m)

1.3.3 Classification of ZnO Nanostructures

From the morphological point of view, nanostructures can be categorized into four basic classes: (i) Zero-dimensional (0D) nanomaterials are materials whose all three dimensions are smaller than 100 nm like nanoparticles quantum dots (QDs). (ii) One-dimensional (1D) ones are materials whose only one dimension is bigger than 100 nm, (e.g., nanotubes, nanowires, and nanorods. (iii) Two-dimensional (2D) nanomaterials have two dimensions bigger than the upper limit of nanoscale such as nanofilms, nanolayers, and nanocoatings. (iv) Three-dimensional (3D) nanomaterials or bulk nanomaterials have no dimensions at nanoscale, but these 3D structures may consist of various nanostructures 3D (e.g., nanotetrapods, nanoflowers, nanopropellers and nanorings) [21]. The deposition and growth methods have a profound impact on morphology and can be engineered to fabricate novel structures. In particular, the morphology is highly dependent on three parameters: source material composition, growth temperatures, and diffusion rates [20].

1.3.3.1 Nanorods, Nanowires, and Nanotubes: Properties and Applications

One-dimensional nanomaterials refer to nanowires, nanorods, nanofibers, nanocables, nanotubes, nanobelts, etc (figure 1.4), which are elongated in one specific direction. Due to their unique optical and electronic properties, semiconducting ZnO nanowires or nanotubes are of crucial interest for the development of devices in nanoelectronics, chemical and biological sensing, energy conversion and storage (photovoltaic cells, batteries, capacitors, and hydrogen-storage devices), light-emitting diodes, catalysis, drug delivery, and piezoelectric energy nanogeneration [22, 23].

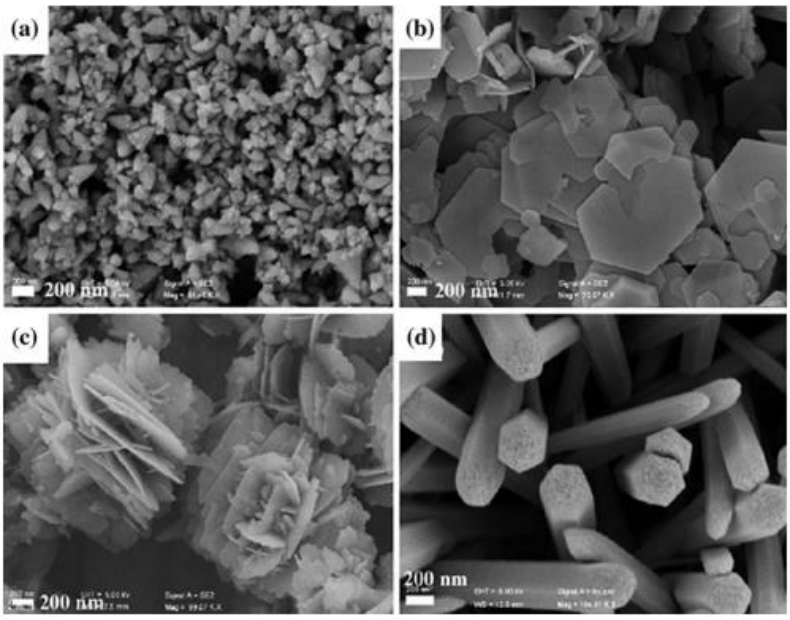

Figure *1*.4: Some different ZnO nanoarchitectures: nanoparticles (a), nanosheets (b), nanoflowers (c), and nanorods (d) [22].

1.3.4 Optical properties of ZnO

The natural color of zinc oxide is white but it displays pronounced changes in color when heated or when certain impurities are incorporated into the crystals. The refractive index of zinc oxide is about 2.008 in visible light and it is transparent in the infrared region between the wavelengths 1.5-15 μm [24]. Both dopant additions and heat treatment affect the wavelength and efficiency of luminescence. For example, after ZnO is chemically reduced with CO, it fluoresces a pale blue-green color under ultraviolet light, X-rays and cathode rays. Zinc oxide shows significant photoconductivity in the ultraviolet region and throughout most of the visible portion of the spectrum. With an incident light of 400 nm wavelength, about 200 electrons are generated by one incident photon [24].

Zinc oxide has an intrinsic band gap at room temperature of 3.37 eV and this value can vary between 3.17 eV and 3.39 eV, depending on preparation method and doping rate [18], which is somewhat lower than that of the other TCO materials, which is used as a material for optoelectronic devices in the blue and ultraviolet spectral range. Since more than 10 years zinc oxide sees a renaissance as an optoelectronic material, due to its high excitant binding energy of 60 meV, allowing excitonic emission even at room temperature [25]. The optical properties are characterized by transmission and reflection (figure1.5) or by spectroscopic ellipsometry [26].

(Figure 1.6) shows typical optical transmittance spectra in the wavelength range from 100 to 1200 nm of ZnO thin films prepared by ultrasonic spray pyrolysis [27]. The films are highly transparent in the visible region of the electromagnetic spectrum with an average transmittance values up to 68 %. The interference fringes originate from the multiple reflexions of light waves in the film between air and substrate interfaces. Their observation is an indication of the smoothness of the surface of the films. In addition, the interference fringes were used to determine the film thickness and the variations the refractive index n with photon wavelength [28]. Furthermore, the optical bandgap of the films was determined from the variations of the absorption coefficient with photon energy [29].

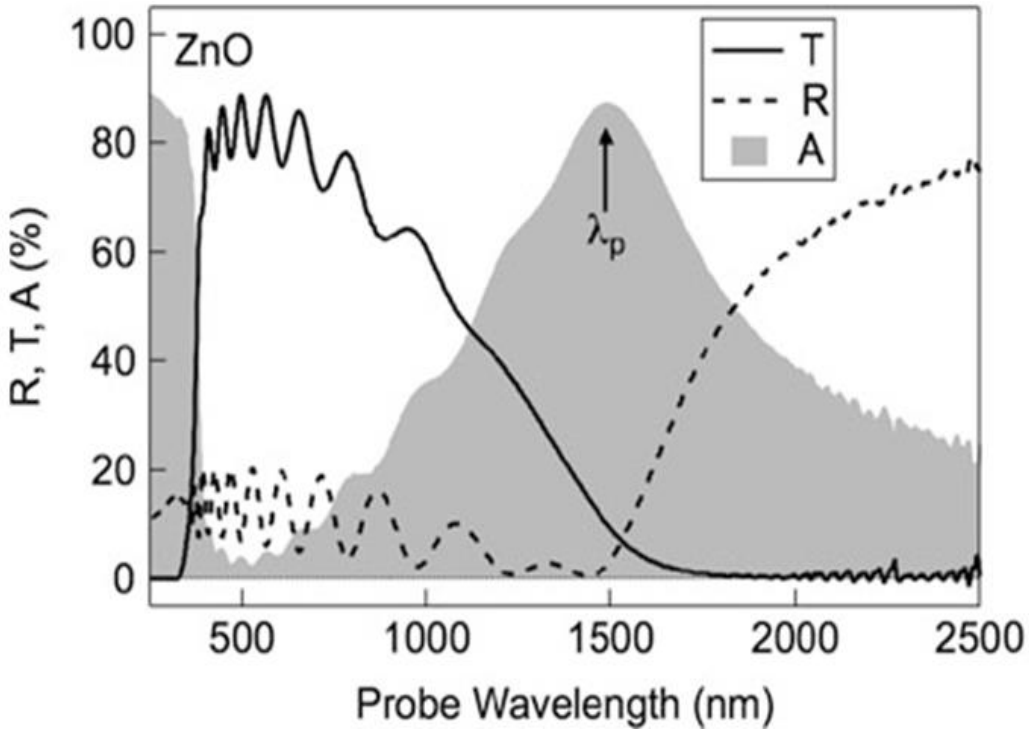

Figure 1.5: Optical spectra of typical (ZnO) transparent conductor [30].

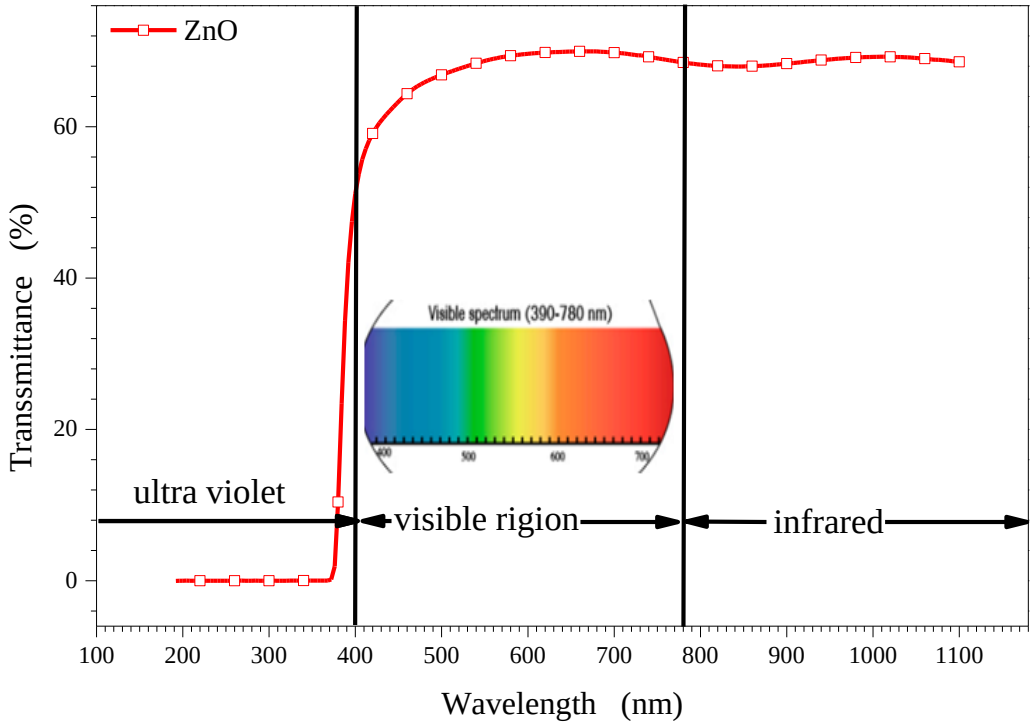

Figure 1.6: Optical transmittance spectra for ZnO thin film.

1.3.5 Thermal properties of ZnO

At 20 °C ZnO has a high thermal conductivity (25 $Wm^{-1}K^{-1}$). Polycrystalline ZnO has a rather low coefficient of linear thermal expansion α with a value of 4.3 $\times 10^{-6}K^{-1}$at 20°C. It increases to 7.7 × $10^{-6}K^{-1}$ and 8 × $10^{-6}K^{-1}$ at 600°C and 1200°C, respectively [24]. In ZnO single crystals, the thermal expansion is anisotropic. The α values parallel to the a-axis, ranging from 5.1×$10^{-6}K^{-1}$ at 20°C to 10.5×10^{-6} K^{-1} at 1200 °C, are higher than those parallel to the c axis, which range from 3×10^{-6} K^{-1} at 20 °C to 2×10^{-6} K^{-1} at 1200°C. These coefficients of thermal expansion are similar to those of polycrystalline $A1_20_3$. Zinc oxide starts to vaporize at around 1000 °C. It has appreciable vapor pressures of 1 torr at 1400 °C and 12 torr at 1500°C. The evolved vapors do not contain ZnO molecules but consist of elemental zinc and oxygen [24].

1.3.6 Photocatalytic properties of ZnO

Zinc oxide is a wide band gap n-type semiconductor (Eg = 3.3eV). The absorption spectrum of ZnO consists of a single, broad intense absorption band from 370 nm to lower wavelengths, ascribed to charge-transfer processes from the valence band to the conduction band [31].

Very highly reducing electrons and oxidizing holes are photogenerated on ZnO under UV light irradiation. Besides holes, h+, the main oxidizing species in water are hydroxyl radicals, $OH^{\bullet}$ other oxidizing species such as singlet oxygen, hydroperoxyl radicals and superoxide ions

play a minor role in photocatalytic transformations in liquid–solid reactions. In gas–solid reactions, the oxidizing species are predominantly superoxide ions [32].

The photocatalytic performance of ZnO is structure sensitive [33]. The typical blue shift of the band gap of nanostructured ZnO compared to bulk ZnO is due to surface and quantum size effects, several studies have established a relationship between ZnO nanoarchitecture and photocatalytic activity. A vast number of ZnO nanoarchitectures have been obtained under controlled synthesis conditions [33].The nanosized system attribute the improvement of the photocatalytic activities into the increasing formation of surface defects such as oxygen deficiencies and hydroxyl groups [34]. ZnO is sometimes preferred over TiO_2 for degradation of organic pollutants due to its high quantum efficiency [35]. Bactericidal properties of UV/ZnO were superior to UV/TiO_2 for Gram-negative Escherichia coli and Gram-positive Lactobacillus helveticus bacteria [36], ZnO has been used in the photodegradation of contaminants which are difficult to mineralize, like amides [37] or nitrobenzene [38].

1.3.7 Electrical properties of ZnO

The electrical properties of ZnO are hard to quantify due to large variance of the quality of samples available. The background carrier concentration varies a lot according to the quality of the layer substantially $\sim 10^{16} cm^{-3}$.The largest reported n-type doping is$\sim 10^{20}$ electrons/cm^3 and largest reported p-type doping is$\sim 10^{19}$ holes/cm^3, however such high levels of p-conductivity are questionable and have not been experimentally verified [39]. The exciton binding energy is 60meV at 300K, and is one of the reasons why ZnO is so attractive for optoelectronic device applications, the electron effective mass is $0.24m_0$, and the hole effective mass is $0.59m_0$. The corresponding electron Hall mobility at 300K for low n-type conductivity is $\mu=200 cm^2 V^{-1} s^{-1}$, and for low p-type conductivity is $5–50 cm^2 V^{-1} s^{-1}$ [40].

1.4 Iron oxide main properties

1.4.1 Introduction

Iron is abundant in the Earth’s crust and an important element in our environment. It is present in soils as oxides and easily mobilized in natural waters in the form of molecular complexes and colloids [41]. There are a number of iron oxides, hydroxides and oxy-hydroxides, as summarized in (Table 1.2) For simplicity, this group of iron oxi((oxy)hydroxi)des is often referred to as iron oxide [42].

Table 1.2: List of iron oxides, hydroxides and oxy-hydroxides [42].

Oxides	**Hydroxides**	**Oxy-hydroxides**
FeO, iron(II) oxide, (wüstite)	iron(II) hydroxide ($Fe(OH)_2$)	goethite (α-FeOOH)
Fe_3O_4, iron(II,III) oxide, (magnetite)	iron(III) hydroxide ($Fe(OH)_3$), (bernalite)	akaganéite (β-FeOOH)
Fe_2O_3, iron(III) oxide		lepidocrocite (γ-FeOOH)
α-Fe_2O_3, hematite		feroxyhyte (δ-FeOOH)
β-Fe_2O_3		ferrihydrite ($Fe_5HO_8 \cdot 4H_2O$ approx.)
γ-Fe_2O_3, maghemite		
ε-Fe_2O_3		

The structural chemistry of these compounds is diverse, reflecting the large number of atomic structures, as summarized in (figure 1.7) [43]. Almost all these phases can be formed from chemical solution, alluding to a complicated chemistry of formation [44]. In particular, the diversity of physicochemical conditions present in the environment (e.g. acidity, redox conditions, temperature, salinity, presence of organic or inorganic ligands, etc.) suggests, practically, all the iron oxide phases can be found naturally (figure 1.8)[43].

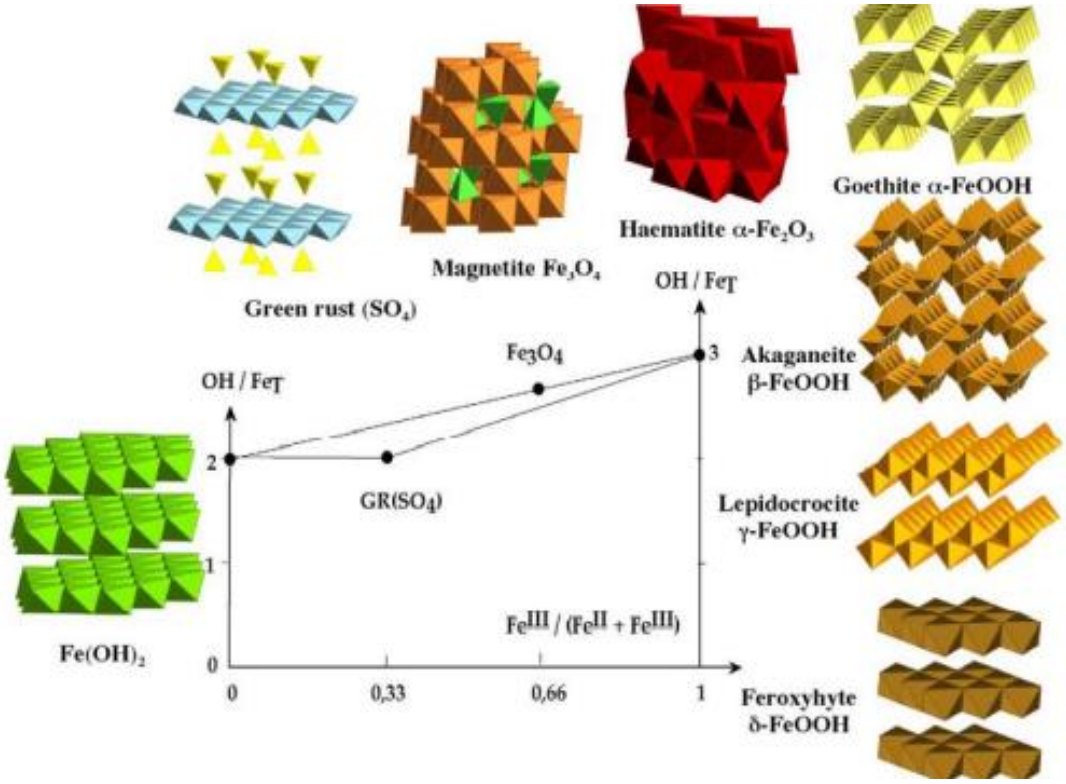

Figure 1.7: Many different phases of iron oxi((oxy)hydroxi)des [43].

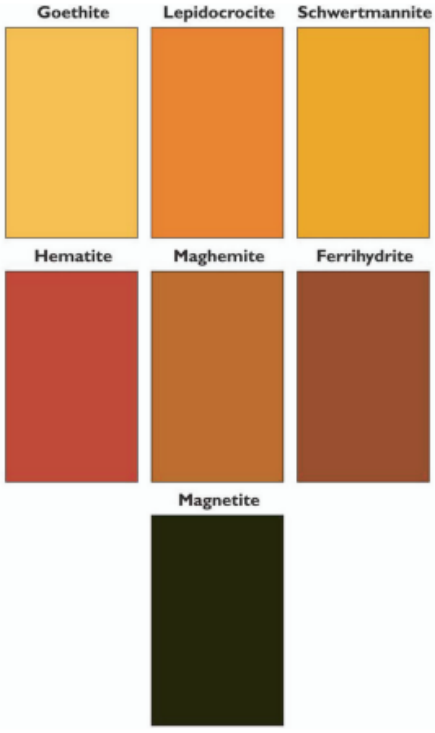

Figure *1.8*: Iron oxide colors [45].

1.4.2 Hematite – α-Fe_2O_3

Mineral hematite, α-Fe_2O_3, formerly spelt haematite, is derived from the Greek haimatite meaning 'blood-like', referring to its powder's shade of red [46]. In bulk compact form, it is colored black or silver-grey. Hematite is mined as the main ore for producing iron [46].

1.4.2.1 Crystallographic Structure of α-Fe_2O_3

The structure of α-Fe_2O_3 (figure 1.9.a), determined by Pauling and Hendricks in 1925, is iso structural with corundrum, α-Al_2O_3 [47]. The space group is R3c (rhombohedral symmetry) and the lattice parameters given in the hexagonal cell, shown in (figure 1.9.b, are: a = b = 5.0346 Å and c = 13.752 Å) [48].

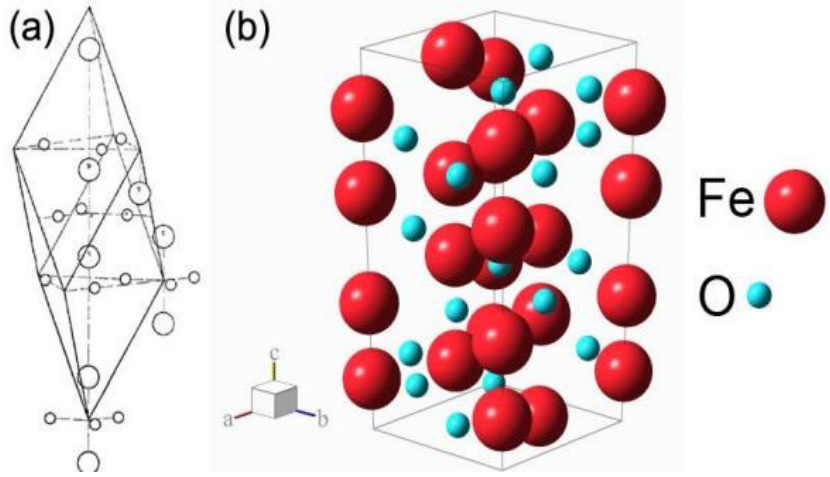

Figure *1*.9: (a): The arrangement of atoms in the structure of hematite (and corundum); small and large atoms represent oxygen and iron (or aluminium), respectively. (b): Model of the hematite unit cell [47].

Nanostructured α-Fe_2O_3 is the most thermodynamically stable iron oxide phase and is of particular interest because of its high resistance to corrosion, low processing cost and non-toxicity [49].This multifunctional material has therefore been investigated extensively for a variety of applications including photo-catalysis [50],gas sensing [51],magnetic recording [52],drug delivery [53],tissue repair engineering and magnetic resonance imaging [54],along with its use in lithium-ion batteries [55],spin electronic devices [56] and pigments [57]. In particular, the magnetic properties of α-Fe_2O_3 have attracted much interest over the past decades [58].

1.4.2.2 Modification Structure of α-Fe_2O_3

Different synthesis processes affect the shape and size of the nanomaterial. Lassoed et al. have shown that an increase of precursory ($FeCl_3$) concentration leads to a size increase of the alpha-hematite nanomaterial [59]. Figure 1.10 (a-d) shows the spherical structure of α-hematite [59].

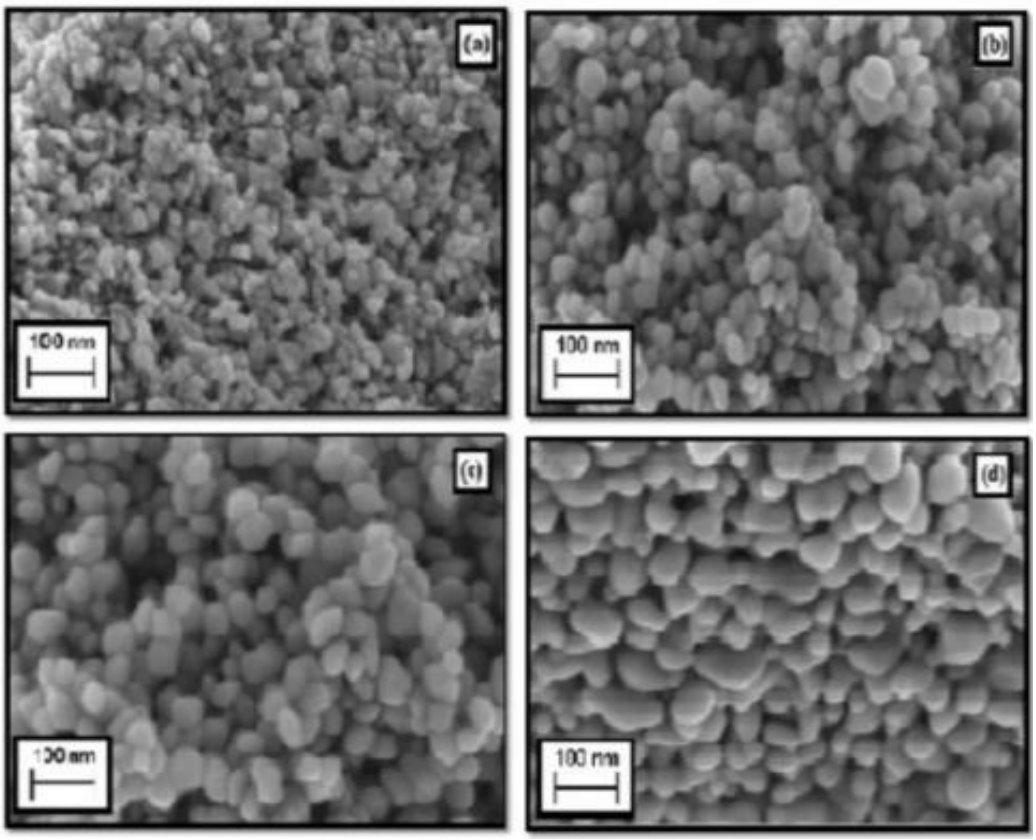

Figure *1*.10: SEM images of various concentrations of α-Fe_2O_3 [59].

1.4.2.3 Optical and photocatalytic properties of α-Fe_2O_3

Hematite (α-Fe_2O_3), an environmentally friendly n-type semiconductor it is one promising candidate for photocatalytic applications due to its narrow band gap of about 2.0–2.2 eV [60]. Further, hematite absorbs light up to 600 nm, collects up to 40% of the solar spectrum energy, is stable in most aqueous solutions (pH > 3), and is one of the cheapest semiconductor materials available. The photocatalytic performance of α-Fe_2O_3 is limited by certain factors such as high recombination rate of electrons and holes, low diffusion lengths of holes (2-4 nm), and poor conductivity, which led to both low efficiencies and a larger requisite over potential for photo-assisted water oxidation [60]. Many attempts have been made by researchers to overcome these anomalies of α-Fe_2O_3 such as lowering the recombination rate

by forming nanostructures, enhancement in conductivity by doping with suitable metals and improving the charge transfer ability [61].

1.4.2.4 Electrical properties of α-Fe_2O_3

The electrical conductivity of the Fe_2O_3 material is very poor without the presence of impurities. This is thought to be the result of the very low drift mobilities of charge carriers in this range, which require thermal activation to hop between lattice sites [62]. Conductivity in hematite is highly anisotropic, observed experimentally [63, 64] and confirmed theoretically [65, 66].

1.4.2.5 Applications of Fe_2O_3 material

1.4.2.5.1 Photovoltaic cells (PV cells)

Photovoltaic cells are one the most important applications globally, and countless materials have been tested to achieve high results. Alpha-hematite is a desirable material for PV because it is cheap, durable, and can absorb visible light from sun irradiation. The size of the material can also affect the absorption intensity [67]. The increase in magnetic tilt coupling brings the pair excitons, which causes local d-d transition and band tail types of charge-transfer. The band tail charge transfer produces photovoltaic responses due to delocalization [67].

1.4.2.5.2 Lithium Batteries

Lithium battery use is a broad subject, and many experiments have been performed to test various materials offering good results; alpha-hematite is one [68].

1.4.2.5.3 Supercapacitor

The supercapacitor is one application that uses alpha-hematite after enhancing its properties. PANI can be synthesized with alpha-hematite to have new structure nanowire arrays. The new structure of alpha-hematite-PANI offers the electrode for supercapacitor application having fast ion and electron transfer, large surface area, and structure stability [69].

1.5 Thin films deposition and spray pyrolysis technique

1.5.1 Thin films deposition

1.5.1.1 Definition of the thin film

It is possible to define a thin film of a material that is an element of this material so that its thickness is greatly reduced, which is expressed with nanometers. (Layer quasi-two dimensionality) [70].

Thin films nature can be insulating (SiO_2, SiN_4, SiC,), metallic (Al, Cr, Au, Ag...) and semi-conductor (Si, GaAs, CdTe, ZnO...), While its structure can be amorphous, nanocrystalline, microcrystalline or monocrystalline [71].

The property of thin film generally varies from the values of the physical parameters of the materials in bulk form as given below [72].

- Quasi-two dimensional
- Different defect structures from the bulk material
- Strongly influenced by surface and interface effects.

These unique properties can be due to their small thickness of few atomic layers up to micrometer value. This will change the optical, magnetic, electrical, thermal, mechanical and chemical properties. (Table1.3) divides thin film properties into five basic categories and gives example of typical applications within each category. The properties of the thin films can also be affected by the high surface to volume ratio of the film [72].

Table 1.3: Properties and applications of thin films [72]

Thin film property category	Typical Applications
Optical	• Reflective/ antireflective coatings • Interference filters • Decoration (color, luster) • Optical memory discs (CDs, DVDs) • Optical Waveguides
Magnetic	• Memory discs (Hard discs and tapes)
Electrical	• Insulation • Conduction • Semiconductor devices • Piezoelectric drivers
Thermal	• Barrier layers • Heat sinks
Chemical	• Barrier to diffusion or alloying • Protection against oxidation or corrosion • Gas/liquid sensors • Photocatalytic
Mechanical	• Tribological (wear-resistant) coatings • Hardness • Adhesion • Micromechanics

1.5.1.2 Classification of thin films deposition techniques

Thin films deposition techniques divide into two groups, depending on the nature of the deposition process. Physical methods include physical vapor deposition (PVD), laser ablation, molecular beam epitaxy and sputtering. Chemical methods comprise of gas phase and solution deposition. The gas phase techniques include chemical vapor deposition (CVD) and atomic layer epitaxy (ALE). The solution deposition techniques include spray-pyrolysis deposition,

sol-gel, spin-coating and dip-coating (Figure1.11) [73]. Research on optimization of thin films making techniques lead to the development of new technologies [73].

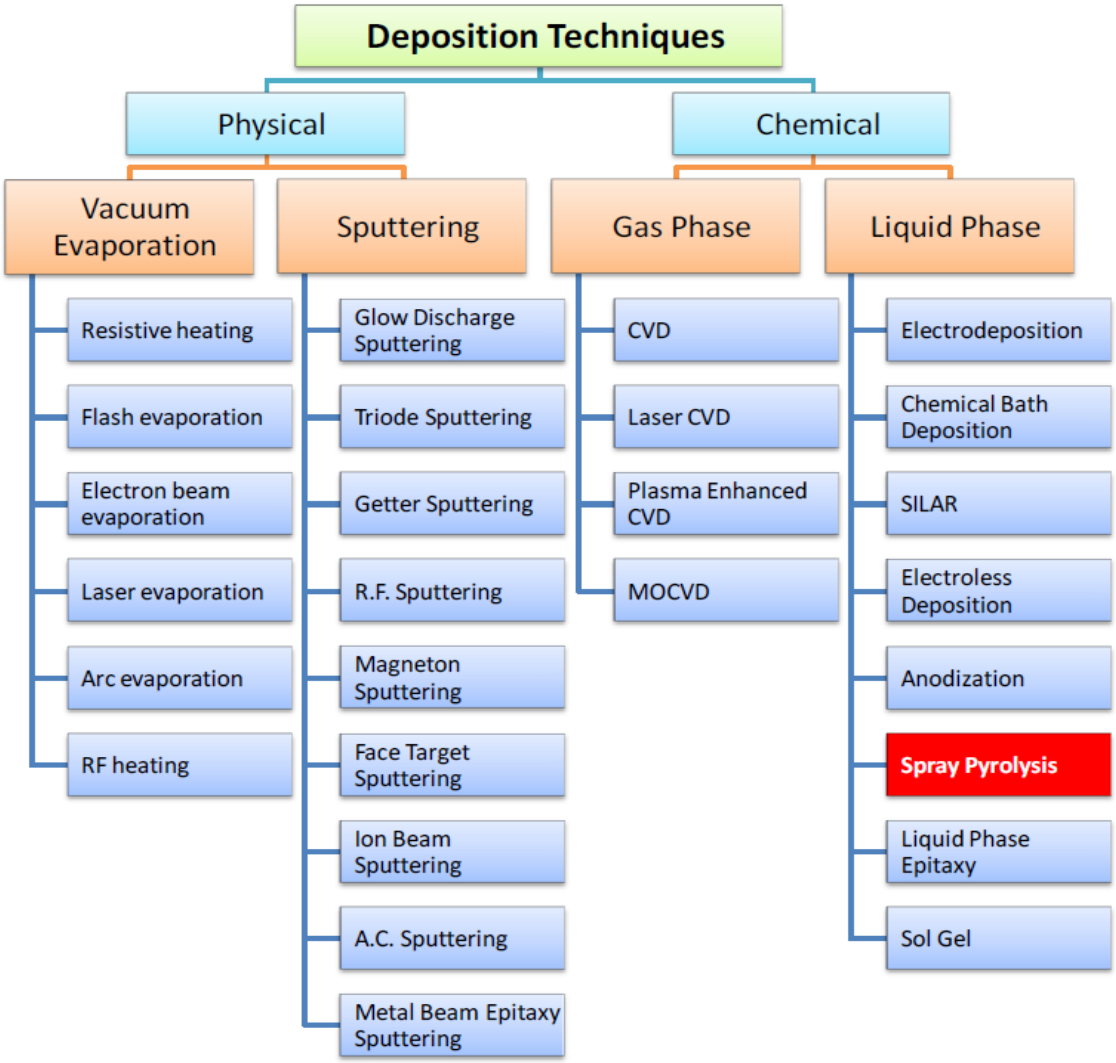

Figure *1*.11: Spray pyrolysis in the classification of thin film deposition techniques [73].

1.5.2 Spray-pyrolysis technique

Compared to other techniques, spray-pyrolysis has many advantages. It requires only simple and inexpensive equipment and offers an easy way to add doping materials. It has a good reproducibility, a high films growth rate with chemical homogeneity in the final product and the potential for deposition over large areas. The films, dense or porous, have thicknesses ranging from 0.1 to 10 μm [74].

The technique itself consists of a precursor solution that is sprayed through an air atomizer on a heated substrate, producing thin films. It is well established that the morphology and quality of the deposited films are strongly linked to the substrate temperature. Defects, such as

non-uniformity of the film, cracks and pores, are among the most frequent problems presented in the films deposited by spray pyrolysis [74].

For the technological use of the films obtained by spray pyrolysis it is necessary that some of its interesting features are understood and controlled. The relationship between the procedural parameters, the characteristics of the deposit microstructures and the final properties obtained, is the foundation for understanding and mastering this technique [73].

Spray pyrolysis is a technique through which dense or porous films and powders can be obtained by controlling the deposition parameters. This technique involves the atomization of a precursor solution that is thrown directly over the heated substrate where the film will be formed [73].

Compared with other techniques for obtaining films, this technique presents a simple experimental arrangement and is a cost effective method, mainly due to its simple equipment. It does not require the use of high quality reagents and substrates. The composition of the films can be easily controlled with the reagents used in the precursor solution. Several types of films have been deposited by spray pyrolysis, and this technique has been used for decades in various industries, such as in the production of glass, solar cells and electrical conductive electrodes [74].

The equipment used in the spray-pyrolysis technique consists basically of an atomizer and a temperature controller (Figure1.12). There are several types of atomizers. The most common ones are compressed air atomizers [75] (when the spray of the precursor solution is produced by a jet of air), electric field atomizers [76] (when the spray of the precursor solution is produced by an electric field) and ultrasound atomizers [77] (when the spray of the precursor solution is produced through high frequencies).

When the spray collides on a surface, the atoms lose energy to it. After the impact, the atoms spread on the surface interacting with other adsorbed atoms. A fraction of the atoms can initiate the formation of an island that can grow in size and coalesce, forming a continuous film [78].

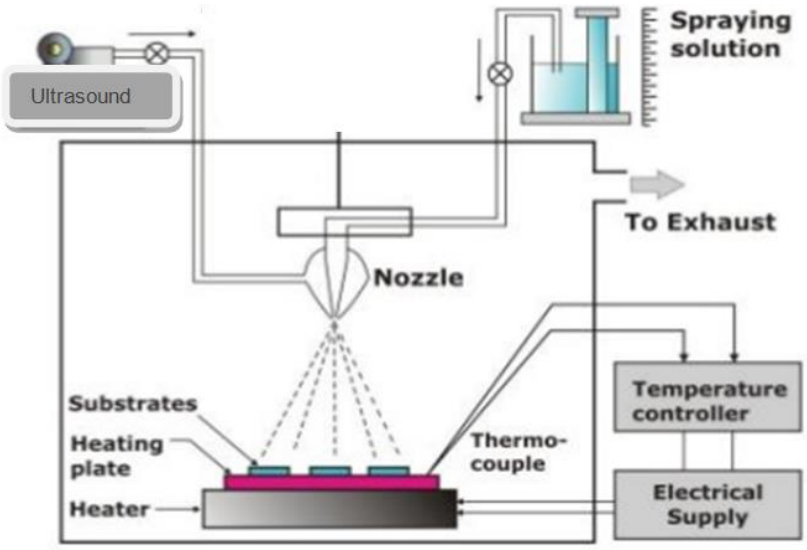

Figure *1*.12: Schematic set-up for ultrasonic spray pyrolysis technique [77].

Zhang and Messing [79] demonstrated an important criterion for the synthesis of fine solid particles from the observation that the precipitated salt particles do not suffer plastic deformation or melt during heating, because of the formation of droplets from reservoirs with low permeability. Consequently, the residual solvent is trapped in the dried droplet, resulting in an increase in pressure, because then the solvent cannot evaporate easily. Consequently, the shell breaks, producing secondary drops, breaking the shell of the droplets formed above a powder, which produces an irregular shape (Figure1.13). Liu et al. [80] also concluded that the high solubility of the salts is not necessary for the formation of solid and uniform particles, as previously stated by other authors.

There is a strong influence of deposition parameters in determining whether the film deposited by being deposited is dense or porous (Figure1.14). If the intermediate reactions occur at some distance from the substrate, the film will be porous, with some cracks. If these same reactions occur near the substrate, but not touching it, the film should be dense. In a third case, if these intermediate reactions occur well before touching the substrate, a powdery film is formed [81]. Also by increasing deposition temperature, the morphology of the film can be shifted from porous to extremely dense.

Figure *1*.13: Steps of powder production during the spray-pyrolysis [79].

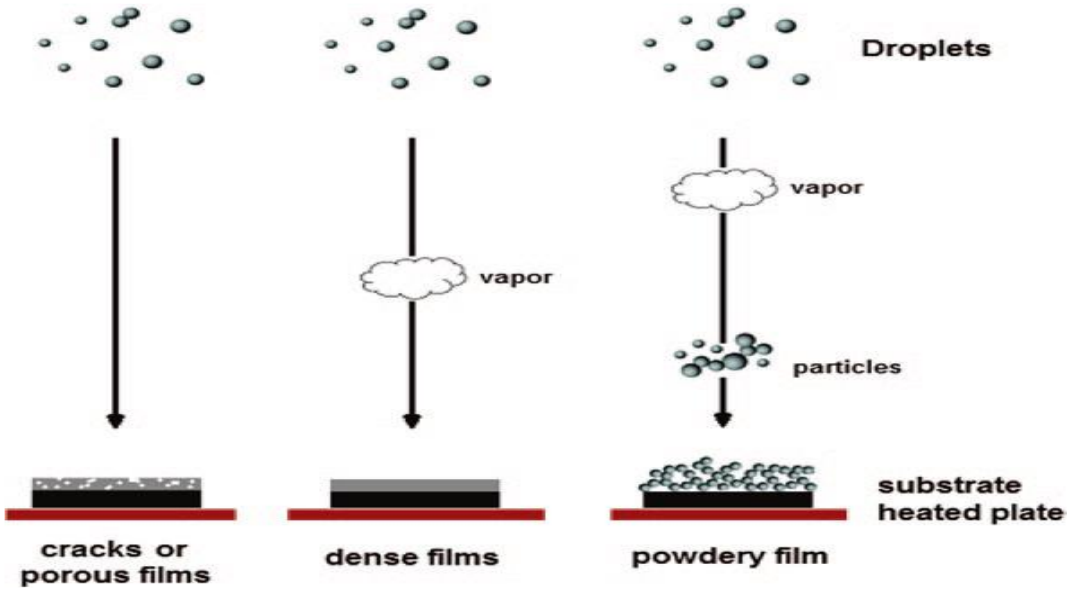

Figure *1*.14: Schematic diagram of the spray-pyrolysis film formation mechanisms [81]

Several studies have been conducted to better understand what occurs during the deposition by spray pyrolysis. Many authors have attempted to develop a model to explain what happens during this process. There are several steps that occur sequentially or simultaneously during film formation by spray pyrolysis and they can be modelled simply. Understanding these steps can help improve the quality of the film. Spray-pyrolysis can be divided into three main steps: atomization of the precursor solution, the transport of aerosols and the resulting decomposition of the precursor solution on the substrate [74].

1.5.2.1 Atomization of precursor solution

Atomizing the precursor through a jet of compressed air, an ultrasonic system and an electrostatic atomizer are the most commonly used methods in spray pyrolysis. Many articles have been published on the mechanism of atomization of precursor solutions. Kufferath et al. [82] evaluated the influence of fluid properties on the characteristics of the compressed air spray. Taniguchi et al [83] studied high frequency atomization (ultrasound). Depending on the parameters of the spray jet modes, a different particle size distribution was obtained.

Atomization by compressed air involves the use of air at high speeds to produce an aerosol. The liquid is introduced into an air stream and drops are pulverized through the energy of the gas stream [84]. Typically, the fraction of the deposited material is small due to excess spray spread. Many drops are deflected or reflected from the surface of the substrate, decreasing

the deposition efficiency. In general, the droplet size grows proportional to the increase of viscosity, surface tension and density [74].

1.5.2.2 Aerosol transportation

In the formed aerosol, droplets are transported and eventually evaporated. When thick films are desired, it is important that during transport as many drops as possible fly into the substrate without the formation of particles before reaching the substrate surface (Figure1.15). In this process, the trajectory of the droplets and evaporation is influenced by gravitational, electric or thermophoretic forces [74].

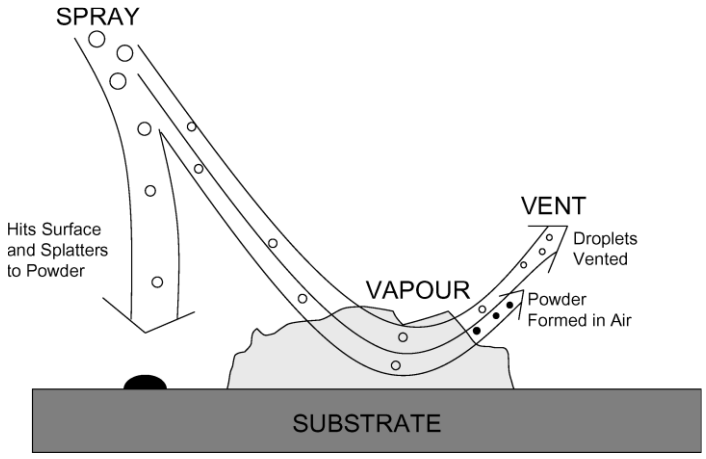

Figure *1*.15: Aerosol transport [74]

Particles that attach to the substrate form a powdery deposit. Some authors suggest that forcing the drops closer to the heated substrate, without touching it, is the most efficient way to improve this kind of film growth [74].

The solvent present in the droplets will evaporate during the transportation from the atomizing nozzle to the substrate. This evaporation of the solvent leads to a decrease in droplet size and therefore a concentration gradient of the salt precursor. This precursor precipitates on the surface of the drop when the concentration exceeds the solubility limit. The precipitation occurs due to rapid evaporation of the solvent while the diffusion of the solvent is much slower. This situation will result in a crust and subsequently in porous hollow particles. This effect is not desired in film formation due to increased roughness of the film [74].

1.5.2.3 Decomposition of the Precursor

Many processes can occur when the drop hits the surface of the substrate, such as evaporation of the residual solvent, scattering of the drops and decomposition of salt. Many models exist for the decomposition of the precursor salt. But most authors suggest that the process of CVD (chemical vapor deposition) gives high-quality films by spray pyrolysis [73]. Perednis [74] proposed that the following processes may occur when the temperature is increased: at lower temperatures the drop spreads through the substrate and then decomposes. At higher temperatures the solvent evaporates completely during flight and the dried precipitate drop hits the substrate, where decomposition occurs. At even higher temperatures the solvent also evaporates before the drop reaches the substrate. Then the precipitated solid melts, vaporizes without decomposition and the vapour diffuses into the substrate to undergo a CVD process. If we increase the temperature furthermore the precursor evaporates before reaching the substrate and consequently solid particles are formed after the chemical reaction in the vapour phase. The author speculates that rough and non-adherent films are formed. Adherent films were obtained in the process of chemical vapour deposition (CVD) at intermediate temperatures. Chen et al. [85] studied the correlation between the morphology of the films and the deposition parameters. They concluded that the most important parameter is the deposition substrate temperature. Precursor solution concentration has a minor influence on the quality of the deposition.

1.5.2.4 Influence of Spray Parameters on the Morphology of the Film

The morphology of the film is highly dependent on the substrate temperature at the time of deposit in spray-pyrolysis. Chen et al. [86] observed four types of morphology: dense films, dense films with embedded particles, dense film with a porous layer on top and porous morphology. Ruiz et al. [87] investigated the influence of gas loading, substrate composition, temperature and time on the deposited film. The most important parameters according to these authors were the drop size and substrate temperature. The behaviour of the spray droplet is determined by surface tension and roughness of the substrate to be coated. The roughness of the substrate and porosity of the substrate also significantly influence the film morphology. Films with low porosity were produced when the precursor solution used solvent high boiling temperatures solvents [86]. This was attributed to a lower rate of evaporation of the solvent during the transport of droplets to the substrate and hence a lower rate of precipitation of the precursor [86].

Organic precursors are more favourable to the spray-pyrolysis technique than inorganic reagents. This is due to the fact that they have higher volatility (organic solvents) and lower deposition temperatures. With inorganic precursors, it is easier to control grain size by changing the deposition parameters [88].

1.6 Photocatalysis

1.6.1 Introduction

Industrialization, technologies, and consumption of non-renewable sources are increasing at a rapid rate since the last few decades, because of regular continuous increasing demands of materials related to textile, dye, fertilizer, domestic, plastic, etc [89]. As a consequence, environmental pollution and energy crises have already reached an alarming stage. The industrial wastes are more toxic and non-biodegradable as compared to municipal wastes because these consist of fats, oil, grease, heavy metals, phenols, and ammonia, etc [89]. The agriculture and pharmaceutical effluents release pesticides and other chemicals that are responsible for some chronic diseases, harmful for human endocrine, making water not useful for drinking and other end uses [90]. There is an urgent need to develop some newer technologies that are eco-friendly in nature and lead to degradation or complete elimination of environmental pollutants and thus, prove to be an alternative clean strategy. In other words, there should be a sustainable solution to the problem [90].

In the modern era, water pollution turns out to be the finest topic to discuss because of the depletion of underground water resources and the lack of managing wastewater, which ensures an unsustainable life with safe water [91]. Even, very lesser amounts of water effluents create adverse health effects in humans and other ecosystems. Hence, industrial discharge of wastewater requires proper sewage treatment plants for the essential wastewater management [91, 92, 93]. Wastewater treatment technologies have come up with various efficient methods, but cheaper and less time-consuming method is a major tool to access safe water [92].

1.6.2 Main source of water pollution

Water as an environmental resource is regenerative in the sense that it could absorb the pollution loads up to certain levels without affecting its quality. In fact, there could be a problem of water pollution only if the pollution loads exceed the natural regenerative capacity of a water resource [94]. In the last decades, water pollution has moved to the top of the international political agenda due to its undesirable health and environmental effects. The contaminants released from industries and agricultural activities have become the main source, which affects

most of the water bodies in the ecological system [92, 95]. It has already been reported that the major organic compounds responsible for increasing environmental threat are the industrial dyes and textile dyes. About 10–20% of total dye products in the world is lost in textile wastes during the manufacturing process and released as effluents into the green environment [91, 93]. Organic dyes are one of the leading groups of pollutants released into wastewaters from textile and other industrial processes [92, 95]. On a global scale, over 0.7 million tons of organic synthetic dyes are manufactured every year mainly for use in the textile, leather goods, industrial painting, food, plastics, cosmetics, and consumer electronic sectors [96]. There are at least million colored chemical substances that were produced during the last century, out of these about 10,000 were industrially produced [91, 93]. Major pollutants in textile wastewaters are highly suspended solids, chemical oxygen demand, heat, color, acidity, and other soluble substances [92]. Textile industries discharge a large quantity of dyes into water bodies which pose serious ecological problems [94]. Many industries use dyes extensively for various operations such as textile, paper, plastic, leather, tanning, etc. These industries discharge mixing of pollutants in a different process [92]. The main pollution in textile wastewater came from dyeing and finishing processes. The textile industry uses approximately 21–377 m^3 of water per ton of textile produced and thus generates large quantities of wastewater from different steps of dyeing and finishing process [92].

Colorants or additive substances causing variation in color or visible light absorption can be divided into two categories: dyes and pigments [96, 97]. The distinct delineation between dyes and pigments is as follows: Dyes are soluble or partly soluble organic (carbon-based plant and animal extracted) colored compounds suspended in a medium that represents one type of colorant [97]. The process of dyeing can be loosely defined as imparting colour to the textile fiber or leather. On the other hand, typically pigments are complete insoluble substances that have no chemical affinity for the substrate to be colored [97].

Industrial wastewater is becoming more and more contaminated with the increasing number of industrial chemical products. The wastewater generated by the textile industry is rated as the most polluting source among all industrial sectors. The textile industry utilizes about 10,000 different dyes and pigments and more than 50% of which are azo dyes. Dyes can be classified on the basis of structure, function, or both. Dyes can also be classified as acid, basic, direct, disperse, reactive, anionic, cationic, etc., and indeed this notation is often simultaneously used with the dye chemical structure type (for example Basic Blue 41 and Acid Yellow 23 are both mono azo dyes) of the synthetic dyes manufactured today; azo compounds are considered dominant (≈50–70%) with anthraquinone dyes being a distant second [97].

The textile wastewater treatment is a very serious problem due to several reasons which are listed as follows:

- High total dissolved solids (TDS) content of the wastewater,
- Presence of toxic heavy metals such as Cr, As, Cu, Cd, etc.
- Non-biodegradable nature of organic dyestuffs present in the effluent, and
- The presence of free chlorine and dissolved silica. Most dyes used in the textile industries are stable to light and not biologically degradable. Because dyes usually have a synthetic origin and complex aromatic molecular structures which make them more stable and more difficult to biodegrade [98].

Pagga et al. reported that out of 87% dyestuffs, only 47% are biodegradable. It was estimated that about 12–15% of these dyes are released as effluents during the making processes which cause unfavourable environmental pollution [97].

1.6.3 Classification of dyes

Synthetic dyes are used for textiles, papers, plastics, colour photography and petroleum product additives; they are also used in specialized applications such as foods, drugs and cosmetics [99]. Synthetic dyes are aromatic compounds produced by chemical synthesis. This is because, this type of dyes is stable, recalcitrant, colorant and even carcinogenic and toxic, their release into the environment creates severe environmental, aesthetic and health problems [100]. Their colour is due to their chromogen-chromophore structure (electron acceptor), and their dyeing capacity is due to their auxochrome group (electron donor). The chromogen is constituted from an aromatic structure normally based on benzene, naphthalene or anthracene rings. The chromophore configurations are represented by the azo group (—N=N—), ethylene group (=C=C=), carbonyl group (=C=O), carbon–nitrogen (=C=NH; —CH=N—), carbon–sulphur (=C=S; ≡C—S—S—C≡), nitro (—NO_2; —NO—OH) or nitroso (−N=O; =N−OH). To produce colour, it is essential for an organic compound to contain at least one group of chromophores on an aryl ring forming an alternating single and double bond. The usual auxochrome groups are amino (—NH_2), carboxyl (—COOH), sulphonate (—SO_3H) and hydroxyl (—OH).These groups intensify the colour of the dye because their presence in the dye molecules allows greater quantum absorption of the photons. Textile dyes are mainly classified in two different ways: (1) based on their application characteristics (Colour Index (CI) generic name, such as acid dye, basic dye, direct dye, disperse dye and reactive dye); and (2) based on their chemical structure (CI constitution number, such as nitro, azo, anthraquinone, xanthene and sulphur) [101].

1.6.4 Wastewater treatment methods

Wastewater treatment and recycling is an essential component and the researchers are coming forward to carry out with convenient economical technologies. The wastewater has been treated by different physical, chemical, and biological processes [92]. The major environmental aspect is the removal of color from textile and dyestuff manufacturing wastewater. A large number of conservative treatment processes have been employed in various industrial wastewaters such as chemical, biological, food, pharmaceutical, pulp and paper, dye processing, and textile wastes [92, 102, 103, 104]. Conventional biological treatment processes are not successful because of the recalcitrant nature of synthetic dyes and the high salinity of wastewater containing dyes [92, 105]. Chlorination and ozonation are also quite incapable owing to their high operating costs [106]. The traditional physical techniques such as adsorption on activated carbon, ultra-filtration, reverse osmosis, coagulation by chemical agents, ion exchange on synthetic adsorbent resins, etc., have been used for the removal of dye pollutants [106]. These methods are successful only in transferring organic compounds from water to another phase, thus creating secondary pollution which requires further treatment of solid wastes and regeneration of the adsorbent which makes the process costlier.

The following essential factors must be considered in the wastewater treatment technologies [107, 108]:

- Treatment flexibility.
- Mineralization of parent and intermediate contaminants.
- The final efficiency of wastewater treatment.
- Recycling capacity and potential use of treated water.
- Cost-effectiveness and eco-friendliness.

Therefore, substantial attention has been focused on complete oxidation of organic compounds to harmless products such as CO_2 and H_2O by the advanced oxidation process (AOP) and appears as one of the most confidential technologies. AOPs can be classified into two groups:

(1) Non-photochemical AOPs; Non-photochemical AOPs include cavitations, Fenton and Fenton-like processes, ozonation, ozone/hydrogen peroxide, wet air oxidation [110].

(2) Photochemical AOPs and photochemical oxidation processes include homogeneous (UV/hydrogen peroxide, UV/ozone, UV/ozone/hydrogen peroxide, photo-Fenton, homo and heterogeneous (photocatalysis) processes) [111]. The intention of any AOPs design is to produce and use hydroxyl free radical (OH•) as a strong oxidant to destroy compounds that

cannot be oxidized by the conventional oxidant. Hydroxyl radicals are non-selective in nature and they can react without any other additives with a series of contaminants whose rate constants are usually in the order of 10^6–10^9 mol l^{-1} S^{-1}[111].

The main and short mechanism of AOPs can be explained as follows:

- Initially, the light energy fall on the surface of a catalyst, the valence band electrons are agitated and move to the conduction band. Holes would be left in the valance band of the catalyst. These holes in the valence band can oxidize donor molecules and react with water molecules to generate hydroxyl radicals (The hydroxyl radicals have strong oxidizing power responsible for the degradation of pollutants).
- The oxidative reaction of these radicals with organic compounds in the water producing biodegradable intermediates.
- The reaction of biodegradable intermediates with oxidants is referred to as mineralization (i.e., production of water, carbon dioxide, and inorganic ions).

1.6.5 Discovery of Photocatalysis

In 1972, **Fujishima** and **Honda** discovered the phenomenon of a photocatalytic splitting of water on a TiO_2 electrode under ultraviolet (UV) light [109]. This event becomes noticeable as the beginning of a new era in heterogeneous photocatalysis. However, this discovery was not accepted at first by electrochemists because at that time, the idea that light could also be used as an energy source had not yet taken hold among electrochemists who maintained that oxygen could not be generated at such a low voltage, because water electrolysis takes place at 1.5–2 V or even higher. Since then, for understanding the fundamental processes and enhancing the photocatalytic efficiency of TiO_2, extensive research was performed by chemists, physicists, and chemical engineers. Such studies are frequently related to energy renewal and energy storage [109, 110]. TiO_2-based photocatalysts are considered as an attractive approach growing rapidly for the total destruction of organic compounds in polluted air and wastewater [109, 110].

Prof. **Fujishima** stresses that benefits of science and technology should be shared by everyone. He says "***The primary objective of science and technology is to create a society where people can have healthy, comfortable and long lives. The crucial thing in science and technology is to develop a new concept that can be applied to actual products and services, and these new products and services will eventually make people happy***". By making use of his discovery of photocatalyst, he came forward to create such a society [110].

1.6.5.1 Definition of Photocatalysis

Photocatalysis is the amalgamation of photochemistry and catalysis. The word "**photocatalysis**" is derived from the Greek language and composed of two parts:

- The prefix photo means **light**
- **Catalysis** is the process where a substance involves in altering the rate of a chemical transformation of the reactants without being altered in the end. The substance which is known to be a catalyst increases the rate of the reaction by reducing the activation energy.

Hence, photocatalysis is a process where light and catalysts are concurrently used to support or speed up a chemical reaction. So, photocatalysis can be defined as "**catalysis driven acceleration of a light-induced reaction.**"

Photocatalyst is classified into two categories: homo- and heterogeneous process [112]

- Homogeneous photocatalysis: When both the semiconductor and reactant are in the same phase, i.e. gas, solid, or liquid, such photocatalytic reactions are termed as homogeneous photocatalysis.
- Heterogeneous photocatalysis: When both the semiconductor and reactant are in different phases, such photocatalytic reactions are classified as heterogeneous photocatalysis.

An excellent semiconductor photocatalyst should be [112]:

(i) photoactive,
(ii) able to utilize visible and/or near-UV light,
(iii) biologically and chemically inert,
(iv) photo stable (i.e., stability toward photo corrosion),
(v) inexpensive, and
(vi) Nontoxic.

Semiconductor photocatalysis emerges to be a promising technology that has a number of applications in environmental systems [111].

The photocatalyst is an extraordinary method which can be used for various purposes like degradation of various organic pollutants in wastewater, production of hydrogen, purification of air, and antibacterial activity. Recently, the photocatalytic process is attaining more concentration in the field of wastewater treatment to obtain complete mineralization of the pollutant achieved under mild conditions of temperature and pressure. The noteworthy features of these processes include undisposed of waste and cost-effectiveness when sunlight

or near-UV light can be used as a source of irradiation. Photocatalyst is a term which means photon assisted generation of catalytically active species. In general, Photocatalysis can be defined as "***a change in the rate of chemical reactions or their generation under the action of light in the presence of substances called photocatalyst that absorbs light quanta and is involved in the chemical transformations of the reactants***" [113].

1.6.5.2 Photocatalytic mechanism

Photocatalytic reaction primarily depends on wavelength or light (photon) energy and the catalyst. In general, semiconducting materials are used as a catalyst which performs as sensitizers for the irradiation of light stimulated redox process due to their electronic structure, which is characterized by a filled valence band and a vacant conduction band [113]. (Figure1.16) shows the schematic representation of semiconductor photocatalytic mechanism.

The fundamental steps in the process of semiconductor photocatalysis are as follows [110, 113]:

- When the light energy in terms of photons fall on the surface of a semiconductor and if the energy of incident ray is equivalent or more than the bandgap energy of the semiconductor, the valence band electrons are agitated and move to the conduction band of the semiconductor.
- Holes would be left in the valence band of the semiconductor. These holes in the valence band can oxidize donor molecules and react with water molecules to generate hydroxyl radicals (The hydroxyl radicals have strong oxidizing power responsible for the degradation of pollutants).
- The conduction band electrons react with dissolved oxygen species to form superoxide ions. These electrons induce the redox reactions.

These holes and electrons could undergo successive oxidation and reduction reactions with any species, which might be adsorbed on the surface of the semiconductor to give the necessary products.

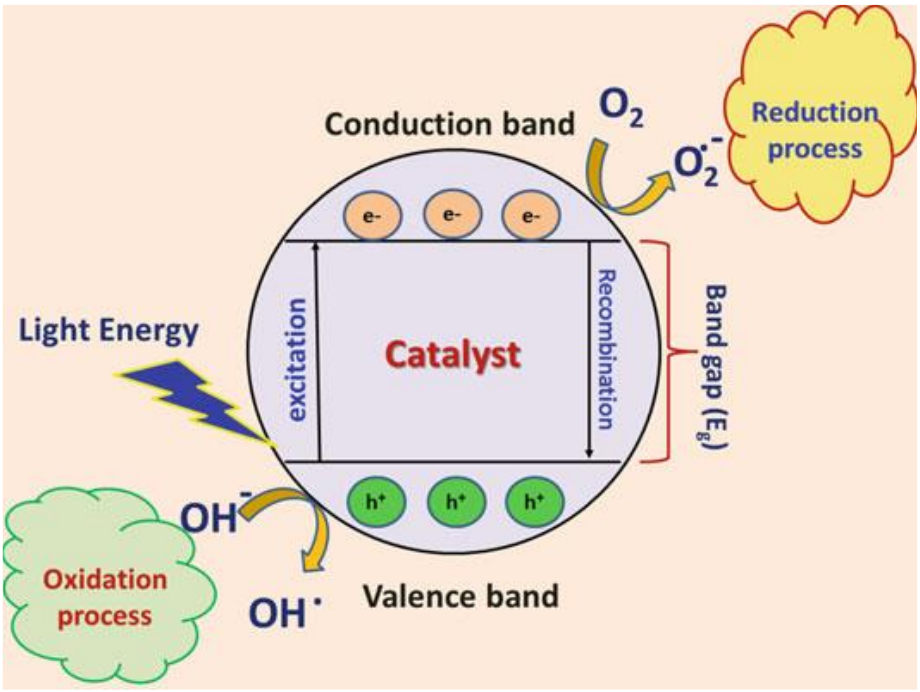

Figure *1*.16: Schematic representation of semiconductor photocatalytic mechanism [114]

1.6.5.3 Description of oxidation mechanism

The photocatalyst surface contains water, which is mentioned as "absorbed water." This water is oxidized by positive holes created in the valence band due to the electrons shift to the conduction band as a result of light irradiation, thus making way for the formation of hydroxyl radicals (OH·) (agents which have strong oxidative decomposing power). Afterward, these hydroxyl radicals react with organic matter present in the dyes. If oxygen is present when this process happens, the intermediate radicals in the organic compounds along with the oxygen molecules can experience radical chain reactions and consume oxygen in some cases. In such a case, the organic matter finally decomposes ultimately becoming carbon dioxide and water [109]. Under such circumstances, organic compounds can react straightly with the positive holes, resulting in oxidative decomposition. The complete oxidation processes were shown in (Figure1.17).

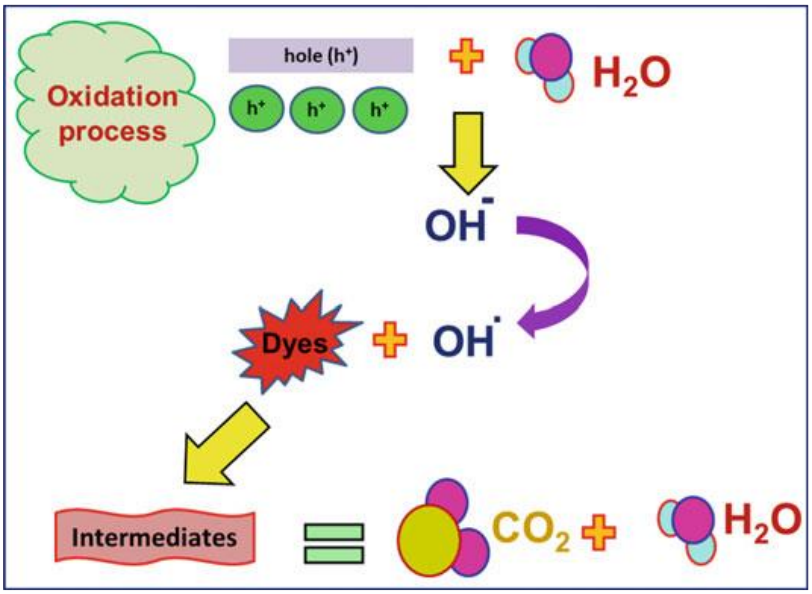

Figure *1*.17: Schematic representation of oxidation mechanism [114]

1.6.5.4 Description of Reduction Mechanism

(Figure1.18) represents the reduction process, the reduction of oxygen contained in the air occurs as a pairing reaction [114]. Reduction of oxygen takes place as an alternative to hydrogen generation due to the fact that oxygen is an easily reducible substance. The conduction band electrons react with dissolved oxygen species to form superoxide anions. These superoxide anions attach to the intermediate products in the oxidative reaction, forming peroxide or changing to hydrogen peroxide and then to water. The reduction is likely to occur more easily in organic matter than in water. Therefore, the higher concentration of organic matter tends to increase the number of positive holes. This reduces the carrier recombination and enhances the photocatalytic activity [114, 115].

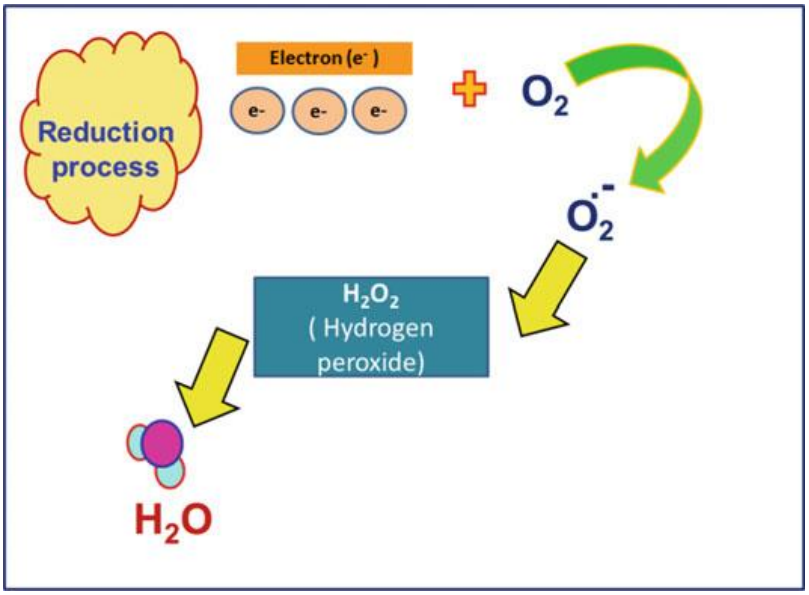

Figure *1*.18: Schematic representation of reduction mechanism [114]

1.6.5.5 Semiconductor Photocatalyst

During the last three decades, the researchers have much focusing attention on the reactions that take place on the illuminated surface of semiconductor metal oxides, sulfides, and selenides (Figure1.19), which have a modest bandgap energy of 1.1– 3.8 eV between their valence and conduction bands [115]. The most efficient photocatalytic materials found in the literature are metal oxides such as TiO_2, ZnO, and CeO_2 [115].

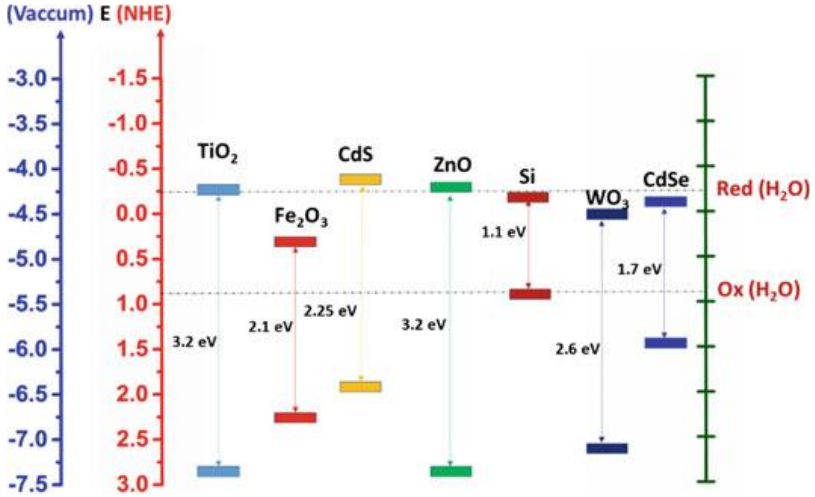

Figure *1*.19: Bandgaps and redox potentials, using the normal hydrogen electrode (NHE) as a Reference for several semiconductors [115]

In general, the photocatalytic reaction mechanism of semiconductors is explained by the following equation based on the earlier reports [93]

$$\text{SemiconductorLight} + \text{Energy} \rightarrow \text{Semiconductor}(e^-_{cb} + h^+_{vb})$$

$$\text{Dye} + \text{Semiconductor}\ (h_{vb}^{+}) \rightarrow \text{Oxidation process}$$

$$\text{Semiconductor}(h_{vb}^{+}) + H_2O \rightarrow \text{Semiconductor} + H^{+} + OH^{\cdot}$$

$$\text{Semiconductor}\ (h_{vb}^{+}) + OH^{-} \rightarrow \text{Semiconductor} + OH^{\cdot}$$

$$\text{Dye} + \text{Semiconductor}\ (e_{cb}^{-}) \rightarrow \text{Reduction process}$$

$$\text{Semiconductor}\ (e_{cb}^{-}) + O_2 \rightarrow \text{Semiconductor} + O_2^{\cdot -}$$

$$O_2^{\cdot -} + H^{+} \rightarrow HO_2^{\cdot}$$

$$HO_2^{\cdot} + HO_2^{\cdot} \rightarrow H_2O_2 + O_2$$

$$H_2O_2 + O_2^{\cdot -} \rightarrow OH^{\cdot} + OH^{-} + O_2$$

$$\text{Dye} + OH^{\cdot} \rightarrow \text{Degradation products}$$

ZnO is sometimes preferred over TiO_2 for the degradation of organic pollutants due to its high adsorption properties [116, 117]. Unfortunately, both TiO_2 and ZnO which are highly evaluated for UV photocatalysis are inactive under visible light due to their wide bandgaps [118]. On the other hand, hematite is also a preferred photocatalytic material, because its absorption is in the visible region. While compared with ZnO or TiO_2, hematite shows lower photocatalytic efficiency because of corrosion property or the formation of short-lived metal-to-ligand or ligand-to-metal charge transfer states [118]. Worldwide efforts are in progress to make use of sunlight for energy production, environmental protection, and water purification. Sunlight contributes about 5–7% ultraviolet light, 46% visible light and 47% infrared radiation [112]. Hence, inherent are the TiO_2 and ZnO semiconductors which have the inability to make use of the vast potential solar photocatalysis. Various technical methods have been employed to make them absorb photons of lower energy as well [112]. Researchers have been focusing on achieving higher degradation efficiency with these materials, particularly under visible light. In the next section, a brief of explanation about a few methods of improving photocatalytic activity is presented.

1.6.5.6 Methods of improving photocatalytic activity

In order to improve the photocatalytic activity, the way of modifying the surface of the particles is an essential step to prevent the electron–hole recombination.

1.6.5.6.1 Metal ion dopants

The doping of an appropriate material into a catalyst can enhance the photocatalytic performance. Kanade et al. explained that the synthetic strategy for doping of transition metal ions in semiconductor nanostructures would be useful for the improvement of visible light photocatalysts and photovoltaic devices [119]. The transition metal ions (Cu, Co, Mn, and Fe)

substitute for Zn ions with tetrahedral O coordination in ZnO lattice and the result gives the narrow bandgap (visible region) due to the spin exchange interactions which leads the enhancement of photocatalytic activity under visible light [120]. The co-doped ZnO sample having maximum surface oxygen defects proves degrading more methylene blue under visible light [121].

1.6.5.6.2 Nonmetal Doping

Doping with nonmetals [B, C, N, and S] in TiO_2 and ZnO promote the photocatalytic activity in visible light due to the synergetic effect [122]. Shifu et al. explained that the photocatalytic activity of N doped ZnO sample is higher than that of pure ZnO because conductivity conversion of the samples from zinc oxide to nitrogen leads red shift and subsequently improves the photocatalytic activity under visible light [123].

1.6.5.7 Operating and affecting parameters of photocatalysis

The rate of photo mineralization of an organic compound by photocatalysis method primarily depends on the following parameters: structure, shape, size, and surface area of the catalyst, reaction temperature, pH, light intensity, amount of catalyst, and concentration of wastewater [96].

1.6.5.7.1 Crystal Structure, Shape, Size, and Surface Area of Catalyst

The structure of catalyst plays a key role in achieving superior photocatalytic activity. For example, TiO_2 material has three phases such as anatase, rutile, and brookite. But the most sensitive and attractive phase is the anatase phase having a notable photocatalytic activity due to its stability, the position of the conduction band, the higher degree of hydroxylation, and adsorption power [115]. On the other hand, morphology also acts as a potential factor that influences the final degradation efficiency which was reported earlier [124, 125]. Saravanan et al. reported that spherical-shaped ZnO samples show higher efficiency compared with the spindle-and rod-shaped ZnO samples due to its large surface area [126].

Nanomaterials having large surface area and smaller size are compared with bulk materials so that it can effectively show higher efficiency in the photocatalytic reaction. When compared with bulk TiO_2, the nanosized TiO_2 material shows more efficient for water purification and recycling ability due to their smaller size [127].

When the size of the catalyst is smaller, a huge number of atoms are accumulated on the surface of a catalyst which leads to increase in surface to volume ratio. This property enhances number of active sites and interfacial charge carrier transfer rates thereby achieving higher

catalytic activities [127]. And also it is well known that the photocatalytic redox reaction mainly takes place on the surface of the photocatalysts and so the surface properties significantly influence the efficiency of catalyst [126].

1.6.5.7.2 Effect of reaction temperature

A number of researchers have been demonstrated to study the dependence of photocatalytic activity on reaction temperature [96]. During the photocatalytic reaction, when the temperature is raised above 80 °C, it will enhance the electron–hole recombination and desorption process of adsorbed reactant species, resulting in the decrease of photocatalytic activity. The degradation rate dependency on temperature is reflected by the low activation energy (5–20 kJ mol^{-1}) compared with ordinary thermal reactions. Due to photonic activation, heat is not required for photocatalytic systems and can operate at room temperature. The optimum reaction temperature for photocatalytic activity is reported to be in the range of 20–80 °C. When the temperature is at 0 °C, there is an increase in the apparent activation energy [128]. This optimum range mainly depends on the activation energy of the material in the photocatalytic reaction [128].Dissolved oxygen is one of the key elements that drive the photocatalysis, as it helps in scavenging CB electrons and leads to the formation of hydroxyl radicals. The higher or lower temperature causes the change in the percentage of the dissolved oxygen in the samples and hence changes the degradation rate of the reaction. Furthermore, the higher temperatures cause desorption of organic compounds from the photocatalyst surface. Because of the fact that the photocatalytic degradation of the compounds is a surface-based phenomenon, desorption of the pollutant before the reaction with the electrons or holes due to the high temperature results in a decrease of the reaction rate [128].

1.6.5.7.3 Effect of pH

In the photocatalytic reactions, the pH of the solution is a vital factor, since it makes a clear explanation on the surface charge properties of the photocatalyst [129]. The effect of pH on the rate of reaction can be interpreted in terms of electrostatic interactions between charged particles and the contaminants. These influence the adsorption and subsequently the surface properties [129].

1.6.5.7.4 Effect of light intensity

The degradation rate of photocatalytic reaction mostly depends upon the light intensity. The result of photocatalytic reaction responses varied under different wavelengths of the light source [129]. The catalysts TiO_2 and ZnO have a large bandgap (~ 3.2 eV) which absorb mostly in the UV region [129]. The degradation reaction rate varies for different intensities of light as follows; the reaction rate increases with increasing light intensity in the range of 0– 20 mW/cm^2. The excessive light intensity promotes more electron–hole recombination thereby causing decrease in the reaction rate [129].

1.6.5.7.5 Effect of amount of catalyst

The amount of catalyst (sample) also influences the efficiency of photocatalytic degradation. If there is an increase in the quantity of catalyst, the number of active sites on the semiconductor surface increases moreover, which in turn produces number of $OH^{\bullet}$ and $O_2^{\bullet-}$ radicals [96]. As a result, the photocatalytic degradation rate is increased, elucidated that the degradation rate is directly proportional to the catalyst concentration in any reactor system [93]. However, as the catalyst loading is improved beyond an optimum concentration, the degradation rate is unfavourable because there will be decrease in the light penetration depth into the solution and consequently diminishing of light scattering occurs [93].

1.6.5.7.6 Adsorption effect

The physicochemical characteristics of the surface are crucial to define the reactivity of a catalyst, because it is there where the interactions between reactive molecules and the solid occur. Accordingly, adsorption depends not only on the density of sites, but also on their chemical nature, which determines the strength of the bonding with reagents and products. This relevance of surface properties in photocatalysis constitutes an important additional factor to define the efficiency of the process which is basically absent in the case of other semiconductor applications such as photovoltaics [130].

1.6.5.8 Major advantages of photocatalysis

The advantages of this photocatalytic technology are as follows [93, 96, 110, 111].

- Photocatalysis offers a good replacement for the energy-intensive conventional treatment methods (adsorption on activated carbon, ultra filtration, reverse osmosis, coagulation by chemical agents, and ion exchange on synthetic adsorbent resins) with the capacity for using renewable and pollution-free solar energy.

- Photocatalysis leads to the formation of harmless products, unlike conventional treatment measures which transfer pollutants from one phase to another.
- The photocatalytic process can be used in the destruction of a variety of hazardous compounds in different wastewater streams.
- The reaction conditions for photocatalysis are mild, the reaction time is modest and a lesser chemical input is required.
- Minimal of secondary waste generation and It can be applied to hydrogen generation, gaseous phase, and aqueous treatments as well for solid (soil) phase treatments to some extent.

1.6.5.9 Limitations of photocatalysis

The photocatalytic activity depends on the following limitations [93, 110, 111].

- Interfacial charge transfer.
- Improve the charge separation and inhibition of charge carrier recombination.

References of chapter 1

[1] D. S. Ginley, H. Hosono, D.C.Paine, Handbook of Transparent conductors, 978-1-4419-1637-2, Springer New York Heidelberg Dordrecht, London (2011).

[2] H.L. Hartnagel, A.L. Dawar, A.K. Jain, and C. Jagadish, Semiconducting Transparent Thin Films, Institute of Physics, London (1995).

[3]G. Wyszecki, in Handbook of Optics, edited by W.G. Driscoll and W. Vaughan McGrawHill, p. 9 New York (1978).

[4] T. Minami, T. Kakumu, Y. Takeda and S. Takata, Highly transparent and conductive ZnO-In2O3 thin films prepared by dc magnetron sputtering, Thin Solid Films 291, 1–5 (1996).

[5] Brian G. Lewis and David C. Paine, Applications and Processing of Transparent Conducting Oxides, MRS BULLETIN/AUGUST (2000).

[6] K. Badeker, Ann. Phys. (Leipzig) 22 (1907) p. 749.

[7] B.L. Gehman, S. Jonsson, T. Rudolph, M. Scherer, M. Weigert, and R. Werner, Thin Solid Films 220 (1992) p. 333.

[8] T. Blunier, J. Chappellaz, J. Schwander, A. Dallenbach, B. Stauffer, T.F. Stocker, D. Raynaud, J. Jouzel, H.B. Clausen, C.U. Hammer and S.J. Johnsen, Asynchrony of Antarctic and Greenland climate change during the last glacial period, Nature 394, 739–743 (1998).

[9] M.E. Mann, Z.H. Zhang, M.K. Hughes, R.S. Bradley, S.K. Miller, S. Rutherford and F.B. Ni, Proxy-based reconstructions of hemispheric and global surface temperature variations over the past two millennia, Proceedings of the National Academy of Sciences of the United States of America 105, 13252–13257 (2008).

[10] Alaska; Mauna Loa, Atmospheric carbon dioxide dry air mole fractions from quasi-continuous measurements at Barrow, Hawaii; American Samoa; and South Pole, 1973–2006, Version: 200710-01", Version: 2007-10-01, ftp://ftp.cmdl.noaa.gov/ccg/co2/in-situ/ (2007).

[11] W. Haidinger, Handbuch der bestimmenden Mineralogie, (Wien, 1845).

[12] P. Dunn, Franklin and Sterling Hill: the World's Most Magnificent Mineral Deposits, (Excalibur Mineral Company, Peekskill), NY, (2004).

[13] A. A. Somerville, Phys. Rev. I, 34(1912)311 (1912).

[14] O. Fritsch, Ann. Phys, 22(1935)375.

[15] A. R. Hutson, Phys. Rev. Lett., 4(1960)505.

[16] F. S. Hickernell, J. Appl. Phys, 44(1973)1061.

[17] H. Morkoc, U. Özgür, Zinc oxide: fundamentals, materials and device technology. Wiley-VCH, Weinheim, Germany (2009).

[18] JL. Gomez, O. Tigli, Zinc oxide nanostructures: from growth to application, J Mater Sci 48:612–624 (2013).

[19] ZR, Tian, JA, Voigt, J, Liu, B, McKenzie, MJ, McDermott, MA, Rodriguez, H, Konishi, H, Xu, Complex and oriented ZnO nanostructures, Nat Mater 2:821(2003).

[20]V. Cauda, R. Gazia, S. Porro, S. Stassi, G. Canavese, I. Roppolo, and A. Chiolerio, Nanostructured ZnO materials: Synthesis, properties and applications, Handbook of Nanomaterials Properties, Springer-Verlag Berlin Heidelberg (2014).

[21] VV. Pokropivny, VV. Skorokhod, Classification of nanostructures by dimensionality and concept of surface forms engineering in nanomaterial science. Mater Sci Eng C 27:990–993 (2007).

[22] XS. Shen, GZ. Wang, X. Hong, W. Zhu, Nanospheres of silver nanoparticles: agglomeration, surface morphology control and application as SERS substrates. Phys Chem Chem Phys 11:7450–7454 (2009).

[23] B. Weintraub, Z. Zhou, Y. Li, Y. Deng, Solution synthesis of one-dimensional ZnO nanomaterials and their applications. Nanoscale 2:1573–1587 (2010).

[24] H. E. Brown, Zinc Oxide Rediscovered. New Jersey Zinc Company, New York Cammavota V A, Babitzke H R, Hague J M 1975 Mineral Facts and Problems. US Bureau of Mines, Washington, DC, pp. 1223-41, Bell Laboratories, Murray Hill, New Jersey, USA (1957)

[25] AV. Desai, MA. Haque, Mechanical properties of ZnO nanowires, Sens Actuat A Phys 134:169–176 15 (2007).

[26] S. Xu, Y. Qin, C. Xu, Y. Wei, R. Yang, ZL. Wang, Self-powered nanowire devices, Nat Nanotechnol 5:366–373 (2010).

[27] L. Hafsa, L. Hadjeris, L. Herissi,UV-induced photocatalytic degradation of methyl green dye by ZnO nanowires and nanorods obtained by spray pyrolysis, Nano Hybrids and Composites, Vol. 36, pp 69-80 (2022).

[28] L. Hadjeris, L. Herissi, M B. Assouar, T. Easwarakhanthan, J. Bougdira, N. Attaf, M. S. Aida, Transparent and conducting ZnO films grown by spray pyrolysis, Semicond. Sci. Technol. 24 (2009) 035006 (6pp).

[29] L. Herissi, L. Hadjeris, M.S. Aida, S. Azizi, A. Hafdallah and A. Ferdi, Ni-Doped ZnO Thin films deposited by pneumatic spray pyrolysis, Nano Hybrids Compos. 27 (2019) 21-29.

[30] Y. Laaziz, A. Bennouna, N. Chahboun, Outzourhit, A. Amezianne, E. L, Optical characterization of low optical thickness thin films from transmittance and back reflectance measurements. Thin Solid Films, 372, 149 (2000).

[31] MR. Hoffmann, ST. Martin, W. Choi, DW. Bahnemann, Environmental applications of semiconductor photocatalysis. Chem Rev 95:69–96 (1995).

[32] W. Doerffler, K. Hauffe, Heterogeneous photocatalysis. The influence of oxidizing and reducing gases on the electrical conductivity of dark and illuminated zinc oxide surfaces. J Catal 3:156–170 (1964)

[33] GH. Lee, T. Kawazoe, M. Ohtsu, Difference in optical band gap between zinc-blende and wurtzite ZnO structure formed on sapphire (0001) substrate. Solid State Commun 124:163–165(2002).

[34] LQ. Jing, ZL. Xu, J. Shang, XJ. Sun, WM. Cai, HC. Guo, The preparation and characterization of ZnO ultrafine particles. Mater Sci Eng A, Struct Mater, Prop Microstruct Process 332:356–361(2002).

[35] S. Rehman, R. Ullah, AM. Butt, ND. Gohar, Strategies of making TiO_2 and ZnO visible light active. J Hazard Mater 170:560–569 (2009).

[36] HL. Liu, TCK. Yang, Photocatalytic inactivation of Escherichia coli and Lactobacillus helveticus by ZnO and TiO_2 activated with ultraviolet light. Process Biochem 39:475–481(2003).

[37] L. Tang, D. Sallet, J. Lemaire, Photochemistry of polyundecanamides. 2. TiO_2-photocatalyzed and ZnO-photocatalyzed oxidation, Macromolecules 15:1437–1441(1982).

[38] C. Minero, E. Pelizzetti, P. Piccinini, M. Vincenti, Photocatalyzed transformation of nitrobenzene on TiO_2 and ZnO, Chemosphere 28:1229–1244(1994)

[39] D. C. Look, B. Clafin,Y. I.Alivov, S. J. Park, Phys. Stat. Sol. (a) 201 (2004) 2203.

[40] S.J.Pearton, D.P.Norton, K.Ip, Y.W.Heo, T.Steiner, Prog.Mater.Sci.50 (2005)293.

[41] R. M. Cornell, U. Schwertmann, The Iron Oxides, Structure, Properties, Reactions, Occurrence and Uses, Wiley–VCH, Weinheim, Germany, pp. 664 (2003).

[42] A. F.Wells, Structural Inorganic Chemistry, 5th edition, Oxford University Press, Oxford, UK, pp. 1382 (1991).

[43] J. Jolivet, Metal Oxide Chemistry and Synthesis. From Solution to Solid State, Wiley, Chichester,pp. 321 (2000).

[44] J. Jolivet, E. Tronc, C.Chaneac, Iron oxides: From molecular clusters to solid. A nice example of chemical versatility, C. R. Geoscience, 338, pp. 488-497 (2006).

[45] J. M. Bigham, R. W. Fitzpatrick, Iron Oxides, Chapter 10, Soil Mineralogy with Environmental Applications. SSSA Book Series No.7, (2002).

[46] A. H. Morrish, , Canted Antiferromagnetism: Hematite, World Scientific, London, UK, (1994)

[47] L. Pauling, S. B. Hendricks, The crystal structures of hematite and corundum, Journal of the American Chemical Society, pp 47, 781-790 (1925).

[48] Y.Cudennec, A.Lecerf, Topotactic transformations of goethite and lepidocrocite into hematite and maghemite, Solid State Sciences, pp7. 520-529 (2005).

[49] R. M. Cornell, U.Schwertman, , The Iron Oxides, 2nd edition, WileyVCH Verlag Gmbh & Co. KGaA, Weinheim (2003).

[50] C. Pulgarin, J. Kiwi, Iron Oxide-Mediated Degradation, Photodegradation, and Biodegradation of Aminophenols, Langmuir, pp 11. 519-526 (1995).

[51] M. Pelino, C. Colella, C.Cantallini, M. Faccio, G. Ferri, A. D'Amico, Microstructure and electrical properties of an α-hematite ceramic humidity sensor, Sensors and Actuators B: Chemical, pp 7. 464-469 (1992).

[52] C. Wu, P. Yin, X. Zhu, C. OuYang, Y. Xie, , Synthesis of Hematite (αFe_2O_3) Nanorods: Diameter-Size and Shape Effects on Their Applications in Magnetism, Lithium Ion Battery, and Gas Sensors, Journal of Physical Chemistry B, pp 110. 17806-17812 (2006).

[53] K. J. Widder, A. E. Senyei, D. G. Scarpelli, , Magnetic microspheres: a model system for site specific drug delivery in vivo, Proceedings of the Society for Experimental Biology and Medicine, pp 58. 141-146 (1978).

[54] G.Garcon, S.Garry, P.Gosset, F.Zerimech, A.Martin, M.Hannothiaux, P.Shirali, Benzo (a) pyrene-coated onto Fe_2O_3 particles-induced lung tissue injury: role of free radicals, Cancer Letters, pp167.7-15 (2007).

[55] R. Lawaczeck, M.Menzel, H. V. Pietsch, Superparamagnetic iron oxide particles: contrast media for magnetic resonance imaging, Applied Organometallic Chemistry, pp18. 506-513 (2004).

[56] M. Busch, M. Gruyters, H. Winter, Spin polarization and structure of thin iron oxide layers prepared by oxidation of Fe (1 1 0), Surface Science, pp 600. 4166-4169 (2006).

[57] D. Walter, Characterization of synthetic hydrous hematite pigments Thermochimica Acta, pp 445. 195-199 (2006).

[58] J. Scamehorn, An overview of Phenomena Involving Surfactant Mixtures, In Phenomena in Mixed Surfactant Systems, ACS Symposium Series, American Chemical Society, Washington, DC (1986).

[59] A. Lassoued, Control of the shape and size of iron oxide (α-Fe_2O_3) nanoparticles synthesized through the chemical precipitation method. Results in physics, p7. 3007-3015 (2017).

[60] M. Mishra, D.-M. Chun, rmalpha-Fe_2O_3 as a Photocatalytic material: A Review, Applied Catalysis A, General (2015).

[61] M. J. Katz, S. C. Riha, N. C. Jeong, A. B. F. Martinson, O. K. Farha, J. T. Hupp, Coord. Chem. Rev. 256(2012) 2521-2529 (2012).

[62] A.J. Bosman, H.J. van Daal, Adv. Phys. 19 (77) (1970).

[63] T. Nakau, J. Phys. Soc. Jpn 15 (1960) 727.

[64] D. Benjelloun, J.-P. Bonnet, J.-P. Doumerc, J.-C. Launay, M. Onillon, P. Hagenmuller, Mater. Chem. Phys. 10 (1984) 503.

[65] K.M. Rosso, D.M.A. Smith, M. Dupuis, J. Chem. Phys. 118 (14) (2003) 6455.

[66] S. Kerisit, K.M. Rosso, Geochim. Cosmochim. Acta 70 (8) (2006) 1888.

[67] K. Cheng, et al., Quantum size effect on surface photovoltage spectra: alpha-Fe_2O_3 nanocrystals on the surface of monodispersed silica microsphere. The Journal of Physical Chemistry B, 2006. 110: p. 7259-7264.

[68] X. Xu, et al., Spindle-like mesoporous α-Fe_2O_3 anode material prepared from MOF template for high-rate lithium batteries. Nano letters, 12: p. 4988-4991 (2012).

[69] X.-F. Lu, et al., α-Fe_2O_3@ PANI core–shell nanowire arrays as negative electrodes for asymmetric supercapacitors. ACS applied materials & interfaces, 7(27): p. 14843-14850 (2015).

[70] M. Benelmekki, A. Erbe : Nanostructured thin films background, preparation and relation to the technological revolution of the 21st century. Nanostructured Thin Films, ISBN 978-0-08-102572-7, (2019)

[71] X. Li, M. Rui, J. Song, Z. Shen and H. Zeng, Adv. Funct Mater, 25, 4929, (2015).

[72] Ohring, Milton. Materials science of thin films: depositon & structure. Elsevier, (2001).

[73] A.K. Alves, C.P. Bergmann, F.A. Berutti. : Novel synthesis and characterization of nanostructured materials. Engineering materials Book, 1612-1317, Porto Alegre Brazil (2013).

[74] D.Perednis, Thin film deposition by spray pyrolysis and the application in solide oxide fuel cells. Ph.D. Thesis, Swiss Federal Institute of Technology Zurich (2003).

[75] A.R. Balkenende, A. Bogaerts, J.J. Scholtz, R.R.M. Tijburg, H.X. Willems, Thin MgO layers for effective hopping transport of electrons. Philips J. Res. 50, 365–373 (1996).

[76] W.Yoon, K.Y. Chung, K. Nam, K.Kim,: Characterization of $LiMn_2O_4$-coated $LiCoO_2$ film electrode prepared by electrostatic spray deposition. J. Power Sources 163, 207–210 (2006).

[77] M. Konarova, I.Taniguchi, Preparation of $LiFePO_4$/C composite powders by ultrasonic spray pyrolysis followed by heat treatment and their electrochemical properties. Mater. Res. Bull. 43, 3305–3317 (2008).

[78] R.M.Trommer, Obtenção e caracterização de revestimentos de hidroxiapatita sobre substratos de aço inoxidável 316L utilizando a técnica de deposição química de vapor assistida por chama. Master Thesis, Universidade Federal do Rio Grande do Sul, Brazil (2006).

[79] S.C. Zhang, G.L. Messing, Synthesis of solid, spherical zirconia by spray pyrolysis. J. Am. Ceram. Soc. 73, 61–67 (1990).

[80] T.Q. Liu, O. Sakurai, N. Mizutani, M. Kato,: Preparation of spherical zirconia fine ZnO particles by spray pyrolysis method using ultrasonic atomization techniques. J. Mater. Sci. 21, 3698–3702 (1986).

[81] K.L.Choy, B.Su, Growth behavior and microstructure of CdS thin films deposited by an electrostatic spray assisted vapor deposition (ESAVD) process. Thin Solid Films 388, 9–14 (2001).

[82] A.Kufferath, B.Wende, W.Leuckel, Influence of liquid flow conditions on spray characteristics of internal-mixing twin-fluid atomizers. Int. J. Heat Fluid Flow 20, 513–519 (1999).

[83] I.Taniguchi, D.Song, M.Wakihara, Electrochemical properties of $LiM_{1/6}Mn_{11/6}O_4$ (M = Mn, Co., Al and Ni) as cathode materials for Li-ion batteries prepared by ultrasonic spray pyrolysis method. J. Power Sources 109, 333–339 (2002).

[84] K.D.Kihm, N.Chigier, Effect of shock waves on liquid atomization of a two-dimensional airblast atomizer. Atomization Sprays 1, 113–136 (1991).

[85] C.H. Chen, E.M.Kelder, P.J.J.M.Van Der Put, J. Schoonman, Morphology control of thin $LiCoO_2$ films fabricated using the electrostatic spray deposition (ESD) technique. J. Mater. Chem. 6, 765–771 (1996)

[86] C.H.Chen, K.N.Varhaug, J.Schonman, Coatings yttria-stabilized-zirconia (YSZ) thin films on gadolinia-doped ceria (GCO) by the electrostatic spray deposition (ESD) technique. J. Mater. Synth. Process. 4, 189–194 (1996).

[87] H. Ruiz, H. Vesteghem, A.R. Giampaolo, J. Lira, Zircônia coatings by spray pyrolysis. Surf. Coat. Technol. 89, 77–81 (1997).

[88] H.A. Hamedani, Dahmen, H. Peydaye-Saheli, H. Garmestani, M. Khaleel, Fabrication of gradient porous LSM cathode by optimizing deposition parameters in ultrasonic spray pyrolysis. Mater. Sci. Eng. B 153, 1–9 (2008).

[89] N.S.A. Mutamim, Z.Z. Noor, M.A.A. Hassan, G. Olsson, Application of membrane bioreactor technology in treating high strength industrial wastewater: a performance review, Desalination 305, 111 (2012).

[90] R. Das, Application photocatalysis for treatment of industrial waste water—a short review. Open Acc. Lib. J. 1, 117 (2014).

[91] U.G .Akpan, B.H .Hameed, Parameters affecting the photocatalytic degradation of dyes using TiO_2-based photocatalysts: a review. J Hazard Mater 170(2–3):520–529 (2009).

[92] V.K. Gupta, I. Ali, T.A. Saleh, A. Nayak, S. Agarwal, Chemical treatment technologies for waste-water recycling—an overview. RSC Adv 2(16):6380 (2012).

[93] I.K. Konstantinou, T.A. Albanis, TiO2-assisted photocatalytic degradation of azo dyes in aqueous solution: kinetic and mechanistic investigations. Appl Catal B 49(1):1–14 (2004)

[94] R.P. Schwarzenbach, T. Egli, T.B. Hofstetter, U. von Gunten, B. Wehrli, Global water pollution and human health. Annu Rev Environ Resour 35(1):109–136 (2010).

[95] B. Chong Jin, C.W.K. Chow, C. Saint, Recent developments in photocatalytic water treatment technology: a review. Water Res 44(10):2997–3027 (2010).

[96] K. Rajeshwar, M.E. Osugi, W. Chanmanee, C.R. Chenthamarakshan, M. Zanoni, P. Kajitvichyanukul, R. Krishnan-Ayer, Heterogeneous photocatalytic treatment of organic dyes in air and aqueous media. J Photochem Photobiol C 9(4):171–192 (2008)

[97] U. Pagga, D. Brown, The degradation of dyestuffs: part II behaviour of dyestuffs in aerobic biodegradation tests. Chemosphere 15(4):479–491(1986)

[98] KR Jegannathan, PH Nielsen, Environmental assessment of enzyme use in industrial production—a literature review. J Clean Prod 42:228–240 (2013)

[99]V. K. Gupta and Suhas, Application of low-cost adsorbents for dye removal - A review, Journal of Environmental Management, 90, 2313-2342 (2009).

[100] M. Shakeri and M. Shoda, Efficient decolorization of an anthraquinone dye by recombinant dye-decolorizing peroxidase (rDyP) immobilized in silica-based mesocellular foam, Journal of Molecular Catalysis B: Enzymatic, 62, 277-281 (2010).

[101] J. Pierce, Colour in textile effluents - the origins of the problem, Journal of the Society of Dyers & Colourists, 110, pp 131-133 (1994).

[102] S. Esplugas, D.M. Bila, L.G.T. Krause, M. Dezotti, Ozonation and advanced oxidation technologies to remove endocrine disrupting chemicals (EDCs) and pharmaceuticals and personal care products (PPCPs) in water effluents. J Hazard Mater 149(3):631–642 (2007)

[103] H.K. Moo Young, Pulp and paper effluent management. Water Environ Res 79(10):1733–1741(2007).

[104] P.R. Gogate, A.B. Pandit, A review of imperative technologies for wastewater treatment II: hybrid methods. Adv Environ Res 8(3–4):553–597(2004).

[105] M.B. Johnson, M. Mehrvar, Aqueous metronidazole degradation by UV/H_2O_2 process in single-and multi-lamp tubular photoreactors: kinetics and reactor design. Ind Eng Chem Res 47 (17):6525–6537 (2008).

[106] H.M. Coleman, B.R. Eggins, J. Byrne, F.L. Palmer, E. King, Photocatalytic degradation of 17-b-oestradiol on immobilised TiO_2. Appl Catal B 24(1):L1–L5 (2000).

[107] I. Oller, S. Malato, J.A. Sanchez-Perez, Combination of advanced oxidation processes and biological treatments for wastewater decontamination, a review. Sci Total Environ 409 (20):4141–4166 (2011).

[108] N. Serpone, S. Horikoshi, A.V. Emeline, Microwaves in advanced oxidation processes for environmental applications. A brief review. J Photochem Photobiol C 11(2 3):114–131(2010).

[109] A. Fujishima, K. Honda, Electrochemical photolysis of water at a semiconductor electrode. Nature 238(5358):37–38 (1972).

[110] A. Fujishima, T.N Rao, D.A Tryk, Titanium dioxide photocatalysis. J Photochem Photobiol C 1(1):1–21(2000).

[111] S. Rehman, R. Ullah, A.M. Butt, N.D. Gohar, Strategies of making TiO_2 and ZnO visible light active. J Hazard Mater 170(2–3):560–569 (2009).

[112] B. Ohtani, Chapter "Principle of Photocatalysis and Design of Active Photocatalysts", Catalysis Research Center, Hokkaido University, Sapporo 001-0021, Japan (2013).

[113] J. Hagen Industrial catalysis: a practical approach/Jens Hagen, 2nd edn. Wiley, Weinheim (2006).

[114] R. Saravanan, F. Gracia, A. Stephen, Basic Principles, Mechanism, and Challenges of Photocatalysis, Springer Ser. Polym. Compos. Mater. 2 (2017) 19 40 (2017).

[115] M.M. Khan, S.F. Adil, A. Al-Mayouf, Metal oxides as photocatalysts, J Saudi Chem Soc 19 (5):462–464(2015)

[116] Y.I. Choi, S. Lee, S.K. Kim, Y. Kim, D.W. Cho, M.M. Khan, Y. Sohn, Fabrication of ZnO, ZnS, Ag-ZnS, and Au-ZnS microspheres for photocatalytic activities, CO oxidation and 2-hydroxyterephthalic acid synthesis. J Alloy Compd 675:46–56 (2016).

[117] L. Zhang, H. Yang, X. Xie, F. Zhang, L. Li, Preparation and photocatalytic activity of hollow ZnSe microspheres via Ostwald ripening. J Alloy Compd 473(1–2):65–70 (2009).

[118] M.A. Fox, M.T. Dulay, Heterogeneous photocatalysis, Chem Rev 93(1):341–357 (1993).

[119] K.G. Kanade, B.B. Kale, J.O. Baeg, S.M. Lee, C.W. Lee, S.J. Moon, H. Chang, Self-assembled aligned Cu doped ZnO nanoparticles for photocatalytic hydrogen production under visible light irradiation. Mater Chem Phys 102:98–104 (2007).

[120] K. Milenova, I. Avramova, A. Eliyas, V. Blaskov, I. Stambolova, N. Kassabova, Application of activated M/ZnO (M = Mn Co, Ni, Cu, Ag) in photocatalytic degradation of diazo textile coloring dye, Environ Sci Pollut Res Int 21(21):12249–12256 (2014).

[121] Q. Xiao, J. Zhang, C. Xiao, X. Tan, Photocatalytic decolorization of methylene blue over Zn_1-xCo_xO under visible light irradiation. Mater Sci Eng B 142(2–3):121–125 (2007).

[122]S. In, A. Orlov, R. Berg, F. Garcia, S. Pedrosa-Jimenez, M.S. Tikhov, D.S. Wright, R.M. Lambert, Effective visible light-activated B-doped and B, N-codoped TiO_2 photocatalysts, J Am Chem Soc 129(45):13790–13791(2007).

[123] C. Shifu, Z. Wei, Z. Sujuan, L. Wei, Preparation, characterization and photocatalytic activity of N-containing ZnO powder, Chem Eng J 148(2–3):263–269 (2009).

[124] H. Wang, C. Xie, W. Zhang, S. Cai, Z. Yang, Y. Gui, Comparison of dye degradation efficiency using ZnO powders with various size scales. J Hazard Mater 141(3):645–652 (2007).

[125] Y. Wang, X. Li, G. Lu, G. Chen, Y. Chen, Synthesis and photo-catalytic degradation property of nanostructured-ZnO with different morphology, Mater Lett 62(15):2359–2362 (2008).

[126] R. Saravanan, V.K. Gupta, V. Narayanan, A. Stephen, Comparative study on photocatalytic activity of ZnO prepared by different methods. J Mol Liq 181:133–141 (2013).

[127] G. Cernuto, N. Masciocchi, A. Cervellino, G.M. Colonna, A .Guagliardi, Size and shape dependence of the photocatalytic activity of TiO_2 nanocrystals: a total scattering Debye function study. J Am Chem Soc 133(9):3114–3119 (2011).

[128] D. Chatterjee, S. Dasgupta, Visible light induced photocatalytic degradation of organic pollutants. J Photochem Photobiol C 6(2–3):186–205 (2005).

[129] K.M. Reza, A.S. Kurny, F. Gulshan , Parameters affecting the photocatalytic degradation of dyes using TiO_2: a review. Appl Water Sci. doi:10.1007/s13201-015-0367-y (2015).

[130] F. BT. Abubakar, Towards new generation of sustainable catalysts: Study of shape and size controlled TiO_2 nanoparticles in photocatalytic degradation of industrial dye. Thesis university of canterbury (New Zeland) (2014).

Chapter 2

Characterization methods

2 Characterization methods

This chapter describes the general experimental techniques used throughout this thesis.

2.1 UV-Vis spectrophotometry

2.1.1 Introduction

Ultraviolet and visible spectrometers have been in general use for the last 35 years and over this period have become the most important analytical instrument in the modern day laboratory. In many applications other techniques could be employed but none rival UV-Visible spectrometry for its simplicity, versatility, speed, accuracy and cost-effectiveness [1].

The different components of light are characterized by a specific wavelength. The sum of all components i.e. of all wavelengths is called a spectrum. More specifically, a spectrum represents a distribution of radiant energy. For instance, the electromagnetic spectrum of visible light ranges from approximately 390 nm up to approximately 780 nm (figure 2.1) [2].

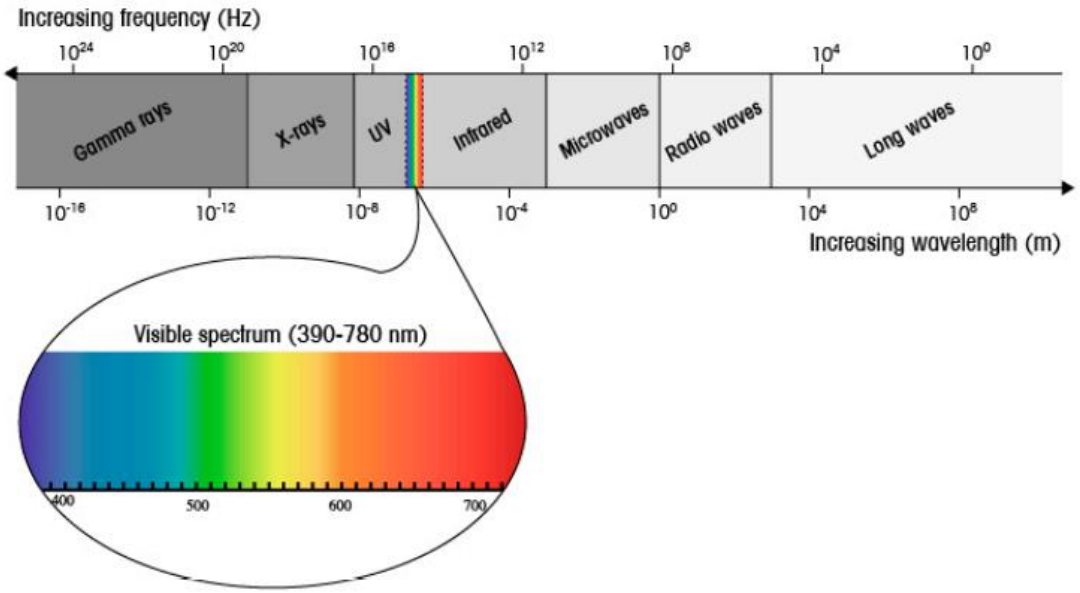

Figure 2.1: The visible spectrum (390 – 780 nm) represents only a small portion of the whole electromagnetic spectrum [3].

2.1.2 Measurement principle

A UV/VIS spectrophotometer measures the intensity of light passing through a sample solution in a cuvette, and compares it to the intensity of the light before it passes through the sample. The main components of a UV/Vis spectrophotometer are a light source, a sample

holder, a dispersive device to separate the different wavelengths of the light (e.g. a monochromator), and a suitable detector (figure 2.2) [4].

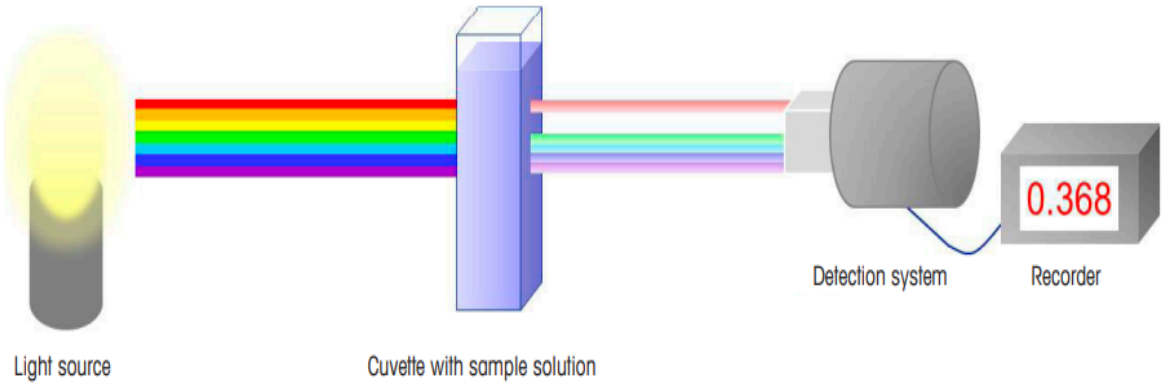

Figure 2.2: Measurement principle in UV/Vis spectroscopy [4]

The working principle of a spectrophotometer is based on the following steps:

2.1.2.1 Blank (measure of the intensity of light transmitted through the solvent):

1. The solvent (e.g. water or alcohol) is added into a suitable, transparent and not absorbing container – a cuvette.

2. A light beam emitted by the light source passes through the cuvette with the solvent.

3. The intensity of the transmitted light at different wavelengths is then measured by a detector positioned after the cuvette with the solvent and recorded.

This is known as the blank, which is needed for the sample measurement [5].

2.1.2.2 Sample determination:

1. A sample is dissolved in the solvent and added into the cuvette.

2. A light beam emitted by the light source passes through the cuvette with the sample.

3. When passing through the cuvette, the light is partially absorbed by the sample molecules in the solution.

4. The transmitted light is then measured by the detector.

5. The light intensity change at different wavelengths is calculated by dividing the transmitted intensity of the sample solution by the corresponding values of the blank. This ratio is finally stored by a recorder [6].

2.1.3 Transmittance and absorbance

The detector in a UV/Vis spectrophotometer measures the intensity of light after passing through the sample solution. This fraction of light collected by the detector is called the transmitted intensity, **I**. The intensity of the transmitted light is attenuated by the sample solution due to, for instance, absorption of light at specific wavelengths. Therefore, its value is lower than the original intensity $\mathbf{I_0}$ at the light source (figure 2.3) [7].

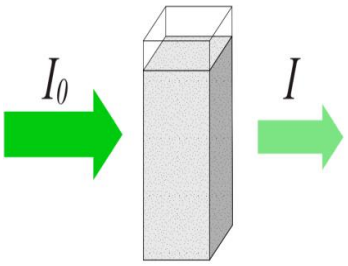

Figure 2.3: Light attenuation by absorption of sample molecules in solution [7].

The ratio between the two intensities I / I_0 is defined as Transmittance T (equation 2.1).

$$T = \frac{I}{I_0} \qquad (2.1)$$

The transmittance is the main value determined by UV-Vis spectroscopy, but it is not the only one. In fact, the absorbance **A** represents an additional result widely used when recording UV-Vis spectra. It is defined as the negative logarithm of the transmittance (equation 2.2).

$$A = -\log(T) \qquad (2.2)$$

Note that the absorbance **A** does not have any unit of measurement. In other words, it is a dimensionless value [6, 7].

2.1.3.1 Lambert-Beer law

When passing through a transparent cuvette filled with sample solution, the light intensity is attenuated proportionally to the sample concentration. In other words, a higher concentrated sample solution will absorb more light. In addition, the attenuation is also proportional to the length of the cuvette; a longer cuvette will lead to a higher absorption of light [4].

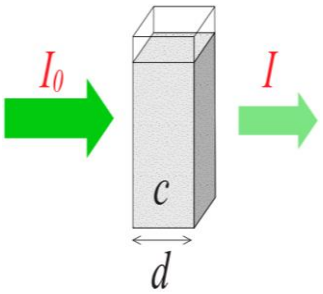

Figure 2.4: The attenuation of the light intensity is proportional to the concentration of the sample solution as well as the length of the cuvette [7].

Both factors can be summarized by expressing the absorbance **A** as a function of the concentration and of the cuvette length (equation 2.3). In particular, the absorbance **A** is equal to the product of the extinction coefficient **ε**, the concentration **c** and the path length **d**:

$$A = \varepsilon \,.\, c \,.\, d \qquad (2.3)$$

This relationship is called the Lambert-Beer law where [6]:

1. The sample concentration **c** is given in mol/l,

2. The path length **d** of the cuvette is given in cm,

3. The extinction coefficient **ε** (epsilon) is a sample specific constant describing how much the sample is absorbing at a given wavelength (in l/ (cm*mol).

2.1.4 Spectrophotometer Design

A spectrophotometer generally consists of four components (figure 2.5):

1. A suitable **light source** which covers the UV-Vis spectrum of interest. In general, a lamp containing a gas such as xenon, or a combination of two different lamps such as tungsten/deuterium is used.

2. An appropriate **sample holder** is needed to hold the sample.

- **Liquid samples** are placed in cuvettes, which can be made of quartz, borosilicate glass or acrylic plastic. However, glass and acrylic plastic do not transmit UV light and should only be used for measurements in the visible light range

- **Solid samples** can be mounted into a suitable holder to be positioned in the optical path of the spectrophotometer for measurement of the transmitted light.

3. A **dispersion element** is needed to distribute the light into separate wavelengths. It can be either a quartz prism or a diffraction grating, i.e. an optical component with a periodic structure able to diffract light.

4. Finally, the transmitted light intensity is recorded by a suitable **detector** such as photomultiplier, a multichannel array (e.g. a photodiode array, or PDA), or a charge-coupled device (CCD), similarly to a digital camera. Both PDA and CCD detectors use a photosensitive semiconductor material to convert the light into an electronic signal which is then recorded by the instrument [8].

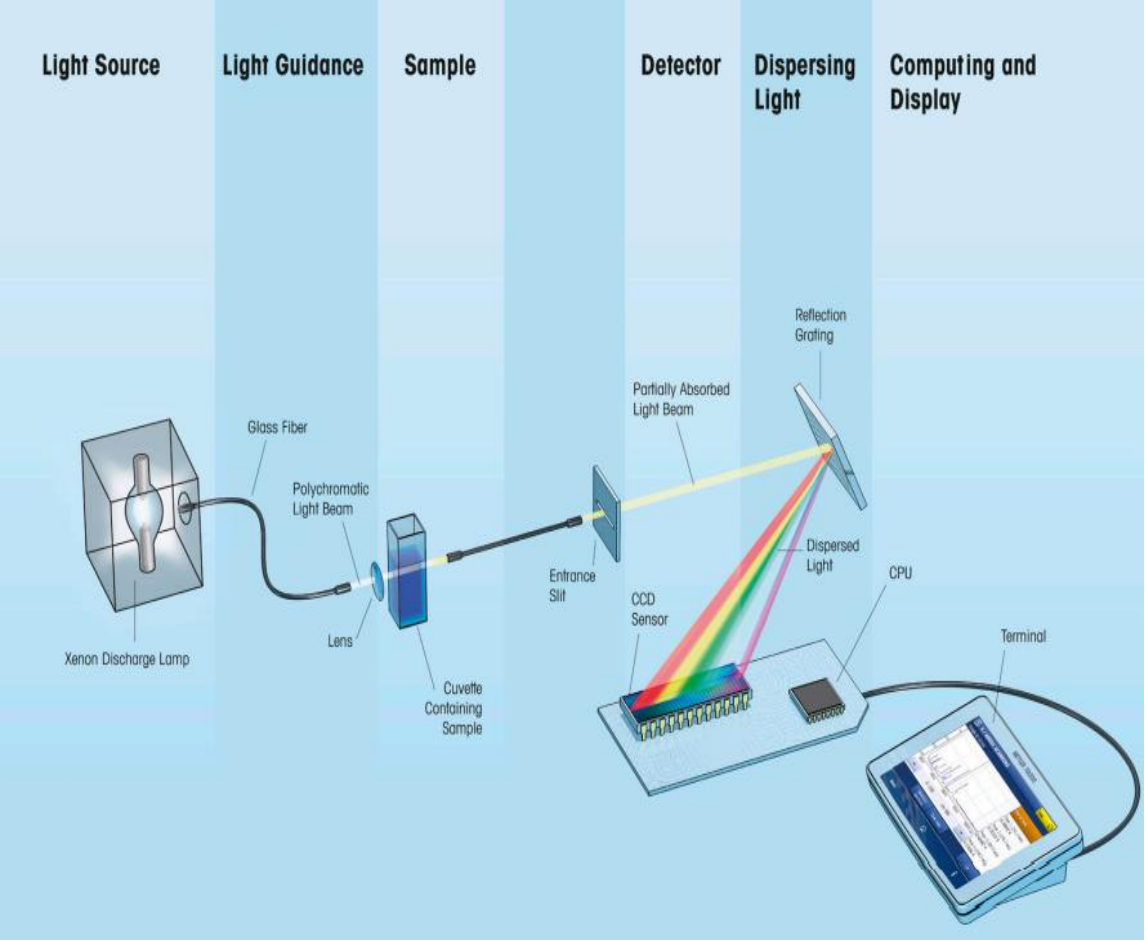

Figure 2.5: Cuvette-based single-beam array spectrophotometer [7].

2.1.5 Determination of band gap energy from UV-Vis spectra

An ideal UV-Vis spectrum for a perfect direct band gap semiconductor exhibits almost no absorption for photons with energies below the band gap and a sharp increase in absorption for photons above the band gap. Since spectra are typically reported in units corresponding to the wavelength of light rather than its energy, the conversion between wavelength (nm) and band gap energy (eV) units is achieved by (equation 2.4):

$$h\upsilon(eV) = \frac{hc}{\lambda} = \frac{1239.8}{\lambda\,(nm)} \qquad (2.4)$$

The band gap in the absorption spectrum corresponds to the point at which absorption begins to increase from the baseline, since this indicates the minimum amount of energy required for a photon to excite an electron across the band gap and thus be absorbed in the semiconductor material [9].

Tauc Plot Method was first developed by Tauc in 1968 [10]. This method gained popularity when research on thin layers began to develop rapidly [11, 12]. At that time, scientists were competing to conduct experiments in searching for new materials. Calculation of energy gap value using the Tauc Plot method is started by calculating the absorption coefficients (α), (equation 2.5):

$$\alpha = \frac{1}{d}\ln\left[\frac{100}{T(\lambda)}\right] \qquad (2.5)$$

where T = Transmittance value from UV/Vis spectrometer and d = sample width (cm).

According to Tauc, the energy gap values can be obtained from the following equation (2.6):

$$(\alpha h\upsilon)^{1/m} = B(h\upsilon - E_g) \qquad (2.6)$$

where h = Planck's constant (4.135×10^{-15} eV.s), υ = frequency (s^{-1}), B = a comparative constant, E_g = energy gap (eV).

m indicates the type of electronic transition, with values for different transitions being [11]:

- ½ = Direct.
- 3/2 = Direct forbidden.
- 2 = Indirect.
- 3 = Indirect forbidden

The optical energy gap E_g can be estimated by extrapolating to the hν-axis, the linear part of the $(\alpha h\nu)^{1/m}$ vs. hν curve (figure 2.6).

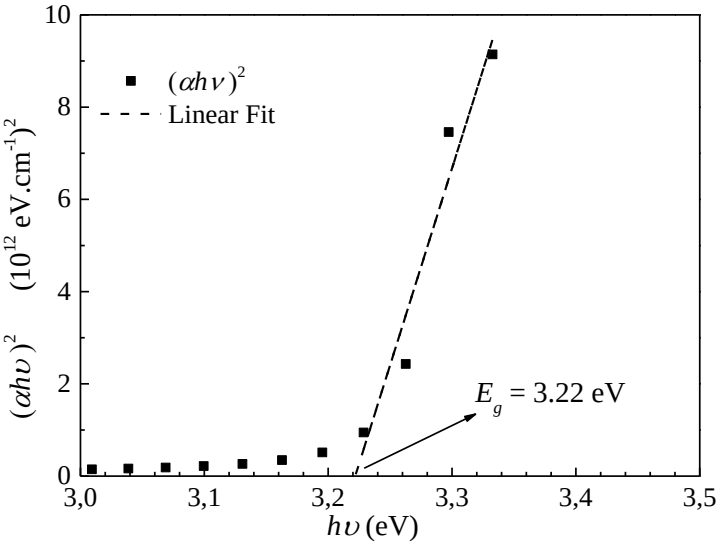

Figure 2.6: Determination of the optical energy gap (E_g) for ZnO Sample.

For values of $\alpha < 10^4$ cm^{-1}, an exponential tail often exists for many materials (such us powders) that cannot be modeled by Tauc equation. The kubelka-Munk function is proportional to the absorption coefficient α (equation 2.7) [11]:

$$[F(R_\infty)h\upsilon]^{1/m} = B(h\upsilon - E_g) \qquad (2.7)$$

where R_∞ is the reflectance of the sample with 'infinite thickness'.

The $(\alpha h\upsilon)^{1/m}$ vs. hυ graph is plotted and the energy-band gap of the powder sample is extracted easily.

2.1.6 Determination of Urbach energy parameter from UV- Vis spectra

Generally, in optical absorption, near band edges, an electron from the top of the valence band gets excited into the bottom of the conduction band across the energy band gap [13]. During this transition process, if these electrons encounter disorder, it causes density of their states ρ (hν), where hν is the photon energy, tailing into the energy gap. This tail of ρ (hν) extending into the energy band gap is termed as Urbach tail. Consequently, absorption coefficient α(hν) also tails off in an exponential manner and the energy associated with this tail is referred to as Urbach energy and can be calculated by the following equation (2.8):

$$\alpha = \alpha_0 exp\left(\frac{h\nu}{E_{Urb}}\right) \qquad (2.8)$$

where α_o is a constant, 'hν' is the photon energy and E_{Urb} is the Urbach energy [14, 15].

The Urbach energy is estimated by plotting log (α) vs. hν and fitting the linear portion of the curve with a straight line. The reciprocal of the slope of this linear region yields the value of E_{urb} (figure 2.7).

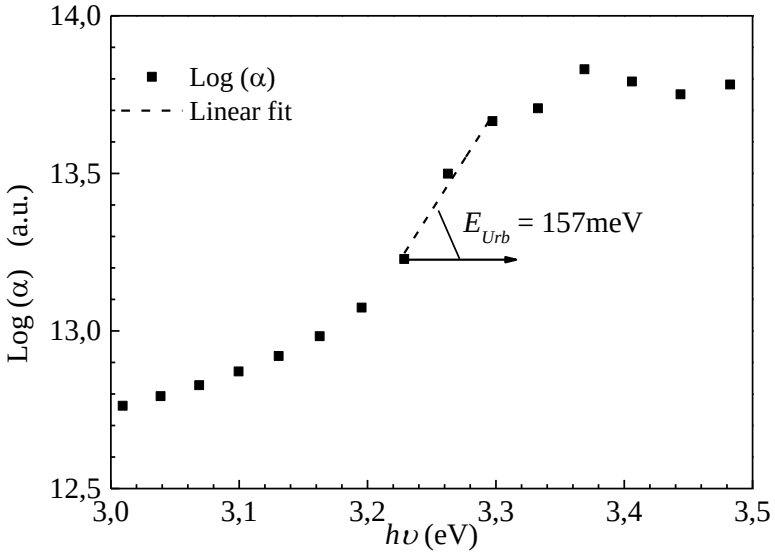

Figure 2.7: Determination of the Urbach energy parameter (E_{Urb}) for ZnO sample.

In this work, some parameters of the optical properties of thin films were determined by exploiting curves representing the variation of the transmittance as a function of the wavelength in the field of UV-Vis. We used a UV-Vis spectrophotometer of the type (JASCO V-630) at LMSSEF laboratory whose spectral range extends from the UV-Vis (190 nm-1100 nm) presented in figure 2.8.

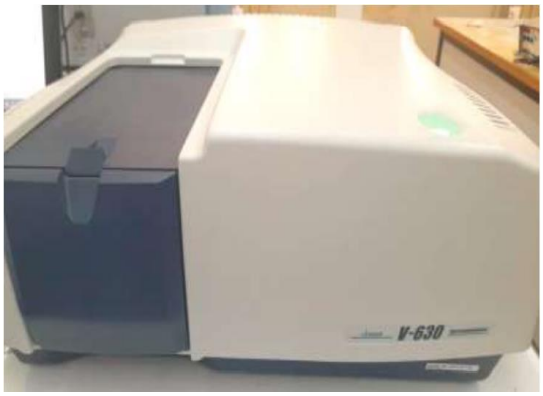

Figure 2.8: (JASCO V-630) UV- Vis spectrophotometer.

2.2 X-ray diffraction (XRD) techniques

2.2.1 Introduction

The discovery of X-rays by Wilhelm Conrad Roentgen in 1895 allowed important innovations in all scientific disciplines, making the development of new medical and technical applications possible [16]. In particular, the research on X-ray diffraction (XRD) by crystals initiated by Laue, Friedrich, and Knipping in 1912 opened new possibilities in the study of crystalline materials [17]. Since then, these methods have been further developed to become very powerful tools in the fields of materials science and engineering. Since the discovery of X-rays and the first experiments on XRD by crystals, XRD methods have become very powerful state of the art techniques for advanced material characterization. The XRD methods are based on the ability of crystals to diffract X-rays in a characteristic manner allowing a precise study of the structure of crystalline phases. Recorded diffraction patterns contain additive contributions of several micro- and macrostructural features of a sample. With the peak position, lattice parameters, space group, chemical composition, macrostresses, or qualitative phase analysis can be investigated. Based on the peak intensity, information about crystal structure (atomic positions, temperature factor, or occupancy) as well as texture and quantitative phase analyses can be obtained. Finally, the peak shape gives information about sample broadening contributions (microstrains and crystallite size)[18].

2.2.2 Principles of X-ray diffraction techniques

2.2.2.1 Generation of X-ray radiation

X-rays are high-energy electromagnetic waves with a wavelength between 10^{-3} and10^{1} nm [19]. The generation of X-rays is generally achieved by the use of sealed tubes, rotating anodes or synchrotron radiation sources. Sealed tubes and rotating anodes, which are used in laboratory equipment, both produce X-rays by the same principle. Electrons generated by heating a tungsten filament in a vacuum are accelerated through a high potential field and then directed to a target which then emits X-rays.

The incident electrons induce two effects leading to the generation of X-rays: the first is the deceleration of the electrons leading to the emission of X-ray photons with a broad continuous distribution of wavelength, also called *Bremsstrahlung* [20]. The second is the ionization of the impinged atoms by ejecting electrons from the inner shells. In order to get a more stable state, electrons from outer shells “jump” into these gaps. The difference between the electron energies of the inner shell and of the incoming electron is emitted in the form of

photons, with a characteristic energy depending on the initial and final shell position of the electrons and on the material as shown exemplarily in figure 2.9 [20]. The characteristic radiation requires minimum excitation potential of the electrons to be emitted, which depends on the target material.

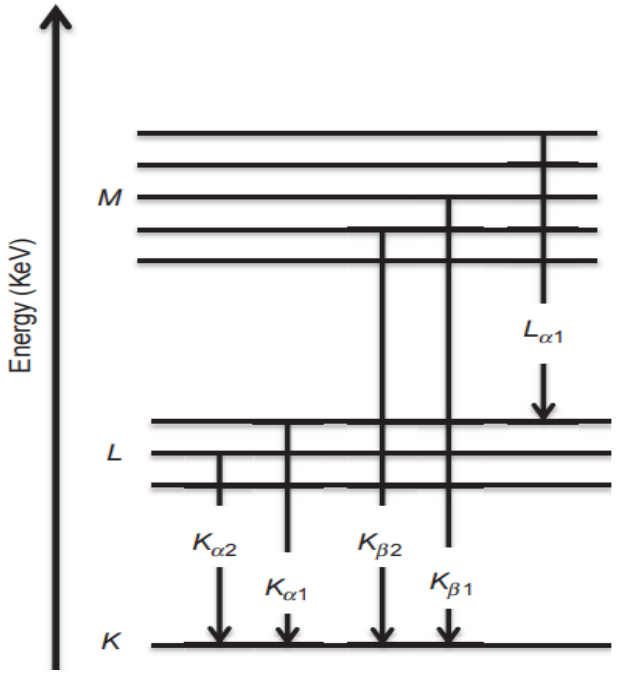

Figure 2.9: Schematic of the atomic energy levels and emission of characteristic X-ray radiation [20].

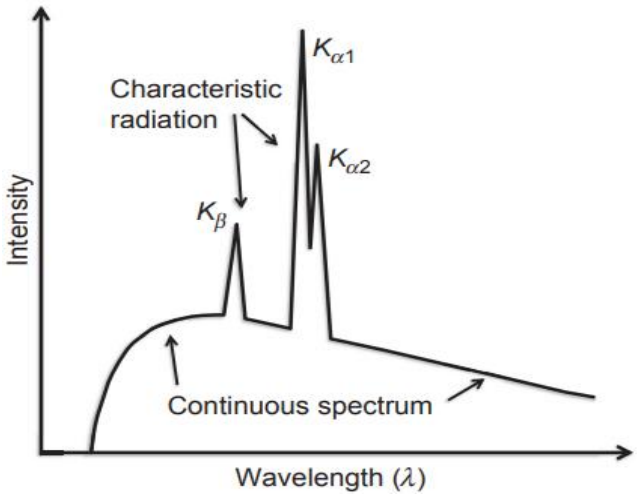

Figure 2.10: Intensity over wavelength distribution of the X-ray radiation produced by a sealed-tube showing the continuous and the characteristic spectrum [20].

The radiation coming out of a sealed tube or a rotating anode is therefore a super imposition of a continuous spectrum and of characteristic radiations as presented schematically

in figure 2.10. In general, XRD methods only use the characteristic radiation with the highest intensity, the K_α radiation, and remove most of the remaining radiation by using appropriate filters or monochromators. The filtering is based on the nonlinear absorption of the filter material regarding the wavelength, leading to absorption edges. According to the filter material, the absorption edge is situated at a different wavelength allowing a strong absorption of the continuous spectrum as well as of the K_β radiation while letting most of the K_α intensity passing through [21]. There are appropriate filter materials for all targets. A list of the common target materials with the wavelength of their characteristic radiations K_α and K_β, together with the minimum excitation potential and the required filters is given in Table2.1 [21].

Table 2.1: List of several common target materials and corresponding wavelength of $K_\alpha$and K_β radiation in nm together with the minimum excitation potential in kV and the appropriate filter material [21].

Target	$K_{\alpha 1}$	$K_{\alpha 2}$	$K_{\alpha\ mean}$	K_β	Excitation potential	Filter
Cr	0.2 2897263	0.2293 6513	0.2291 0346	0.208 48881	5.98	V
Mn	0.2 1018543	0.2105 8223	0.2103 1770	0.191 02164	6.54	Cr
Fe	0.1 9360413	0.1939 9733	0.1937 3520	0.175 66055	7.11	Mn
Co	0.1 7889961	0.1792 8351	0.1790 2758	0.162 08263	7.71	Fe
Ni	0.1 6579301	0.1661 7561	0.1659 2054	0.150 01523	8.33	Co
Cu	0.1 5405929	0.1544 4274	0.1541 8711	0.139 22346	8.98	Ni
Mo	0.0 7093000	0.0713 5900	0.0710 7300	0.063 22880	20.0	Zr

2.2.2.2 Diffraction of X-ray by crystalline materials

The principle of the methods is based on the diffraction of X-rays by periodic atomic planes and the angle or energy-resolved detection of the diffracted signal. The geometrical interpretation of the XRD phenomenon (constructive interferences) has been given by W.L. Bragg [22]. Figure 2.11 gives the details about the geometrical condition for diffraction and the determination of Bragg's law. Bragg's law is given in equation (2.9).

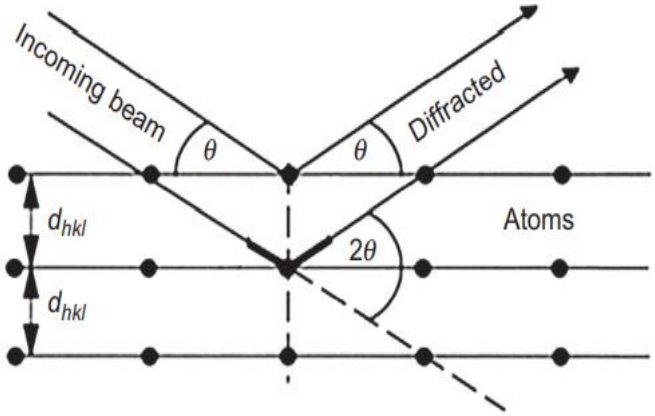

Figure 2.11: Geometrical conditions for diffraction from lattice planes [19].

$$n\lambda = 2d_{hkl}\sin\theta \qquad (2.9)$$

Where

n: is the order of diffraction

λ: the wavelength of the incident beam in nm

d_{hkl}: the lattice spacing in nm

θ: the angle of the diffracted beam.

The total intensity diffracted by a considered unit cell is described by the summation of the intensity scattered from the individual atoms [23]. The diffracted intensities I (hkl) are directly proportional to the square of the crystallographic structure factor F(hkl), which is a complex quantity (equation 2.10) [24].

$$F_{hkl} = \sum_{j=1}^{N} f_j \times \exp(2\pi i(hx_j + ky_j + lz_j)) \qquad (2.10)$$

With f_j the form factor or atomic scattering factor of atom j, hkl the Miller indices of the diffracting planes and xyz the relative atomic positions in the unit cell. The summation j runs over all atoms in one unit cell [24].

2.2.3 Applications

In general, diffraction data are represented as intensity distribution as a function of the angle 2θ (figure 2.12). The information content that can be extracted is

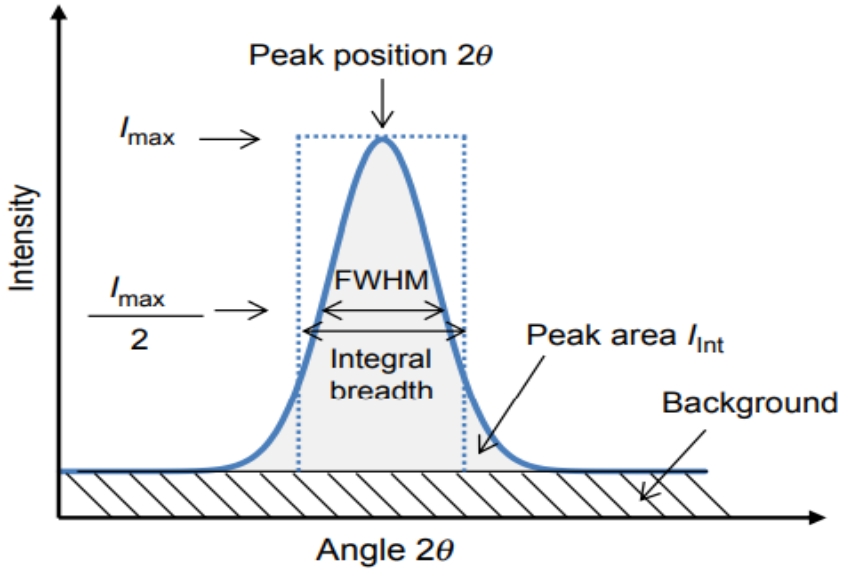

Figure 2.12: Diffraction peak and information content that can be extracted [25].

2.2.3.1 Qualitative phase analysis

This can include phase identification by comparing 2θ values between measured diffraction and pattern diffraction. International Center Diffraction Data (ICDD) or formerly known as (JCPDS Joint Committee on Powder Diffraction Standards) is the organization that maintains the data base of inorganic and organic spectra. The data base is available from the Diffraction equipment manufacturers or from ICDD direct [26].

2.2.3.2 Quantitative phase analysis

By controlling the present phases and their distribution [26].

2.2.3.3 Texture measurements

The method is based on the evaluation of the intensity variation of one or several diffraction peaks of a given phase along a large amount of sample orientation [26].

2.2.3.4 The average crystallite size

(D, in nm) was estimated using Scherrer's equation (2.11) [27].

$$D = 0.9\lambda/\beta \cos\theta \qquad (2.11)$$

where,

λ is the X-ray wavelength for CuK_α (0.154056 nm).

β is the full width in radians at the FWHM of the diffraction line.

θ is the diffraction angle.

2.2.3.5 The average strain

Calculated by the Stokes–Wilson equation (2.12) [28].

$$\varepsilon = \frac{\beta}{4\,tan\theta} \qquad (2.12)$$

2.2.3.6 Lattice constants

The lattice constants a and c values of our sprayed films were estimated from the XRD data using the following equations (2.13 and 2.14) [29]:

$$\frac{1}{d_{hkl}^2} = \frac{4}{3}\left(\frac{h^2+hk+k^2}{a^2}\right) + \frac{l^2}{c^2} \qquad (2.13)$$

$$\sin^2\theta = \frac{\lambda^2}{4}\left[\frac{4}{3}\left(\frac{h^2+hk+k^2}{a^2}\right) + \left(\frac{l}{c}\right)^2\right] \qquad (2.14)$$

In α-Fe_2O_3:

According to the above formulas, for the (110) plane with diffraction peak at 2θ = 35.57°, the lattice constant a was calculated by (equation 2.15) [30]:

$$a_{Fe_2O_3} = \frac{\lambda}{\sin\theta} \qquad (2.15)$$

And for (104) plane with diffraction peak at 2θ = 33.10°, the lattice constant c was calculated by (equation 2.16) [30]:

$$c_{Fe_2O_3} = \sqrt{\frac{12a^2\lambda^2}{3a^2sin^2\theta-\lambda^2}} \qquad (2.16)$$

and unit cell volume[30].

$$v_{Fe_2O_3} = \frac{\sqrt{3}}{2}a^2c \qquad (2.17)$$

In ZnO:

For the (100) plane with diffraction peak at 2θ = 31.36°, the lattice constant a was calculated by [31]:

$$a_{ZnO} = \frac{2}{3}\frac{\lambda}{sin\theta} \qquad (2.18)$$

And for (002) plane with diffraction peak at 2θ = 33.10°, the lattice constant c was calculated by [31]:

$$c_{ZnO} = \frac{\lambda}{sin\theta} \quad (2.19)$$

and unit cell volume[31].

$$v_{ZnO} = a^2 c \quad (2.20)$$

XRD measurements were performed at LMSSEF laboratory using ARL-EQUINOX 100 diffractometer with Cu_{Ka} radiation (λ = 1.5406 Å) to determine the crystallographic and phase structures of the thin films. Illustrated in figure 2.13.

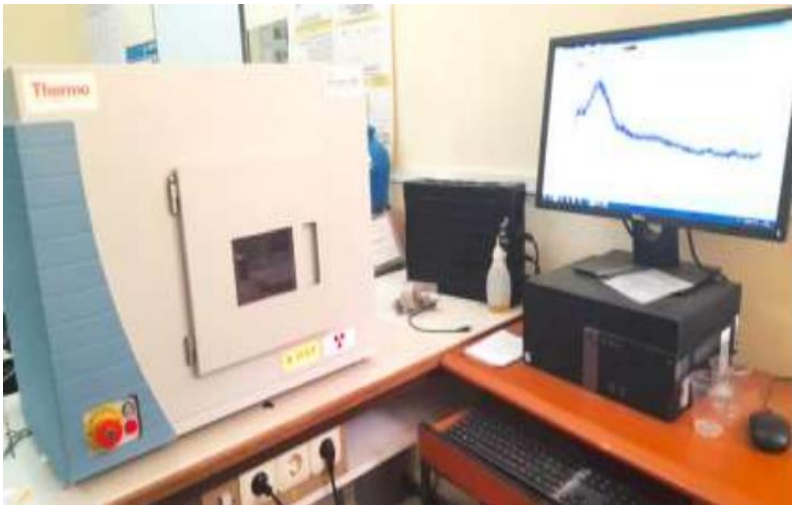

Figure 2.13: Thermo Scientific ARL Equinox 100 X-Ray Diffractometer.

2.3 Scanning electron microscopy (SEM)

2.3.1 Introduction

The scanning electron microscope (SEM) is one of the most versatile instruments available for the examination and analysis of the microstructure morphology and chemical composition characterizations [32]. Since the discovery that electrons can be deflected by the magnetic field in numerous experiments in the 1890s [33], electron microscopy has been developed by replacing the light source with high energy electron beam [33].

2.3.2 Principle

Image formation in the SEM is dependent on the acquisition of signals produced from the electron beam and specimen interactions. These interactions can be divided into two major categories: elastic interactions and inelastic interactions [34]. Elastic scattering results from the

deflection of the incident electron by the specimen atomic nucleus or by outer shell electrons of similar energy. This kind of interaction is characterized by negligible energy loss during the collision and by a wide-angle directional change of the scattered electron. Incident electrons that are elastically scattered through an angle of more than 90˚ are called backscattered electrons (BSE), and yield a useful signal for imaging the sample. Inelastic scattering occurs through a variety of interactions between the incident electrons and the electrons atoms of the sample, and results in the primary beam electron transferring substantial energy to that atom. The amount of energy loss depends on whether the specimen electrons are excited singly or collectively and on the binding energy of the electron to the atom. As a result, the excitation of the specimen electrons during the ionization of specimen atoms leads to the generation of secondary electrons (SE), which are conventionally defined as possessing energies of less than 50 eV and can be used to image or analyze the sample [34, 35]. In addition to those signals that are utilized to form an image, a number of other signals are produced when an electron beam strikes a sample, including the emission of characteristic x-rays, Auger electrons, and cathode luminescence [36]. Figure 2.14 shows the regions from which different signals are detected.

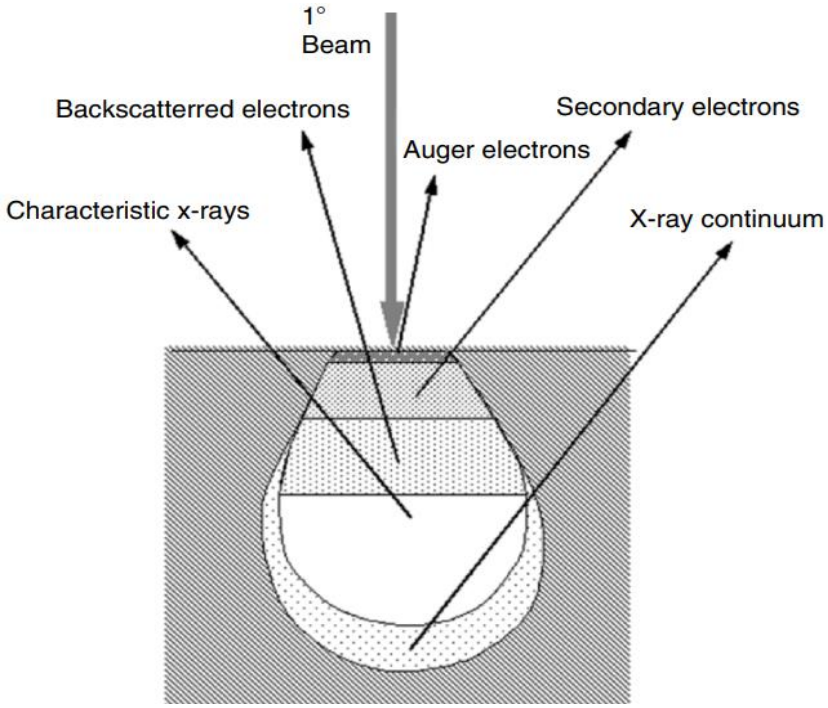

Figure 2.14: Illustration of several signals generated by the electron beam–specimen interaction in the scanning electron microscope and the regions from which the signals can be detected [36].

2.3.3 Instrumentation of SEM

The basic components used in electron optical system are (figure 2.15) [37]:

- A source of electrons, called electron gun,

- Lenses,
- Scanning Coils,
- Detectors to collect signals,
- Sample Stage,
- Display/Data output devices,

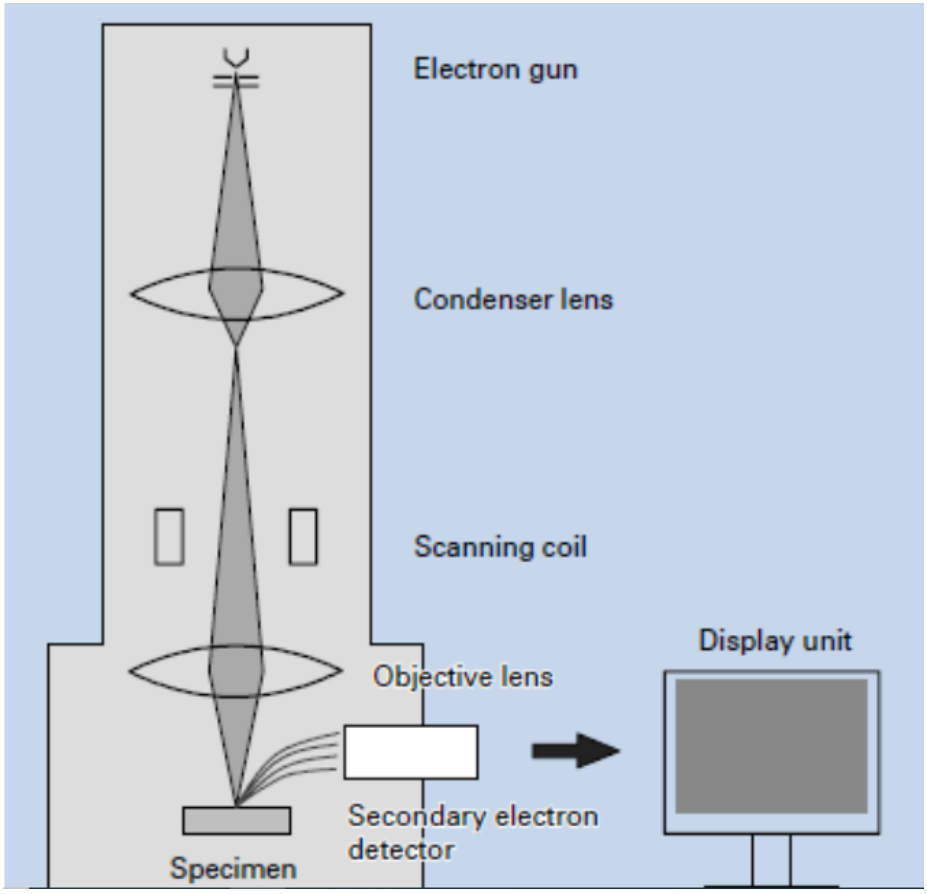

Figure 2.15: Basic construction of SEM [37].

2.3.4 Metal coating

Some specimens are naturally composed of low atomic number elements that naturally emit a low secondary and BSE yield when excited by an electron source. These specimens also act as an insulator and often lead to the charging phenomena. Since the beginning of biological SEM, precious metals were evaporated onto the specimen in order to render the specimen conductive. Sputter coating these metals (gold, silver, gold/palladium, and platinum) in an argon atmosphere reduced bioorganic specimen surface damage [32].

SEM was conducted on the sample using a TESCAN VEGA3 -SEM at the university Oum El bouaghi- ISTA laboratory (figure 2.16) and at LaBoMaP laboratory using JSM-7610F

field emission scanning electron microscopy (figure 2.17). The working distance varied between 5 and 6.5 mm to provide the best image. SEM samples were 1cm^2 area.

Figure 2.16: TESCAN VEGA3 –SEM.

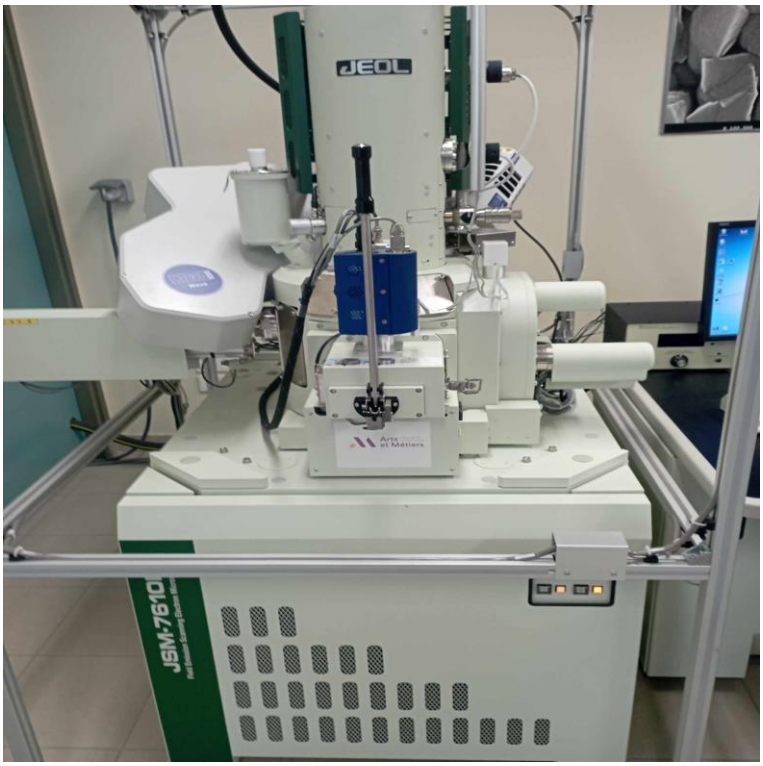

Figure 2.17: JSM-7610F field emission scanning electron microscopy.

2.4 Energy Dispersive X-Ray Spectroscopy

2.4.1 Introduction

EDX spectroscopy is involved in the detection of elemental composition of substance by using scanning electron microscope [38]. EDX is able to detect elements that possess the atomic number of higher than boron and these elements can be detected at concentration of least 0.1%. The application of EDX includes material evaluation and identification, contamination identification, spot detection analysis of regions up to 10 cm in diameter, quality control screening, and others [38].

2.4.2 Principle

Upon collision with the electron beam in typical SEM, the samples interact with the beam and produce characteristic X-rays. Due to the principle that none of the elements have the same X-ray emission spectrum, they can be differentiated and measured for its concentration in the sample [39]. The X-ray is the result of the primary beam of electron interaction with the nucleus of the sample atom. Primary electron beam will excite the electron in the nucleus of an atom, ejecting it from the nucleus and creating an electron hole. An electron from the outer shell (higher energy) of the atom will replace the missing ejected electron and releases the superfluous X-ray. The emitted X-ray consists of X-ray continuum (generated by the deceleration of electron) and characteristic X-ray (generated as a result of higher shell electron filling the electron hole in the nucleus shell) [40].

X-ray continuum is not paramount for the identification of elements in the sample and need to be identified to differentiate them. The intensity of the X-ray continuum is contributed by the factors such as probe current, accelerating voltage supplied, and the atomic number of the sample. On the other hand, the characteristic X-ray will be recorded by the energy dispersive spectrometer for the measurement of the elemental composition in the specimen [41]. The intensity of each radiation depends on the quantity of each element present in the sample. Each atom has individual discrete energy levels and emits fluorescence radiation (Figure 2.18) [42].

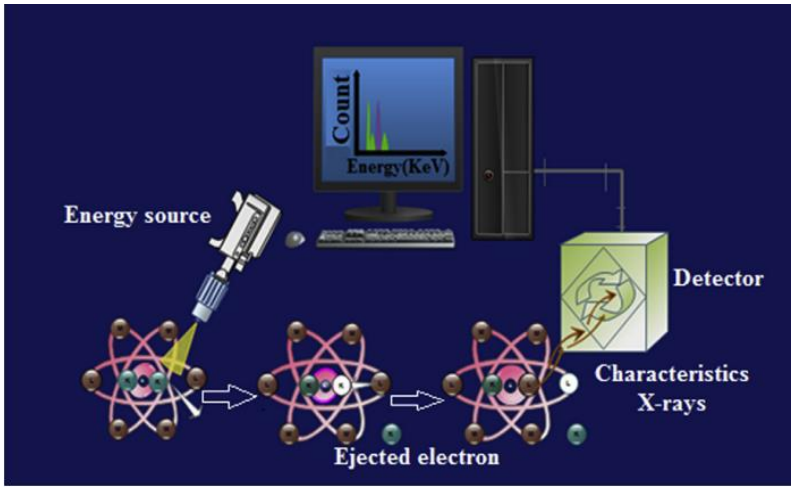

Figure 2.18: Description of energy-dispersive X-ray spectroscopy principle [42].

EDX spectroscopy measurements were performed at LaBoMaP laboratory using JSM-7610F field emission scanning electron microscopy (Figure 2.17).

2.5 Optical profilometry

2.5.1 Introduction

When studying the morphology of uncoated and coated optical surfaces nowadays a variety of sophisticated optical and non-optical characterization methods can be employed [43].

The measurement of 3-D profiles is an important requirement in many engineering fields. The most popular profiling instrument is a mechanical stylus scanner. The main drawback of a stylus instrument is the mechanical contact required for performing the measurement. The mechanical contact with a loaded stylus will cause wear of the stylus itself and damage the measured surface. Also, the spatial resolution of these contact measurements is restricted by the size of the stylus point that degrades during operation due to wear and contamination [44]. Optical profilometry is being used for non-contact surface topography measurement. Several principles such as triangulation and interference provides two dimensional data (line scans) or three dimensional surface images. Roughness parameters can be determined with high accuracy from measured data [45].

2.5.2 Measuring principle

In principle, the method may be used either a conventional light source or a laser. However, all experiments were performed with a He-Ne laser, which also lends itself to direct mathematical analysis [46].

The principle of operation is outlined in figure 2.19. A white light collimated beam is focused at the surface under test by means of longitudinally dispersing optics, so that focus multiplexing is obtained according to the source power spectrum [46]. The back reflected light is partly separated by a beam splitter, and laterally dispersed and focused on a photodiode array. Scanning the array produces a peak signal corresponding to the wavelength in focus at the surface. The knowledge of the foci distribution after calibration allows for surface localization in depth [47].

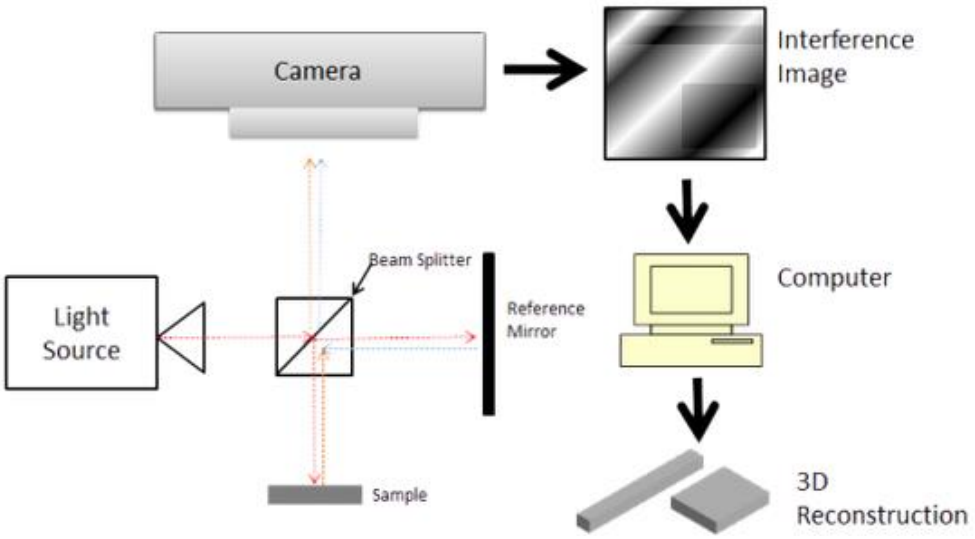

Figure 2.19: Description of optical profilometer principle [47].

2.5.3 Advantages of optical profilometer

The profilometer performance is very important in order to analyze the surface topography properly, in a comparative study on surface roughness and thickness measurements using stylus profiler, optical profilometer, and AFM; Chin. Y. Poon et.al., studied the effects of stylus size, scan size, and sampling interval [48].

The optical profilometer works on the principle of non-contact mode where the light source is used to analyze the materials surface hence true imaging is possible where area measurements can be obtained. The data acquisition in this technique is high-speed compared to that of the contact mode and also it can be obtained for larger areas [45]. This method is a non-destructive technique that does not damage the sample and hence the sample can be used for further analysis. The critical dimensional measurements can be obtained in this technique where the x, y and z coordinates can be measured, which helps obtain the three-dimensional surface data [45].

Optical profilometer measurements were performed at LaBoMaP laboratory using WYKO NT 1100 optical profiling system (Figure 2.20).

Figure 2.20: WYKO NT 1100 optical profiling system.

2.6 Four-Point Resistivity (Conductivity) Measurements

2.6.1 Introduction

Electrical resistivity is a key physical property of all materials. It is often necessary to accurately measure the resistivity of a given material. The electrical resistivity of a material is a number describing how much that material resists the flow of electricity. Resistivity is measured in units of ohm-meters (Ω m). If electricity can flow easily through a material, that material has low resistivity. If electricity has great difficulty flowing through a material, that material has high resistivity [49].

The use of four-point probes is widespread in the semiconductor industry for measurement of surface resistivity [50]. In geophysical applications, probes with four (or more) points are used to measure soil resistivity values in order to reconstruct profiles of soil composition as a function of depth below the surface [50, 51]. Similarly, four-point probes are commonly used to determine the resistivity (or, equivalently, the conductivity) of metals [52].

2.6.2 Four-Point Technique

Figure 2.19 shows the four-point measurement technique on a bar of material. Four wires are attached to the sample bar as shown. A current source forces a constant current through the ends of the sample bar. A separate ammeter measures the amount of current I passing through the bar. A voltmeter simultaneously measures the voltage V produced across the inner part of

the bar. (Alternatively, a voltage source could apply a voltage across the outer contacts, while an ammeter in series with this voltmeter measures the current flowing through the sample bar) [49].

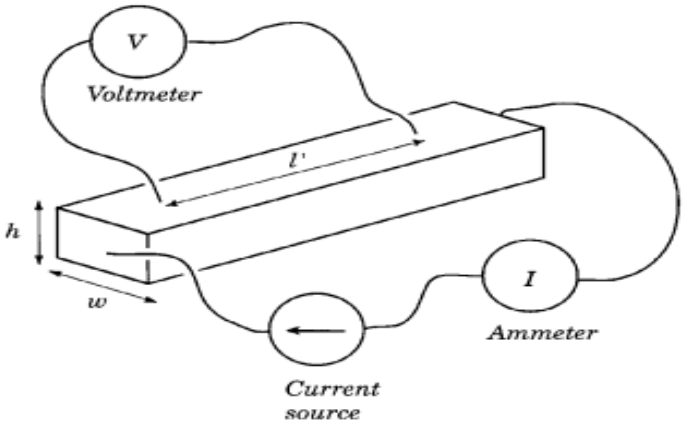

Figure 2.19: A four-point technique for measuring the resistivity of a bar of material [49].

It is often necessary to measure the resistivities of thin films or sheets of various materials. If the material can be made into the form of a rectangle, then the resistivity can be measured just like the bar samples in figure 2.19 [53]:

$$\rho = \frac{\pi.d}{ln2} . \frac{V}{I} \qquad (2.21)$$

where ρ : sample resistivity in **Ω** m

V : Voltage measured by the voltmeter in volts

d: Thickness of the sample measured in meters

I : Current the ammeter measures flowing through the sample in amperes

Therefore, the electrical conductivity (σ) given by the following expression:

$$\sigma = \frac{1}{\rho} \qquad (2.22)$$

2.6.3 Instrumentation for four-point resistivity (conductivity) measurements

The resistivities of thin films of materials are often measured using commercial four-point probes. These probes generally have four equally spaced, collinear metal points that are pressed against the surface of the film. A current is applied between the outer two points, while the voltage is measured across the inner two points. These probes can also be used to measure the resistivity of bulk samples [49].

We used a Four-Point device, Jandel RM3-AR Multi-position 4 Point Wafer Probe (Figure 2.20). The probe consists of four linearly aligned contacts and the distance between the four terminals (a=1 mm). A variable current (I) is applied between the two external terminals and the voltage (V) is measured between the two terminals interns using a KEITHLEY 2400 which measures low voltages.

Figure 2.20: Jandel RM3-AR Multi-position 4 Point Wafer Probe.

References of chapter 2

[1] S. M. Sze , K. Ng, Physics of Semiconductor Devices (2006).

[2] D. L. Wood and J. Tauc, Weak Absorption Tails in Amorphous Semiconductors. Physical Review B 5, 3144 (1972)

[3] E. A. Davis and N. F. Mott, Conduction in non-crystalline systems V. Conductivity, optical absorption, and photoconductivity in amorphous semiconductors. Philosophical. Magazine 22, 0903 (1970).

[4] W. Wendlant, G. Hecht, Reflectance spectroscopy, Wiley Interscience, New York (1966).

[5] R. A. Smith, Semiconductors, 2nd ed., Cambridge University Press: Cambridge (1978).

[6] Z. Chen, F. Thomas Jaramillo, The use of UV-visible spectroscopy to measure the band gap of a semiconductor, Edited by Bruce Brunschwig 2017.

[7] A. Cosimo, C. Haller. UV/Vis spectrophotometry fundamentals and applications. Book 2015. https://www.researchgate.net/publication/321017142.

[8] S. Abdullahi, S. Güner, Y.Koseoglu, I. Musa, Simple Method for the determination of band gap of ananopowdered sample using Kubelka Munk theory. Journal of the Nigerian Association of Mathematical Physics Volume 35, (2016).

[9] J. D. Dow and D. Redfield: Electro absorption in semiconductors: the excitonic absorption edge. Physical review B1 3358 (1970).

[10] R. J. Elliott: Intensity of optical absorption by excitons. Physical Review 1384 (1957).

[11] J. Tauc, A. Menth and D. L. Wood, Optical and Magnetic Investigations of the Localized States in Semiconducting Glasses. Physical Review Letters 749, (1970).

[12] A. P. Finlayson, V. N. Tsaneva, L. Lyons, M. Clark and B. A. Glowacki, Evaluation of BiW-oxides for visible light photocatalysis. Physica Status Solidi 203 327-335 (2006).

[13] K. Boubaker, A physical explanation to the controversial Urbach tailing universality

The European Physical Journal Plus 126 1-4 (2011).

[14] B. Choudhury, B. Borah and A. Choudhury, Extending photocatalytic activity of TiO_2 nanoparticles to visible region of illumination by doping of cerium photochemistry and photobiology, 88 257-264 (2012).

[15] P. Sigmund, Theory of Sputtering. I. Sputtering Yield of Amorphous and Polycrystalline Targets, Physical Review 184 383-416 (1969).

[16] W.C. Roentgen, Uber eine neue Art von Strahlen. In: Sitzungsbericht der Würzburg Physik und Medicin Gesellschaft (1895).

[17] W. Friedrich, P. Knipping, M.V. Laue, Interferenzerscheinungen bei Röntgenstrahlen, Ann Phys 346, 971-988 (1913).

[18] R.E.Dinnebier, S.J.L.Billinge, Powder Diffraction, Theory and Practice, The royal society of chemistry (2008).

[19] L. Spieß, G. Teichert, R. Schwarzer, H. Behnken, C. Genzel, Moderne Röntgenbeugung, second ed. Teubner Verlag, Wiesbaden (2009).

[20] L.H. Schwartz, J.B. Cohen, Diffraction from Materials. Springer Verlag, Berlin (1987).

[21] G. ölzer, M. Fritsch, J. Deutsch, M. Härtwig, E.Förster, $K_{\alpha 1,2}$ and $K_{\beta 1,3}$ X-ray emission lines of the 3d transition metals. Phys Rev A 56, 4554-4568 (1997).

[22] W.L. Bragg, The diffraction of short electromagnetic waves by a crystal, Proc Camb Philos Soc 17, 43-57 (1913).

[23] I.C. Noyan, J.B.Cohen, Residual stress, measurement by diffraction and interpretation. Springer Verlag (1987).

[24] G. Will, Powder Diffraction: The rietveld method and the two stage method. Springer Verlag (2006).

[25] J. Epp, Materials characterization using nondestructive evaluation (NDE) methods.

[26] Chapter 7: Basics of X-ray Diffraction. 10040 Bubb Road Cupertino, CA 95014 U.S.A. Scintag Inc (1999).

[27] B.D. Cullity, Elements of X-ray diffraction, second ed., Addison-Wesley Company, USA (1978).

[28] A.R. Stokes, A.J.C. Wilson, Proc. Phys. Soc. 56-174 (1944).

[29] G.Z. Jia, Y.F. Wang, J.H. Yao, J. Phys. Chem. Solids 73-495 (2012).

[30] A. Mirzaei, K Janghorban, B. Hashemi, S. Hosseini, M. Bonyani, S.Leonardi, A. Bonavita, G. Neri, Synthesis and characterization of mesoporous α-Fe_2O_3 nanoparticles and investigation of electrical properties of fabricated thick films, Processing and Application of Ceramics 10 (2016) 209–217.

[31] G.S.Thool, A.K. Singh, R.S. Singh, A. Gupta, M.A.B.H. Susan, Facile synthesis of flat crystal ZnO thin films by solution growth method: A micro-structural investigation, J. Saudi Chem. Soc.18 (2014)712-721.

[32] W. Zhou, R. P. Apkarian, Z. L. Wang, D. Joy, Fundamentals of scanning electron microscopy (2012)

[33] O. C. Wells, Scanning Electron Microscopy, McGraw-Hill, New York (1974).

[34] S. Wischnitzer, Introduction to Electron Microscopy, Pergamon Press, New York (1962).

[35] M. E. Haine and V. E. Cosslett, The Electron Microscope, Spon, London (1961).

[36] C. W. Oatley, the Scanning Electron Microscope, Cambridge University Press, Cambridge (1972) 7.

[37] J. I. Goldstein and H. Yakowitz, Practical Scanning Electron Microscopy, Plenum Press, New York (1975).

[38] M. Abd Mutalib, M.A. Rahman, M.H.D. Othman, A.F. Ismail, J. Jaafar, Scanning Electron Microscopy (SEM) and Energy-Dispersive X-Ray (EDX) Spectroscopy,Membrane Characterization, Chapter 9 (2017).

[39] Goldstein JI, Newbury DE, Echlin P, et al. Scanning electron microscopy and X-ray microanalysis. (2003).

[40] R. Gauvin, K. Robertson, P. Horny, et al, Materials characterization using high-resolution scanning-electron microscopy and x-ray microanalysis. JOM (2006).

[41] P. Rautala, M. Hietala, H. Sipila, Practical aspects of energy dispersive X-ray emission spectrometry, IAEA, Vienna, 1979, p. 119 (1979).

[42] K .Raghvendra , K. Ajesh, Energy dispersive X-ray spectroscopy technique for nanomaterial, Microscopy Methods in Nanomaterials Characterization, Chapter 12 (2017).

[43] D .Angela, K .Norbert, "Microtopography investigations of optical surfaces and thin films by light scattering, optical profilometry, and atomic force microscopy", SPIE Vol. 1995 Optical Scattering (1993) / 181.

[44] Y. Fainman, E. Lenz, and J. Shamir , Optical profilometer: a new method for high sensitivity and wide dynamic range, APPLIED OPTICS / Vol. 21, No. 17 / 1 (1982).

[45]D.ČAIROVIĆ, ZLÁMAL Martin, P.ŠTĚPÁNEK, T.TRČKA, P. ŠKARVADA and R. MACKŮ, Determination of surface roughness parameters by optical profilometry and sand patch test, Solid State Phenomena ISSN: 1662-9779, Vol. 259.

[46] James C. Wyant , Chris L. Koliopoulos , Bharat Bhushan & Orrin E. George, An Optical Profilometer for surface characterization of magnetic media, A S L E Transactions, 27:2, 101-113, (1984).

[47] G. Molesini, G. Pedrini, P. Poggi and F. Quercioli, Focus-wavelength encoded optical profilometer, Optics communications (1984).

[48] C.Y. Poon, and B.Bhushan, Comparison of surface roughness measurements by stylus profiler, AFM and non-contact optical profiler. Wear, 190(1), (1995).

[49] B. Michael, Electrical conductivity and resistivity (CRC Press LLC. http://www.engnetbase.com (2000).

[50] D. K. Schroder , Semiconductor material and device characterization (New York: Wiley) (1998).

[51] J. M. Reynolds, Introduction to Applied and Environmental Geophysics (Chichester: Wiley) (1997).

[52] D. S. Parasnis, Principles of applied geophysics 5th edn (London: Chapman and Hall) (1997).

[53] N. W. Ashcroft and N. D. Mermin, Solid State Physics, Philadelphia, PA: Saunders College, 1976; C. Kittel, Introduction to Solid State Physics, 7th ed., New York: John Wiley & Sons, (1996).

Chapter 3

Experimental details

3 Experimental details

3.1 Introduction

The experimental process used for the practical realization of the thin films by using spray pyrolysis technique and the photocatalytic test conditions presented in this thesis will be discussed in this chapter.

3.2 Growth process details

All elaboration procedures of the samples are carried out in the laboratory of (LMSSEF: *Laboratoire des matériaux et structure des systèmes électromécaniques et leur fiabilité*), University Larbi Ben M'hidi, Oum El Bouaghi, Algeria.

3.3 Substrate Preparation

- **Substrate selection**

Thin film requires a substrate to support itself. The substrate is very important for the growth of thin films in terms of the lattice and thermal mismatching between it and the film [1].The choice of substrate affects crystalline quality as well as optical and electrical properties of the films [1].

In this work, our thin films were deposited in a microscopy slide glass substrates. The choice of glass as substrate was due to economic reasons, to perform a good optical characterization of our films, and it is adopted because the good thermal expansion that it presents with ZnO (α_{glass}=8.5 10^{-6} K^{-1}, α_{ZnO}=7.2 10^{-6} K^{-1}), which is minimize the constraints between film interface and substrate [1,2] .

- **Substrate Cleaning**

Substrate cleaning in thin film technology is an important step prior to deposition [1]. It is necessary to remove the contaminants that would otherwise affect the properties of the film.

Cleaning involves the removal of contaminants without damage the substrate. While cleaning, the bond between the substrates is broken and contaminants are set free from the substrates. The properties that can be affected by the presence of contaminants include morphology, nucleation electronic properties and the substrate film interface.

The cleaning is done in an ultrasonic bath (figure 3.1) according to the following steps:

- ✓ Rinse the substrates in distilled water for 5 min,
- ✓ Cleaning in ethanol for 5min,
- ✓ Rinse in distilled water for 5 min,
- ✓ Cleaning in acetone for 5min,
- ✓ Rinse in distilled water for 5 min,
- ✓ Substrate drying using Joseph paper.

Substrates should not be touched with hands after this treatment to avoid contamination.

Figure 3.1: Ultrasonic bath photo.

- **Choice of deposition temperature**

The spray pyrolysis technique is among the chemical methods that require high temperatures for the realization of the decomposition of the solutions used arriving on heated substrates and converted into oxides [3].

In order to preserve thin films characteristics, we have chosen a temperature set at 350°C.

3.4 Basic materials

The chemicals used for the synthesis of these thin films are:

- **Iron chloride tetrahydrate ($FeCl_2 \cdot 4H_2O$):** precursor source of Fe_2O_3.
- **Zinc acetate dihydrate ($Zn(CH_3COO)_2 \cdot 2H_2O$) and zinc chloride ($ZnCl_2$) :** precursors source of ZnO nanowires and ZnO nanorods, respectively.
- **Aluminum nitrate nonahydrate ($Al(NO_3)_3 \cdot 9H_2O$):** is source of aluminum (Al) dopants.

Table 3.1: Lists of the products specificities mentioned above.

	chemical formula	**Molar Mass**	**Degree of purity**	**Provider**
Zinc acetate dihydrate	$Zn(CH_3COO)_2.2H_2O$ 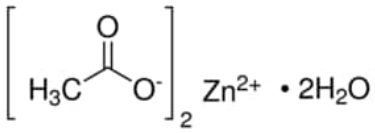	219.51	99.99%	sigma-Aldrich
Zinc chloride	$ZnCl_2$ 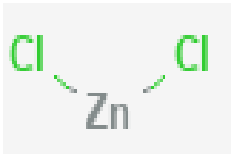	136.315	98%	sigma-Aldrich
Aluminium nitrate nonahydrate	$Al(NO_3)_3 \cdot 9H_2O$ 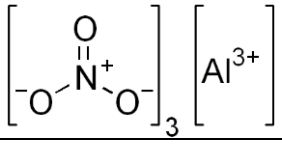	375.13	99.94%	sigma-Aldrich

3.5 Preparation of the solutions

- **Preparation of iron oxide solutions**

The spray solution was prepared from a mixture of 0.1M Iron chloride tetrahydrate ($FeCl_2 \cdot 4H_2O$) as a precursor material dissolved in distilled water to synthesize Fe_2O_3 thin films.

- **Preparation of zinc oxide solutions**

ZnO nanowires and ZnO nanorods thin films were grown by using the chemical spray pyrolysis technique onto a glass substrates using 0.1 M of zinc acetate dihydrate ($Zn(CH_3COO)_2 \cdot 2H_2O$) and zinc chloride ($ZnCl_2$) as precursors dissolved in distilled water, respectively.

- **Preparation of doped zinc oxides solutions**

For depositing of Al doped zinc oxide, we used with amounts calculated so as to obtain Al concentrations of 5% was added to water, in the same conditions used previously.

3.6 Deposited thin films

The resulting solutions were sprayed on the heated glass substrates by an ultrasonic spray pyrolysis system (figure 3.2) which transforms the liquid to a stream of uniform and fine droplets of ~ 40 µm average diameter (given by the manufacturer).

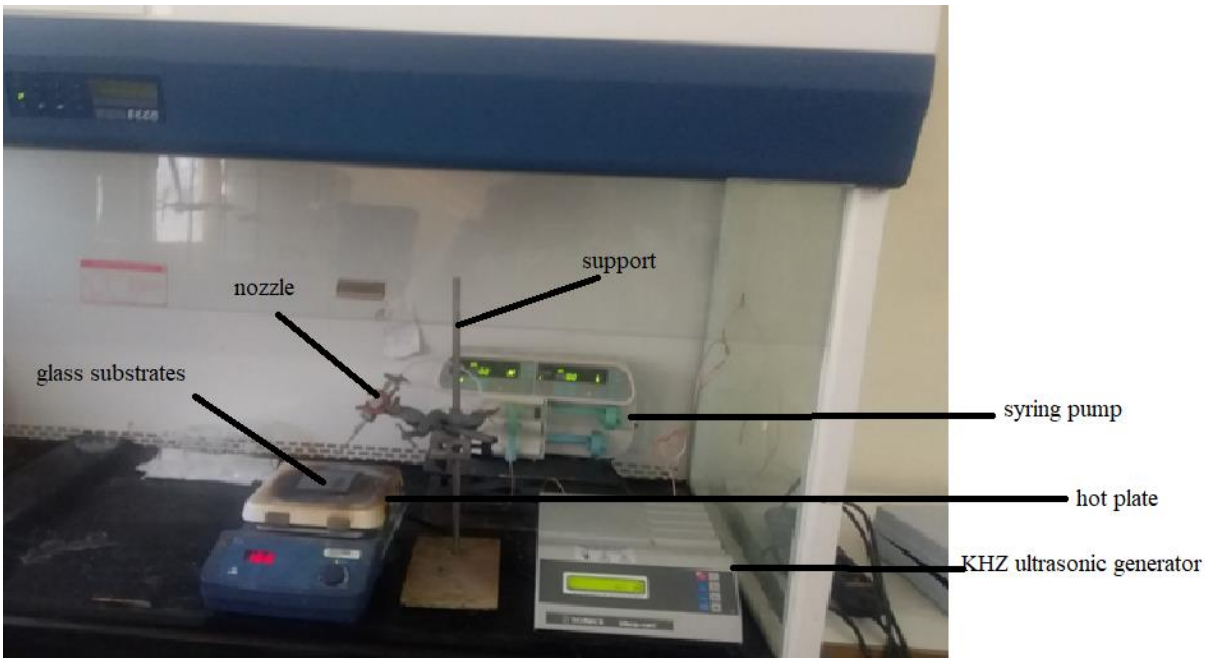

Figure 3.2: Vibra-cell ultrasonic spray pyrolysis system.

The experimental conditions of deposited thin films are fixed during the whole depositions:

- ✓ Substrate demotions : (7.62 x 2.54) cm^2,
- ✓ Nozzle-substrate distance : 3 cm,
- ✓ Volume deposited : 10 ml / sample,
- ✓ Flow:60 ml/h,
- ✓ Substrate temperature : 350 °C,
- ✓ Solution concentration : 0.1 M.

The diagram bellow shown the category of thin films deposited:

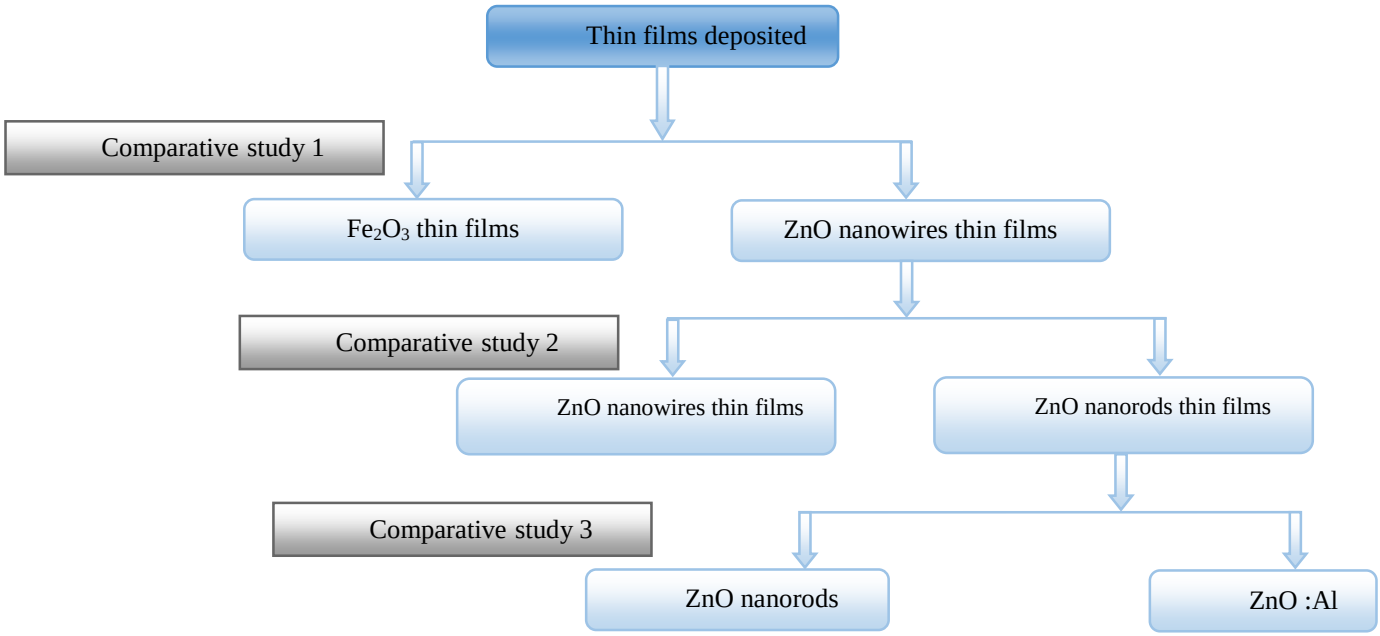

Figure 3.3: Diagram shown the category of thin films deposited.

3.7 External appearance of thin films

Figure 3.4 shows the photos of the different types of thin films, ZnO, Fe_2O_3, and ZnO:Al thin films. The color of these samples is a parameter that can make difference to the naked eye, which changes according to the element nature (Fe_2O_3 or ZnO) and also the doping elements (doped ZnO).This finding may be explained by the fact that doping element color, so it influences the whitish color of undoped ZnO nanorods [4].

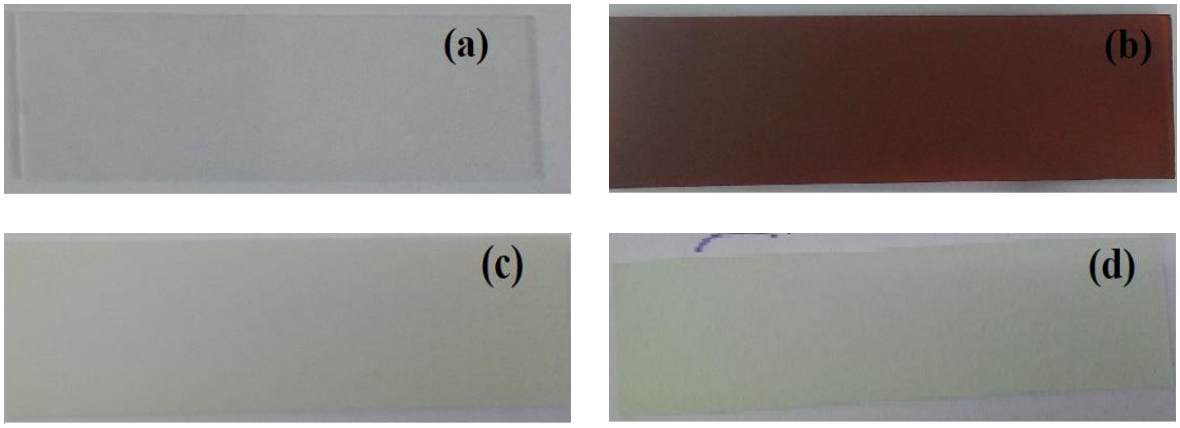

Figure 3.4: Photos of different types of thin films; (a): ZnO nanowires, (b): Fe_2O_3, (c): ZnO nanorods, (d): ZnO:Al.

3.8 Photocatalytic tests

3.8.1 Pollutant

The pollutant used as a model compound during photocatalytic degradation is methyl green dye (MG), and its physico-chemical properties are represented in the following (Table3.2):

Table 3.2: Physico-chemical properties of methyl green dye [5].

Compound (name)	Methyl green
Chemical formula	$C_{27}H_{35}BrClN_3 \cdot ZnCl_2$ 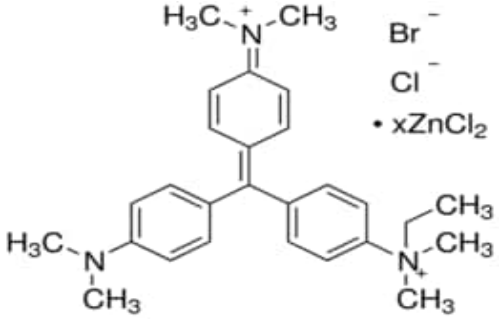
Molar Mass (g/mol)	653.24
Solubility (mg/mL)	In water: 1
Family	Cationic

In addition, the choice of methyl green dye is based on the following reasons [6]:

- ✓ High solubility in water.
- ✓ Low vapor pressure.
- ✓ Simple analysis by UV-Vis spectrophotometry.

3.8.2 Irradiation system

The photo-catalysis experiment is carried out using the setup in figure 3.5.The device is very simple, it consists of a UV lamp Sylvania 20W emitting within 300−370 nm which illuminates the solution to be degraded, which is itself under agitation, ensured by a magneticstirrer, to ensure its homogenization and thus facilitate adsorption and desorption molecules on the surface of the catalyst. The main radiation in the ultraviolet range is at 368 nm, which corresponds to energy in the order of 3.36 eV. This energy is larger than the band gap of Fe_2O_3 (~2.1)[7], ZnO (~3.2 eV)[8] and Al doped ZnO (3- 3.19 eV) [9]. It will therefore allow the activation of the material by generation of electron-hole pairs. The emission of this lamp is characterized by monochromatic radiation.

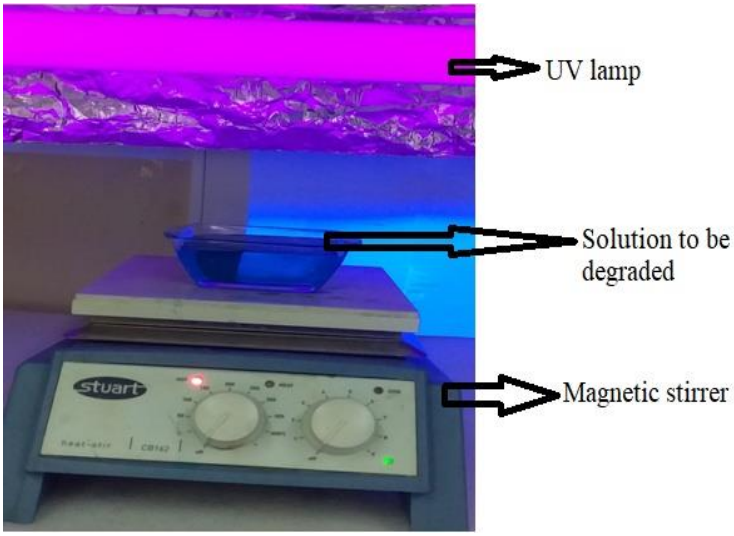

Figure 3.5: Photo-catalysis experimental set-up.

3.8.3 Preparation of methyl green solution

The primary solution was prepared by dissolving 0.02 mg of GM in 110 ml of distilled water. The secondary solutions (V= 110 ml) to be used for the analysis were obtained by successive dilutions to the desired optical density (OD = 0.8at λ= 632 nm) (Figure 3.6).

Figure 3.6: MG solutions.

3.8.4 Photo-catalyst

Thin films used as catalysts are Fe_2O_3, ZnO nanowires, ZnO nanorods, and ZnO:Al nanorods. The different elements were used to determine which one gives better photo-catalysis results.

3.8.5 UV-Visible Spectrophotometer

(JASCO V-630) UV-Visible spectrophotometer, (figure 3.7), was used to measure the optical density of methyl green at 632 nm during photo-degradation. Quartz tank with 10 mm optical path were filled with 3 ml of MG solution.

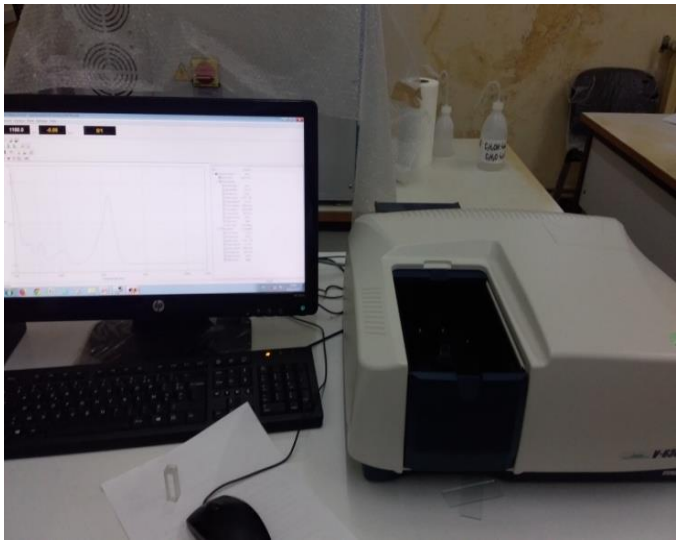

Figure 3.7: (JASCO V-630) UV-Vis spectrophotometer.

The UV-visible spectrum of (MG) aqueous solution with 0.8 optical density(at λ= 632nm) is illustrated in figure 3.8, which shows the existence of 4 characteristic bands of variable intensity, the main one which is located at 632 nm and the other three secondary's are located successively at 254 nm, 312 nm and 420 nm.

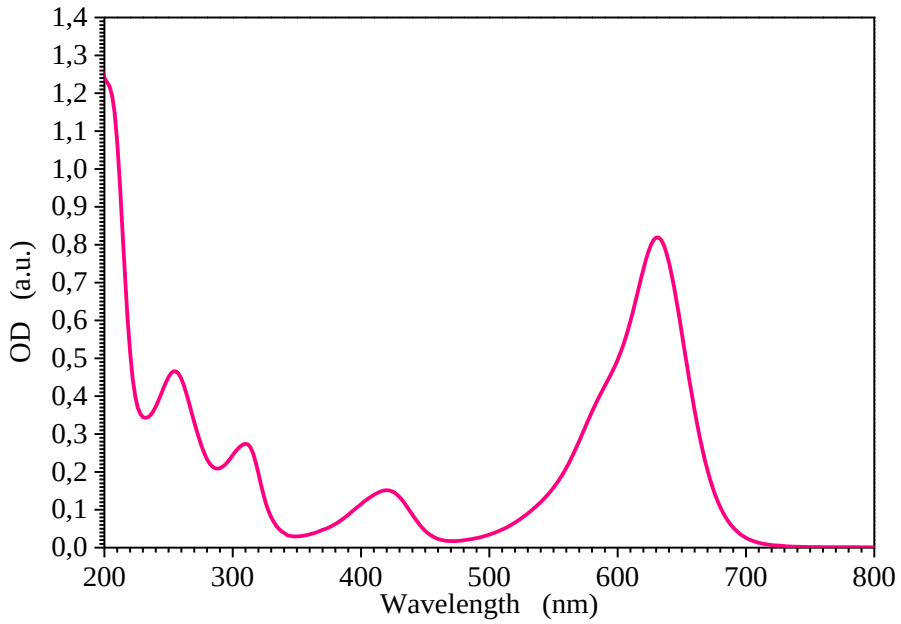

Figure 3.8: UV-visible spectrum of (MG) aqueous solution with 0.8 optical density.

3.8.6 Experimental protocol

In this experiment, we proceeded in three steps:

3.8.6.1 In photolysis

Methyl Green solution with volume of 110 ml was irradiated with a UV lamp for 120 min. Figure 3.9 shows the evolution of the UV-visible spectrum of direct photo-transformation of MG with irradiation time. A decrease in the main band of 632 nm wavelength and change in intensity of the other bands is observed. This evolution of the UV-visible absorption spectrum indicates that the composition of the solution changes during the irradiation and that the light emitted induces the transformation of the MG indicating a photo-transformation of the MG and the appearance of the photoproducts.

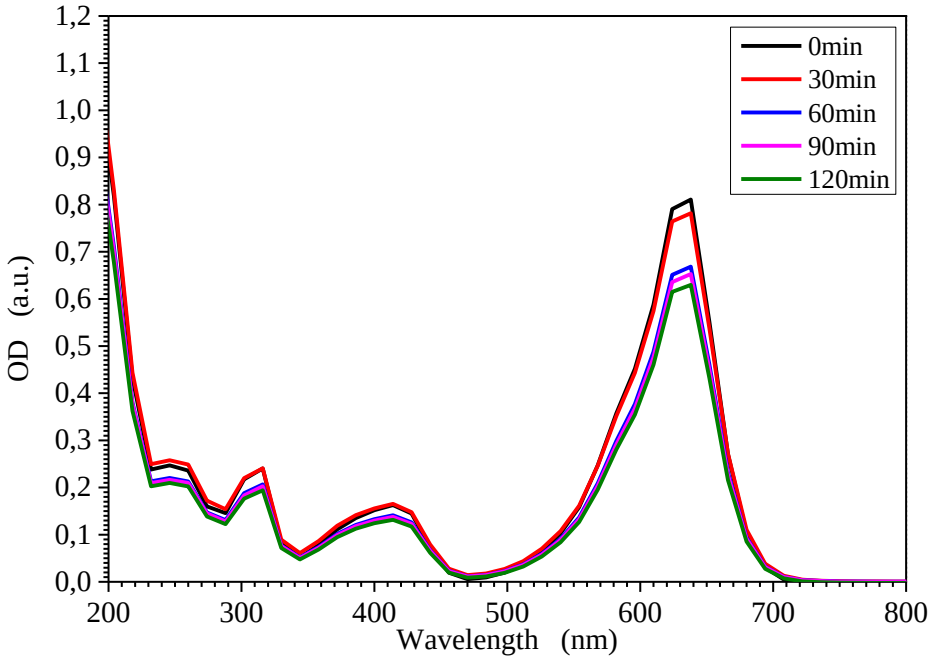

Figure 3.9: Evolution of the UV-visible spectrum of direct photo-transformation of MG with irradiation time

3.8.6.2 In adsorption

We follow the following steps

- Take 110 ml of the methyl green solution then we add thin films layers undoped or doped.
- Stirs the mixture at room temperature in the absence of UV radiation for 60 min.
- Takes samples of the solutions obtained using syringes every 30 min for analysis by UV-Visible spectrophotometer.

3.8.6.3 In photo-catalysis

The following steps have been followed:

- Take 110 ml of the methyl green solution then we add thin films layers undoped or doped.
- Stirs the mixture at room temperature in the absence of UV radiation for 60 min.
- Put this solution under continuous irradiation for 120 min.
- Takes samples of the solutions obtained using syringes every 30 min for analysis by UV-Visible spectrophotometer.

In all cases, all glassware is cleaned by rinsing with distilled water.

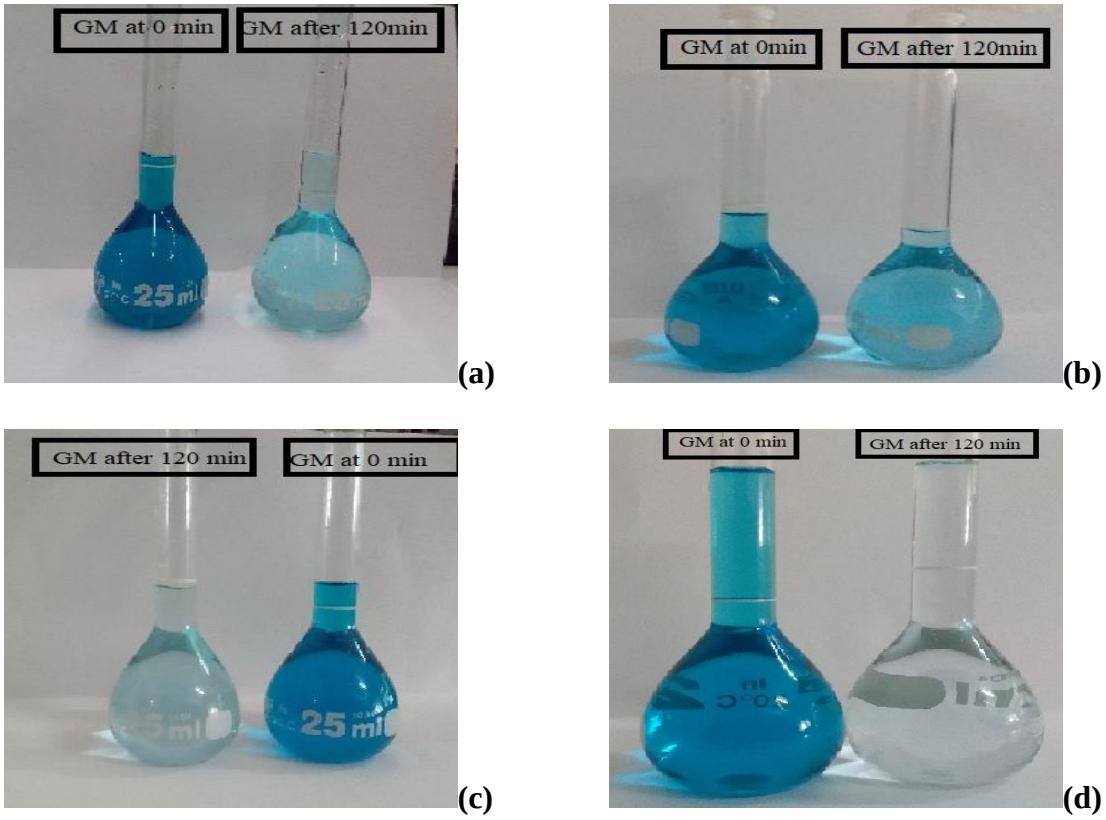

Figure 3.10: Photos of GM solution before and after photocatalysis test for different types of photocatalysts; (a): ZnO nanowires, (b): Fe_2O_3, (c): ZnO nanorods, (d): ZnO:Al.

To make a comparison of the photocatalytic activity of the investigated samples, the degradation efficiency was estimated using equation (3.1) [10]:

$$Degradationefficiency = \frac{(OD)_0 - (OD)}{(OD)_0} \times 100 \qquad (3.1)$$

where $(OD)_0$ is the initial optic density value of the dye solution, (OD) is the optic density value of dye solution at time *t*. Also, the degradation rate constant was obtained from the slope of the linear fitting of $\boldsymbol{ln}[(OD)_0 / OD)]$ vs time, taking into consideration that the photocatalytic degradation of MG is classified as the first-order Langmuir–Hinshelwood kinetics described by equation (3.2) [10]:

$$\boldsymbol{ln}\left(\frac{(OD)_0}{OD}\right) = Kt \qquad (3.2)$$

where *K* is the first-order degradation rate constant.

Conclusion

We have successfully synthesized undoped Fe_2O_3, undoped ZnO with different precursors (zinc acetate dihydrate precursor forming ZnO nanowires thin films and zinc chloride precursor forming ZnO nanorods thin films) and Al doped ZnO thin films on glass substrates using ultrasonic spray pyrolysis method. All the obtained samples have been characterized by deferent techniques for the study of structural, optical, morphological, electrical and photocatalytic properties.

References of chapter 3

[1] L. Herissi, Élaboration et caractérisation de couches minces d'oxydes métalliques destinées à des applications optoélectroniques,Dissertation for the degree of Doctor of Philosophy, Labi ben M'Hidi University (2016).

[2] E. Bacaksiz, M. Parlak, M. Tomakin, A. Özçelik, M. Karakız, M. Altunbaş, The effects of zinc nitrate, zinc acetate and zinc chloride precursors on investigation of structural and optical properties of ZnO thin films, J. Alloy. Compd. 466 (2008) 447–450 (2008).

[3] Van Heerden, J. L., and R. Swanepoel, "XRD analysis of ZnO thin films prepared by spray pyrolysis." Thin Solid Films 299.1-2 (1997): 72-77 (1997).

[4] S. Abbad, K. Guergouri,, S. Gazaout, S. Djebabra, A. Zertal, R. Barille, M. Zaabat, Effect of silver doping on the photocatalytic activity of TiO_2 nanopowderssynthesized by the sol-gel rout, Journal of Environmental Chemical Engineering (2020), https://doi.org/10.1016/j.jece.2020.103718.

[5] P. F. Gordon, P. Gregory, « Organic Chemistry in Color » Springer-Verlag, Berlin, (1983) 5-21.

[6] J. Pierce, Colour in textile effluents - the origins of the problem, Journal of the Society of Dyers & Colourists, 110, pp 131-133 (1994).

[7] A.G.Tamirat, et al., Using hematite for photoelectrochemical water splitting: a review of current progress and challenges. Nanoscale Horizons (2016).

[8] U. Ozgur, Y.I. Alivov, C. Liu, A. Teke, M.A. Reshchikov, S. Dogan, V. Avrutin, Cho S-J, MorkocH, A comprehensive review of ZnO materials and devices. J Appl Phys 98:041301 (2005).

[9] Zhang Y-Hui, Li Y-Liang, Gong F-Long, Xie K-Fei, Liu M, Zhang H-Li, Fang S-Ming, Al doped narcissus-like ZnO for enhanced NO_2 sensing performance: an experimental and DFT investigation, Sensors and Actuators: B. Chemical (2019),
doi: https://doi.org/10.1016/j.snb.2019.12748.

[10] S. Azizi, N. Mesri, T. Sehili, L. Hadjeris, L. Herissi, Degradation of methyl green by a supported photocatalyst: Economic technique for the depollution, Int. J. Chem. Biochem. Sci. 18(2020)73 78 (2020).

Chapter 4

Results and discussion

4 Results and discussion

4.1 Introduction

Good quality thin films can be prepared by controlling their properties which offers the ability to modify the physical properties of the material according to the need of the type of application. The aim of this work is to study how to achieve the best conditions leading to photocatalytic yield enhancement. This chapter is devoted to the presentation and discussion of results obtained from three different comparative studies,

In the first study, titled "Comparative study between ZnO and Fe_2O_3 thin films", we compare the structural, optical, morphological, and electrical properties of the sprayed ZnO (prepared with zinc acetate dihydrate precursor) and Fe_2O_3 thin films in detail. Then the photocatalytic activity properties of these thin films has been evaluated, by studying the degradation of the methyl green (MG), as a polluting model.

In the second study, titled "Comparative study between ZnO nanowires and ZnO nanorods thin films", we compare the structural, optical, morphological, and electrical properties of the sprayed ZnO nanowires and ZnO nanorods thin films prepared with different precursors (zinc acetate dihydrate precursor forming ZnO nanowires thin films and zinc chloride precursor forming ZnO nanorods thin films). Then the photocatalytic activity properties of these thin films has been evaluated, by studying the degradation of the same polluting (MG) mentioned above.

Finally, in the third study, titled "Comparative study between undoped ZnO nanorods and 5% Al doped ZnO nanorods thin films", we compare the structural, optical, morphological, and electrical properties of the sprayed undoped ZnO nanorods and ZnO: Al thin films. Then the photocatalytic activity properties of these thin films has been evaluated, by studying the degradation of the same polluting (MG) mentioned above.

4.2 Comparative study between ZnO and Fe_2O_3 thin films

4.2.1 X-ray diffraction analysis

The structural properties of our samples were determined by X-ray diffraction. Figure 1 represents typical XRD patterns of sprayed ZnO (4.1.a) and Fe_2O_3 (4.1.b) thin films. The as-grown ZnO films are polycrystalline with hexagonal structure (wurtzite type), highly c-axis-oriented. Indexed by all diffracted peaks (JCPDS 036-1451) [1]. The as-grown Fe_2O_3 films are

also polycrystalline in nature with the rhombohedral structure of a hematite Fe_2O_3phase, identifiable with the reference (JCPDS 01-086-2368). No other peaks connected to impurities were observed [2] (Figure 4.1).

The highest peak intensity is most appropriated for calculation of some crystallographic parameters ((101) for ZnO and (104) for Fe_2O_3).

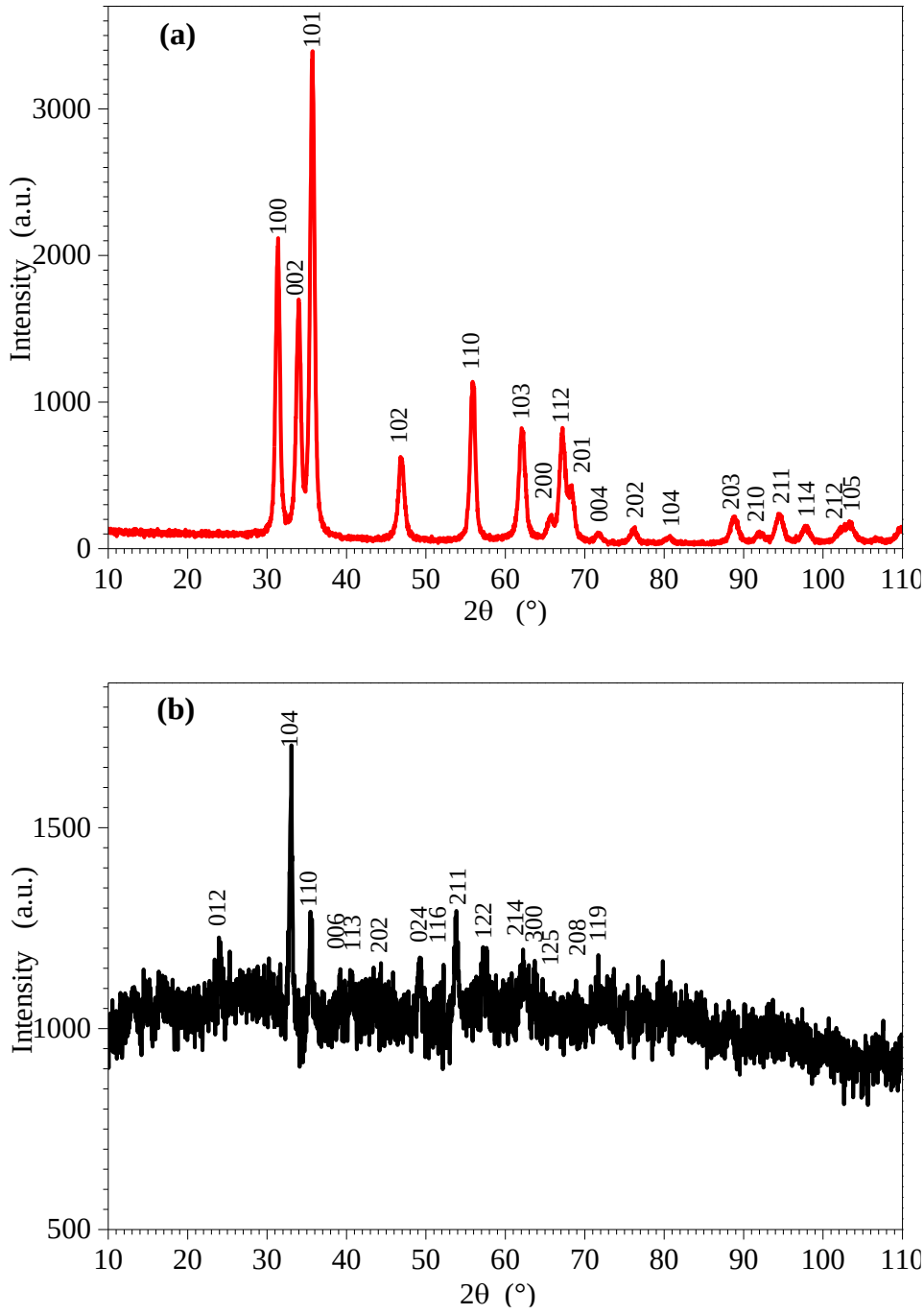

Figure 4.1: XRD patterns of: (a) ZnO (b) Fe_2O_3.

Table 4.1: Some crystallographic parameters determined from ZnO and Fe_2O_3 thin films XRD data.

Sample label	**(hkl)**	**FWHM β (°)**	***D* (nm)**	***ε (%)***
ZnO	(101)	0.354	26	0.46
Fe_2O_3	(104)	0.413	22	0.59

Table 4.2: The lattice parameters of Fe_2O_3 and ZnO thin films.

Sample label	**Lattice parameters (Å)**	
	Calculated	Standard
ZnO	*a*=*b*=3.76 *c*=5.22 v = 74 Å ^{3}	*a*=*b*=3.24 *c*=5.20 v = $a^2c = 55Å^3$
Fe_2O_3	*a*=*b*=5.04 *c*=13.77 v=302.91 Å^3	*a*=*b*=5.035 *c*=13.75 v = $\frac{\sqrt{3}}{2}a^2c = 301.87Å^3$

The average crystallite size of the studied films was found to be 22 nm for $Fe_2O_3$and 26nm for ZnO (Table 4.1). The lattice parameters of ZnO and Fe_2O_3 are in close agreement with the reported standard data [3, 21] (Table 4.2).

4.2.2 UV-Vis spectroscopy analysis

Figure 4.2 represents the transmittance spectra of ZnO and Fe_2O_3. These spectra are characterized by two regions: a region below 370 nm (for zinc oxide) and below 540 nm (for iron oxide) where there is total absorption which is due to the excitation and the migration of the electrons from the valence band to the conduction band and also to oxygen deficiency [4], and a second region, above 380 nm (for zinc oxide) and above 540 nm (for iron oxide), where there is non-zero transmittance. The low transmittance and the absence of interference fringes in the both spectra can be explained by a high surface roughness this explanation is in agreement as we shall see on the one hand with the SEM cross section images morphology results (Figure 4.6) and on the other hand with optical profilometer results (Table 4.4), also the variations with wavelength indicates the presence of many defects which create local states in the gap [5, 6].

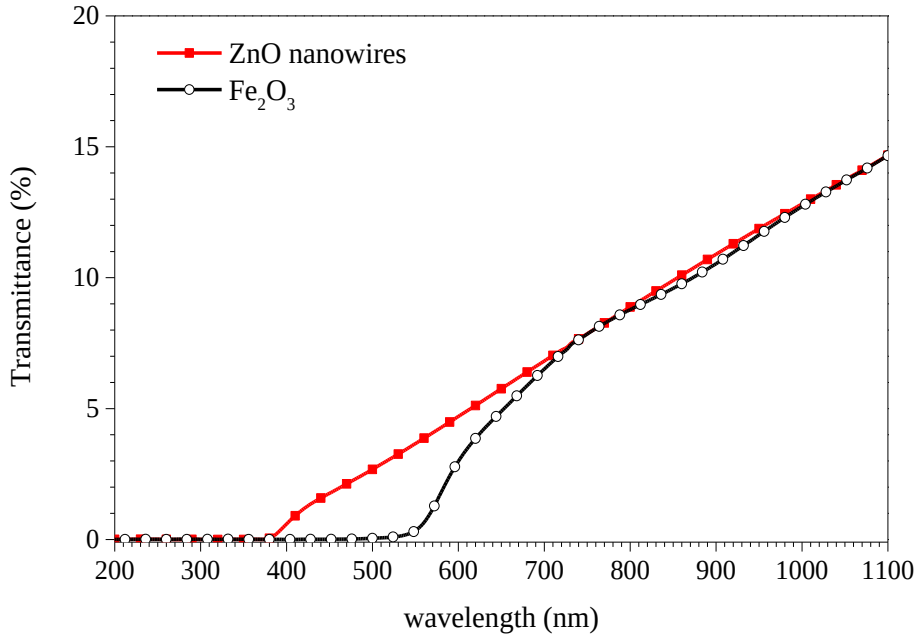

Figure 4.2: Optical transmittance spectra for ZnO and Fe_2O_3 thin films.

As explained in Chapter 2 (paragraph 2.1.5 and paragraph 2.1.6) for the determination of band gap energy and Urbach energy parameter from UV-Vis spectra we deduced the band gap energy values Eg = 3.12 eV for ZnO and E_g = 2.10 eV for Fe_2O_3 (Table 4.3). Also, the low Urbach energy parameter, deduced for Fe_2O_3 (E_{Urb} =167 meV), can be ascribed to less defects compare with ZnO (E_{Urb} =667 meV) (Table 4.3) [5].

Table 4.3: Some optical parameters for ZnO and Fe_2O_3 thin films

Sample Name	***E*g (eV)**	***E*Urb(meV)**
ZnO	3.12	667
Fe_2O_3	2.10	167

4.2.3 Profilometer analysis

Three-dimensional optical profilometer images of (a) ZnO and (b) Fe_2O_3thin films surface morphology are displayed in figure 4.3. All thin films show homogenous grain distribution characterized by columnar growth perpendicular to the substrate. This observation is in agreement with the XRD results (c-axis orientation). Furthermore, the films exhibit different surface topographies, which seem to be dependent on the non-uniform films thickness this observation is in agreement as we shall see with the SEM cross section images morphology results (figure 4.6).

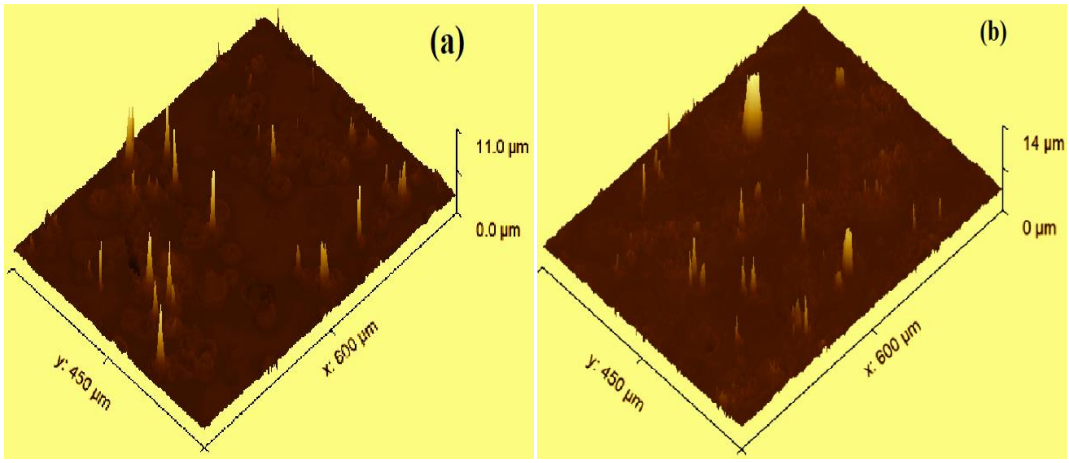

Figure 4.3: Three-dimensional (3D) topography images of (a): ZnO and (b): Fe_2O_3 thin films.

The root mean square roughness (RMS) and Mean roughness (Ra) were deduced from these images and their values are shown in Table 4.4.

Table 4.4: Morphological parameters for ZnO and Fe_2O_3 thin films

Sample Name	RMS roughness (nm)	Mean roughness Ra (nm)
ZnO	451.6	206.5
Fe_2O_3	349.6	186.6

The low root mean square roughness (RMS) and Mean roughness (Ra) were deduced for Fe_2O_3 can be ascribed to less defects compare with ZnO this observation is in agreement with thelow Urbach energy parameter deduced in paragraph (4.2.2) [5].

4.2.4 Electron spectroscopy (SEM) analysis

The morphological arrangement of sprayed Fe_2O_3 and ZnO thin films was examined using scanning electron microscopy.

Figures 4.4 (a-b-c-d-f) show SEM images of Fe_2O_3 top surface at different magnifications including (x3000, x50000, x80000. andx100000) with 30kV. Fe_2O_3 layer showed a classic thin film surface morphology where grains are distributed uniformly throughout the surface (a-b) [7]. SEM images (c-d-e-f) show that Fe_2O_3 grains are of spherical shape with nanometer size. Moreover, agglomerates formation was observed in (c-d-e) SEM images which could explain the surface roughness of Fe_2O_3 thin films.

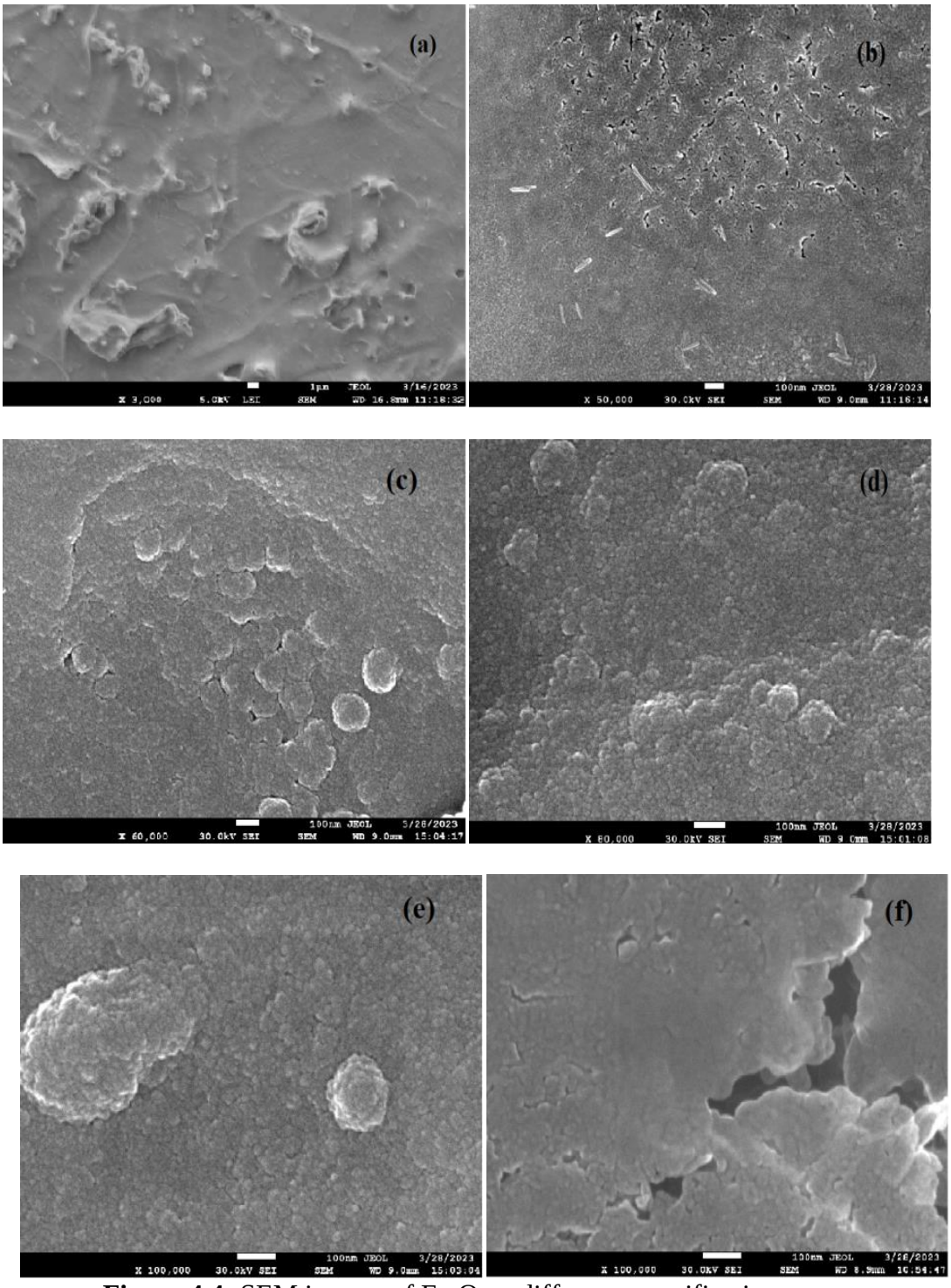

Figure 4.4: SEM images of Fe_2O_3 at different magnifications.

The SEM micrographs of zinc oxide thin films at three different magnifications (x 250, x 1500 and x 3000) with 5 kV are shown in figure 4.5 (a-c).We observe nanowires grown onto the substrate surface with a low density, irregular in size and which are horizontaly aligned to the substrate.

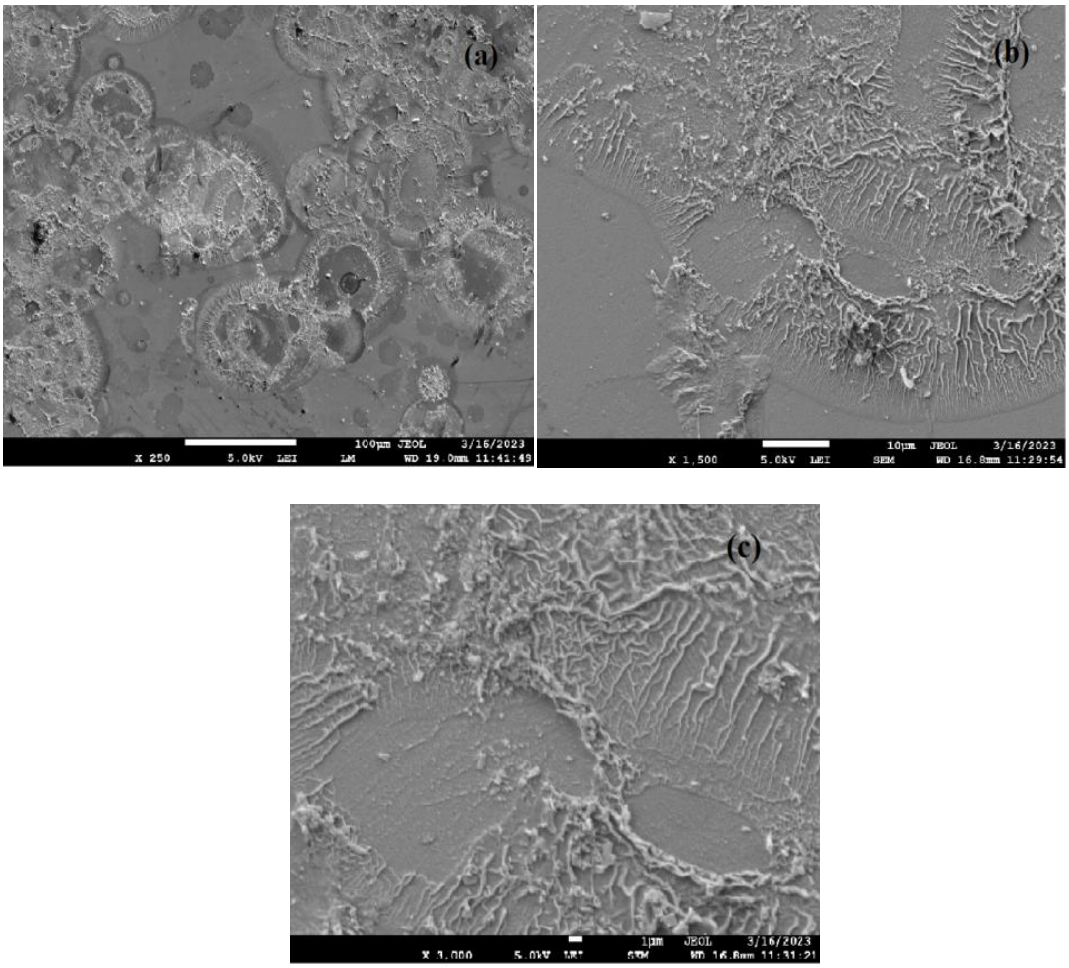

Figure 4.5: SEM images of ZnO nanowires at different magnifications.

SEM images of Fe_2O_3 thin films cross section morphology deposited on glass substrates is shown in figure 4.6 (a-c), demonstrating the roughness surface. It also shows that the thickness of the Fe_2O_3 film is heterogeneously led to the non-uniformity for theFe_2O_3thin films deposited by spray pyrolysis technique [8]. According to Perednis: defects, such as non-uniformity of the film, cracks and pores, are among the most frequent problems presented in the films deposited by spray pyrolysis [9].

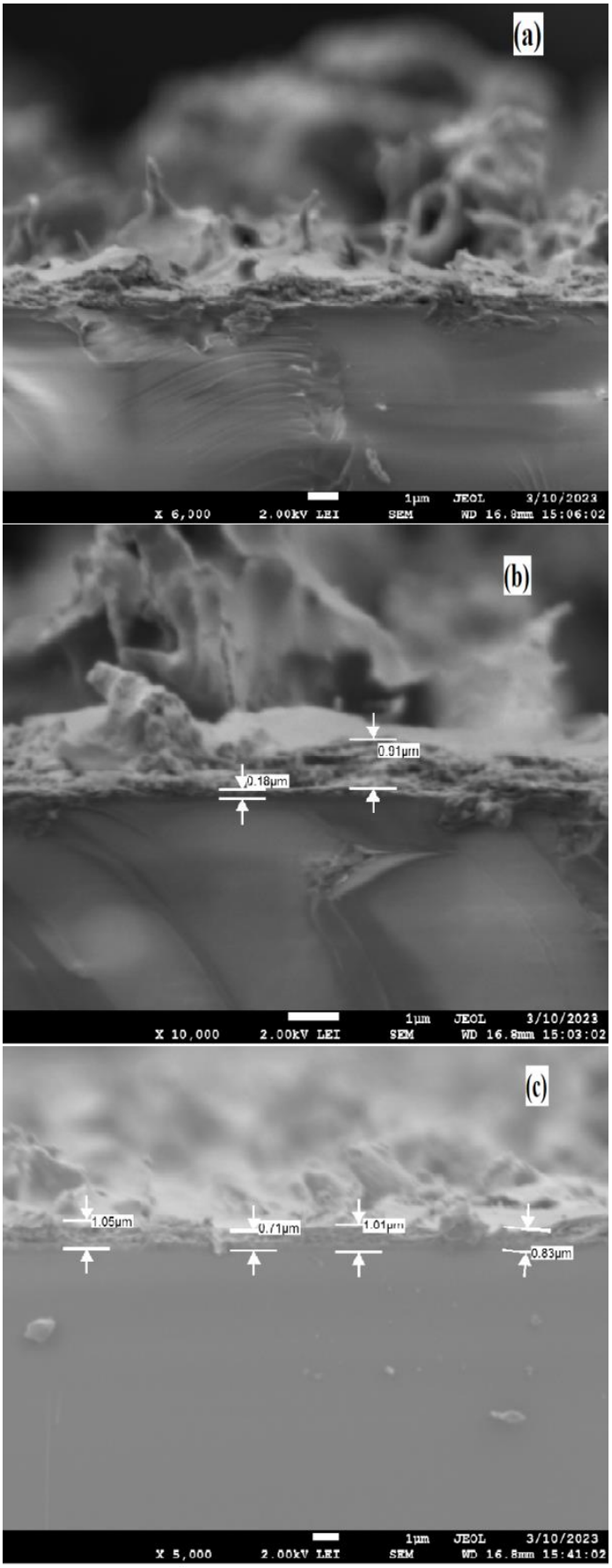

Figure 4.6: Fe_2O_3 thin films SEM images cross section morphology.

4.2.5 Energy dispersive spectroscopy (EDS) analysis

In order to know the elemental composition of the ZnO and Fe_2O_3 thin films, EDS analysis was carried out as shown in the figure 4.7 (4.7.a: ZnO; 4.7.b: Fe_2O_3) where the atomic percentage (%) of the elements such as Zn and O for ZnO thin films, Fe and O for Fe_2O_3 thin films are given, this results is clearly indicating the formation of the two oxides.

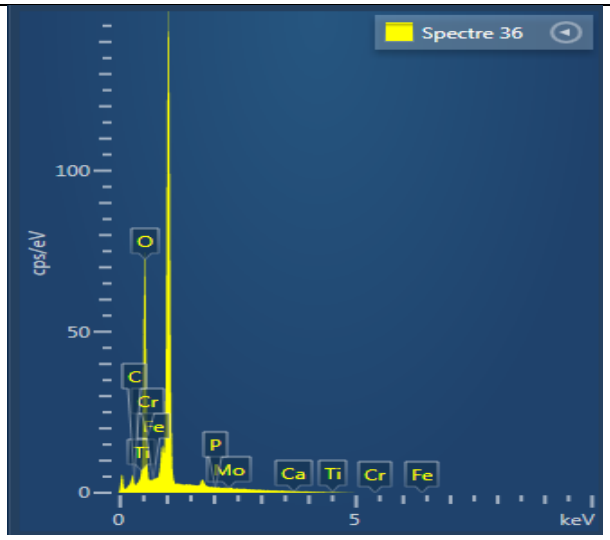

(a)

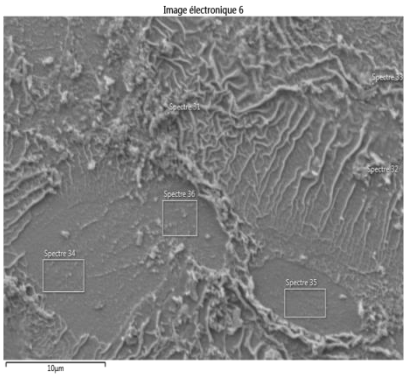

Elements	Atoms %
Zn	49.49
O	50.51

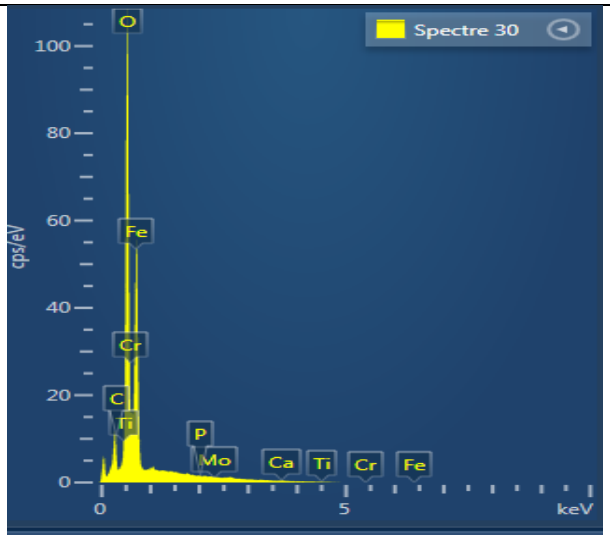

(b)

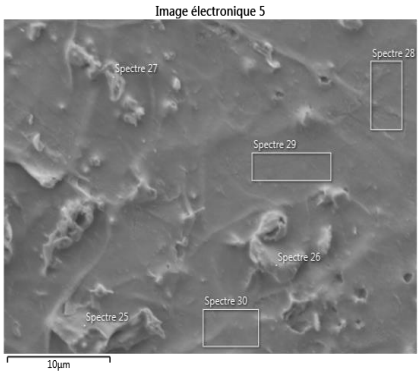

Elements	Atoms %
Fe	44.53
O	55.47

Figure 4.7: EDS spectrum, Selected Areas and atomic percentage table for (a) ZnO (b) Fe_2O_3.

4.2.6 Electrical properties

ZnO and Fe_2O_3thin films I-V are measured using commercial four-point probe at room temperature is shown in figure 4.8, (4.8.a: ZnO ; 4.8.b:Fe_2O_3).The electrical conductivity values were deduced from this measuring are shown in (Table 4.5).We can see from table 4.5 there is a difference in the electrical conductivity for ZnO and Fe_2O_3thin films, where it is lower for Fe_2O_3thin films this may be mainly due to the difference of charge carriers where it is an insufficient number of charge carriers for Fe_2O_3thin films [10]. On the other hand iron oxide thin films are known as poor electrical conductive materials [10, 11]. According to Ingler Fe_2O_3 has high resistivity, shows slow surface kinetics, and possesses low electron mobility and high electron-hole combination due to low carrier diffusion properties [12].

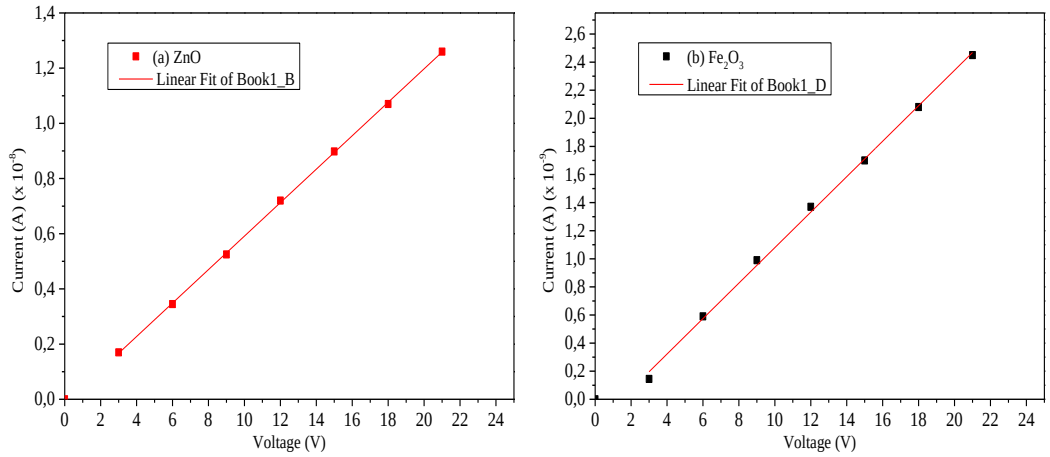

Figure 4.8: I-V measurement for ZnO and Fe2O3 thin films.

Table 4.5: Summary of the electrical conductivity of ZnO and Fe_2O_3 thin films

Sample Name	Electrical conductivity δ $(\Omega.cm)^{-1}$
ZnO	4.39×10^{-6}
Fe_2O_3	9.18×10^{-7}

4.2.7 Photocatalytic activity

A comparative study between the different dye removal catalyst (ZnO and Fe_2O_3Thin films) is shown in figure 4.9. It is observed that the degradation rate of MG increases with UV irradiation time and the photocatalytic activity is improved in the presence of ZnO photocatalyst which shows 55 % degradation of MG after ≈ 2 h of UV exposure, whereas, Fe_2O_3 sample shows only 39 % degradation after 2 h.

According to Ohtani et al. The degradation phenomenon is explained as follows: the high activity of photocatalyst should satisfy a requirement: large surface area for absorbing dye

[12].The explanation that we propose to this phenomenon will be based on the highest of the active surface. Indeed, as shown on the SEM images, that is more important for ZnO.

The higher band gap energy reduce photo-excited electron-hole recombination rate these electron-hole generate ($OH^{\cdot}$) radical (The hydroxyl radicals have strong oxidizing power responsible for the degradation of pollutants) [13].On the other hand, hematite is also a preferred photocatalytic material, because its absorption is in the visible region. While compared with ZnO or TiO_2, hematite shows lower photocatalytic efficiency because of corrosion property or the formation of short-lived metal-to-ligand or ligand-to-metal charge transfer states [14].

The results given above for the degradation of MG, which is the most important for ZnO is confirmed with the calculation of the reaction rate constant k (Figure 4.10), which is the largest for ZnO in this study.

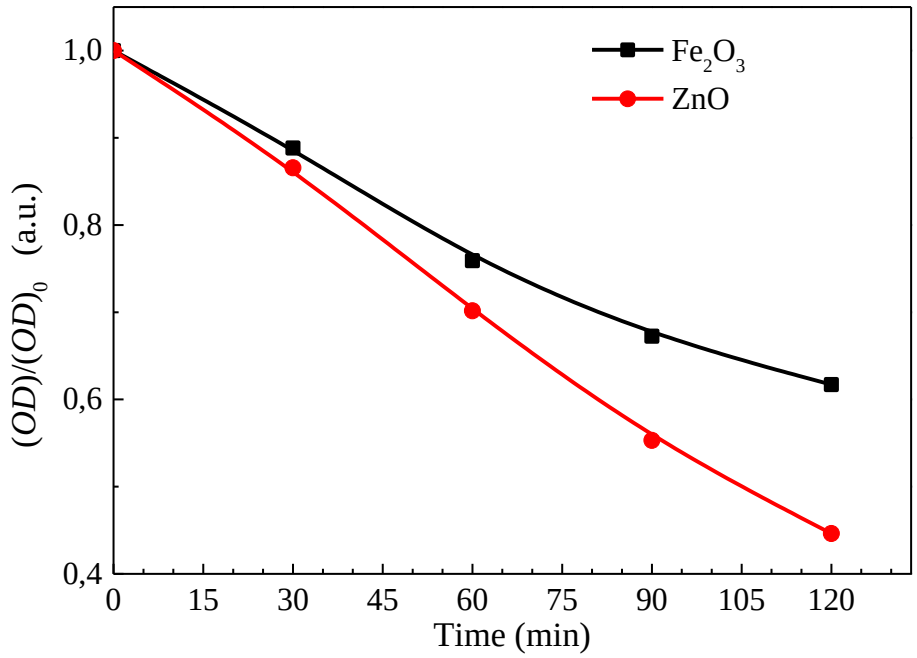

Figure 4.9: *Photodegradation kinetic of MG dye by ZnO and Fe_2O_3 catalyst.*

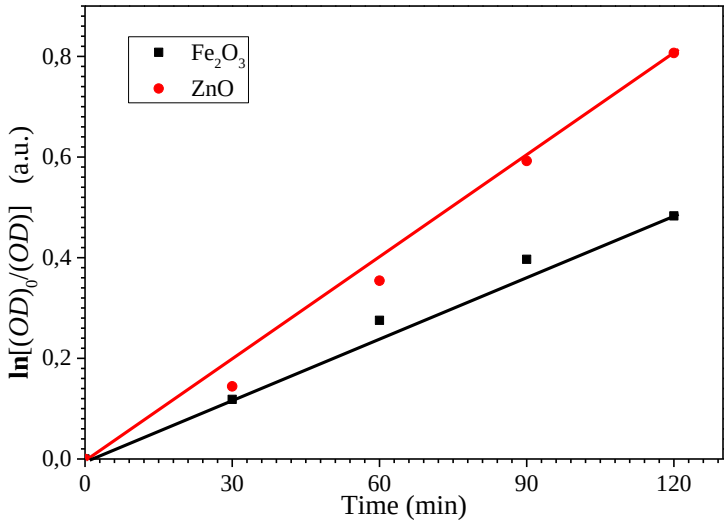

Figure 4.10: Pseudo-first order kinetics of MG photocatalytic degradation by ZnO and Fe_2O_3 catalysts.

Table 4.6: Summary of the kinetic parameters of MG photocatalytic degradation by ZnO and Fe_2O_3 catalyst.

Sample Name	Degradation efficiency (%)	Constant rate k (min^{-1})	Half-life time $T_{1/2}$(min)
ZnO nanowires	55	0.007	99
Fe_2O_3	39	0.004	169

4.2.8 Conclusion

From the results of our first comparative study between ZnO and Fe_2O_3 thin films, it appears that an enhancement of 16 % in the photocatalytic activity of ZnO thin films was achieved compared to Fe_2O_3 thin films.The results indicated that ZnO thin films composed of nanowires are more suitable than Fe_2O_3 thin films as photocatalyst for organic dye photodegradation (MG).

4.3 Comparative study between ZnO nanowires and ZnO nanorods thin films

4.3.1 X-ray diffraction analysis

Typical XRD patterns of sprayed ZnO with different precursors (zinc acetate dihydrate precursor forming ZnO nanowires thin films and zinc chloride precursor forming ZnO nanorods thin films) are presented in figure 4.11: ZnO nanowires (4.11.a) and ZnO nanorods (4.11.b).We can see that the as-grown ZnO thin films are highly c-axis-oriented corresponding to hexagonal (wurtzite) structures indexed by all diffracted peaks (JCPDS NO. 036-1451). No other peaks

connected to impurities were observed, which confirms that the synthesized materials are ZnO thin films. Similar XRD results are also checked in the reported literature for ZnO [15, 16]. The three prominent XRD diffraction peaks in (figure 4.11.a) are (100), (002), and (101), and in (figure 4.11.b) are (002) (102) and (103).

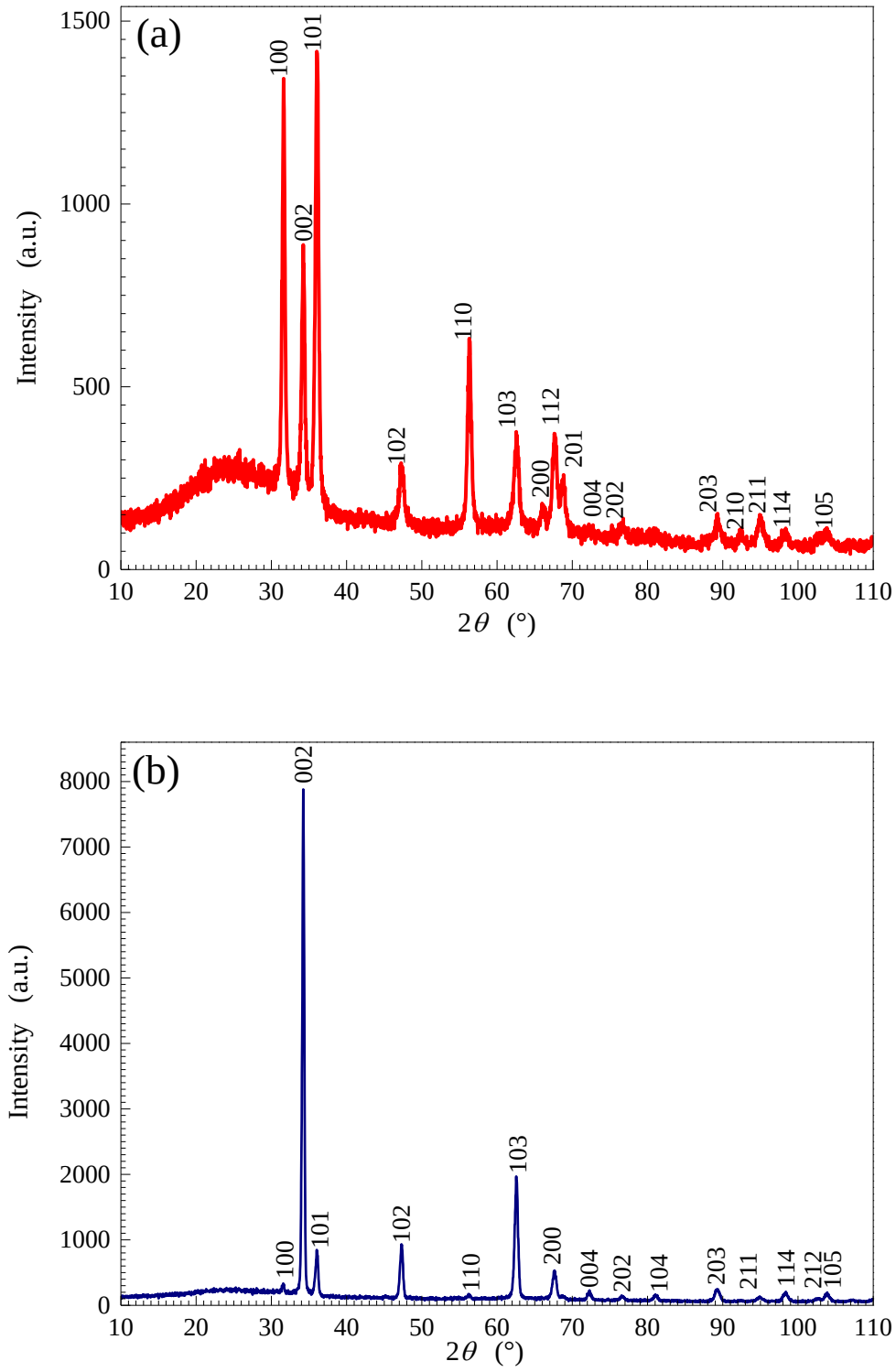

Figure 4.11: XRD patterns of ZnO nanostructures thin films: (a) ZnO nanowires, (b) ZnO nanorods.

Table 4.7: Some crystallographic parameters determined from ZnO nanowires and ZnO nanorods thin films XRD data.

Sample label	**(hkl)**	**FWHM β (°)**	***D* (nm)**	***ε (%)***
ZnO nanorods	(002)	0.265	36	0.360
ZnO nanowires	(101)	0.383	24	0.498

Table 4.8: The lattice parameters of ZnO nanorods and ZnO nanowires thin films.

Sample label	**Lattice parameters (Å)**	
	Calculated	Standard
ZnO nanorods	a=b=3.48 c=4.96 v = 60 Å^3	a=b=3.24 c=5.20 v = a^2c = 55Å^3
ZnO nanowires	a=b=3.76 c=5.22 v=74 Å^3	

The crystallite size of the studied films was found to be 36 nm for ZnO nanorods and 24 nm for ZnO nanowires (Table 4.7). The values found in Table 4.7 show that the stress is tensile in both nanostructures. It is apparent that the nanowires have the biggest unit cell volume as compared to the nanorods and the standard (table 4.8). It is a consequence of higher microstrain in nanowires.

4.3.2 UV-Vis spectrophotometry analysis

Using the same conditions anddifferent precursors (zinc acetate dihydrate precursor forming ZnO nanowires thin films and zinc chloride precursor forming ZnO nanorods thin films), all the obtained thin films were well adherent to the glass substrates and presented the powdery aspect for ZnO nanorods and transparent for ZnO nanowires (figure 3.4in chapter3). Figure 4.12 shows the optical transmittance spectra of ZnO thin films in the wavelength range from 200 to 1100 nm. We found that the ZnO thin films deposited from zinc chloride (nanorods) have a low transmission of about 30 % and an absence of interference fringes, it can be explained by the surface roughnessthis explanation is in agreement as we shall see in optical profilometer results (figure 4.13) and the presence of more defects [5, 6]. While the ZnO thin films deposited from zinc acetate (nanowires) have higher transmission of about 60 %, in the visible range. The region of strong absorbance was observed below 380 nm. In this region, the decrease of the transmittance is due to the excitation and the migration of the electrons from

the valence band to the conduction band and also to oxygen deficiency [4], this observation is well agreement with the EDS resultsas we shall see in figure (4.16)

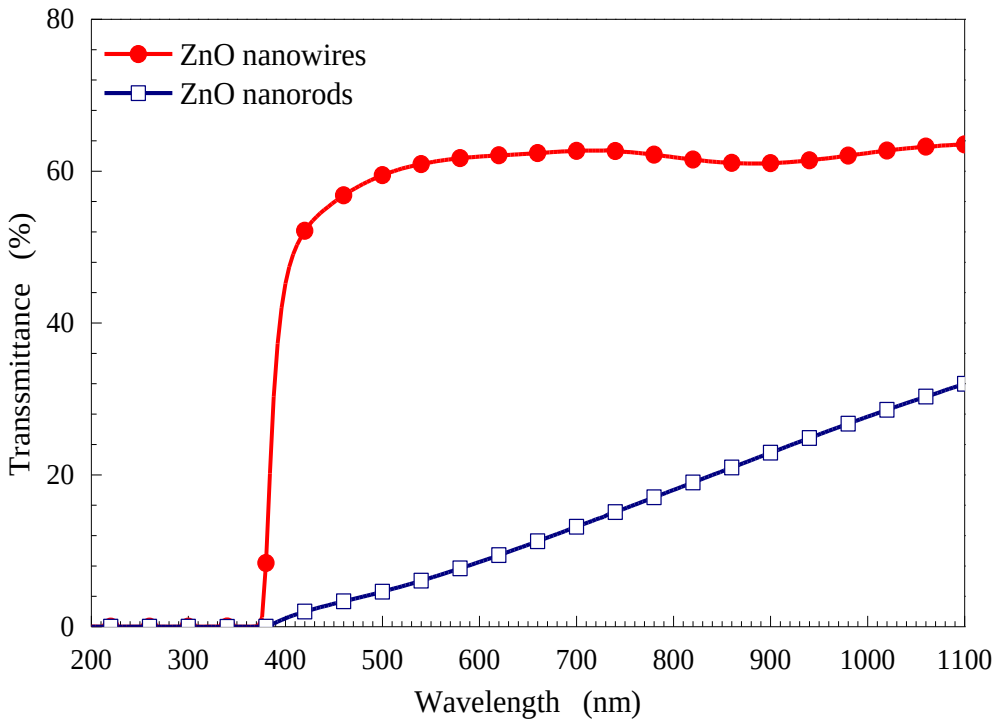

Figure 4.12: Optical transmittance spectra for ZnO thin films.

Also as explained in Chapter 2 (paragraph 2.1.5 and paragraph 2.1.6) for the determination of band gap energy and Urbach energy parameter from UV-vis spectra we deduced the band gap energy values Eg = 3.22 eV for ZnO nanorods and E_g = 3.23 eV for ZnO nanowires (Table 4.9). These values are somewhat smaller than the bulk value for ZnO equal to 3.3 eV [17].Also, the low Urbach energy parameter, deduced for ZnO nanowires samples (E_{Urb} =71 meV), can be ascribed to less defects compare with ZnO nanorods (E_{Urb} =157 meV) (Table 4.9) [5].

Table 4.9: Some optical parameters for ZnO nanorods and nanowires thin films.

Sample Name	E_g (eV)	E_{Urb}(meV)	Thickness (nm)	Refractive index
ZnO nanorods	3.22	157	304.82	2.04
ZnO nanowires	3.23	71	131.80	2

4.3.3 Optical profilometer analysis

Three-dimensional optical profilometer images of (a) ZnO nanowires and (b) ZnO nanorods ZnO thin films surface morphology are displayed in figure 4.13.All thin films show homogenous grain distribution characterized by columnar growth perpendicular to the substrate. This observation is in agreement with the XRD results (c-axis orientation)(paragraph 4.3.1). Furthermore, the films exhibit different surface topographies, which seem to be dependent on the non-uniform films thickness.

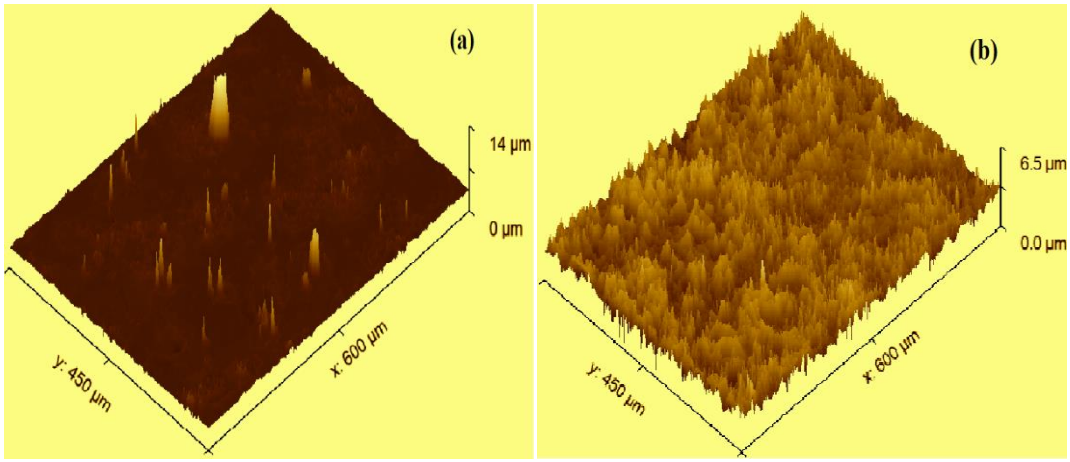

Figure 4.13: Three-dimensional (3D) topography images of (a): ZnO nanowires and (b): ZnO nanorods thin films.

The root mean square roughness (RMS) and Mean roughness (Ra) were deduced from these images and their values are shown in table 4.10.

Table 4.10: Morphological parameters for ZnO nanowires and ZnO nanorods thin films.

Sample Name	RMS roughness (nm)	Mean roughness Ra (nm)
ZnO nanowires	451.6	206.5
ZnO nanorods	486.3	383.6

The low root mean square roughness (RMS) and Mean roughness (Ra) were deduced for ZnO nanowires thin films can be ascribed to less defects compare with ZnO nanorods thin films this observation is in agreement with thelow Urbach energy parameter deduced in paragraph (4.3.2) [5].

4.3.4 Electron spectroscopy (SEM) analysis

The surface morphology of ZnO nanostructures synthesized by spray pyrolysis method with different precussors was characterized by scanning electron microscopy(SEM) and

illustrated in figure 4.14 and figure 4.15 which show SEM images of ZnO nanorods and nanowires, respectevely, at different magnificationsincluding (x3000, x5000, x10000, x20000, x 50000) with 30kV. We observe in figure 4.14 (a-e) hexagonal nanorods, obtained with zinc chloride precursor, grown onto the whole substrate surface with a high density and which are vertically aligned to the substrate.

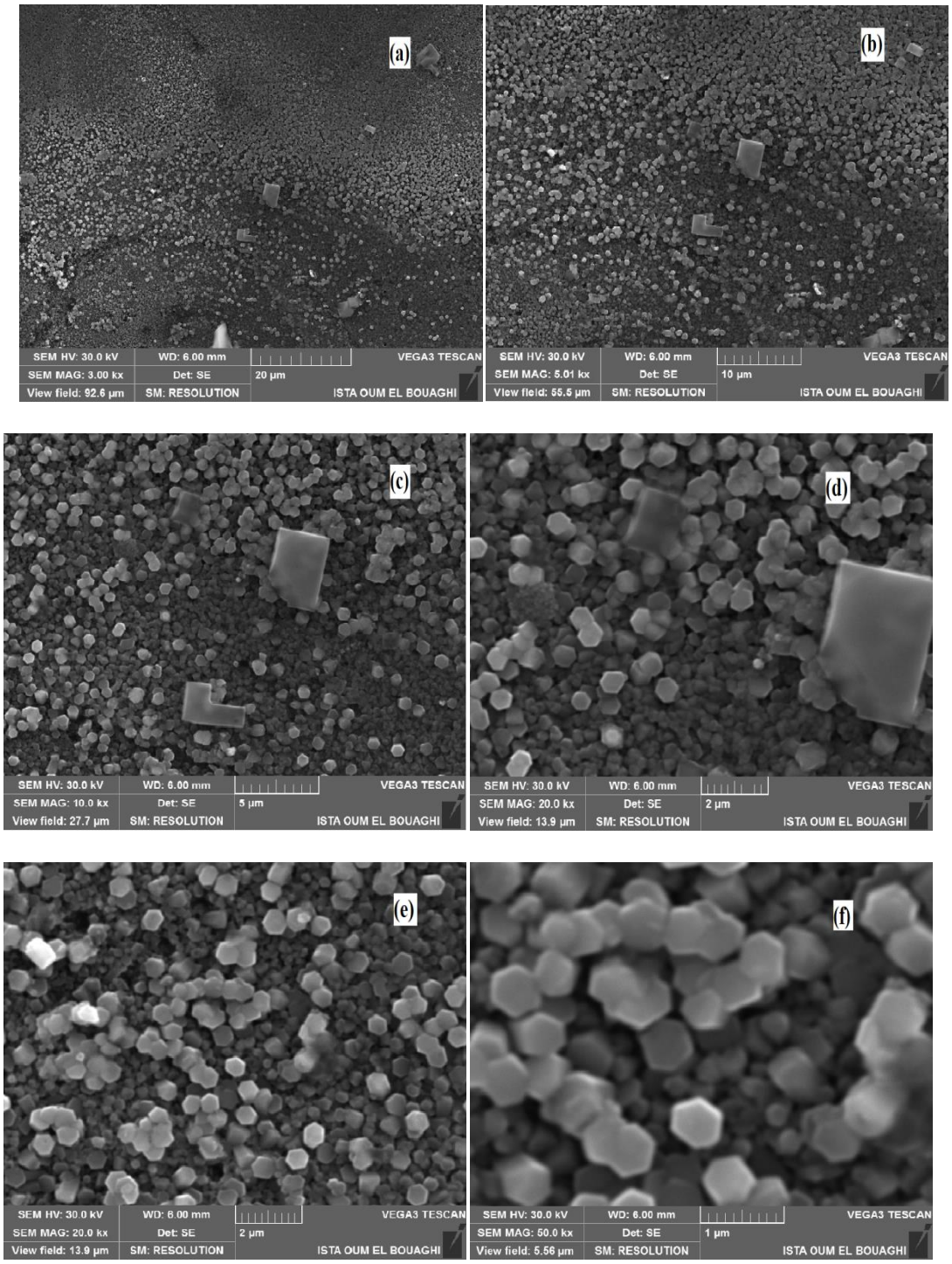

Figure 4.14: SEM images of ZnO nanorods at different magnifications.

The well-defined and perfect hexagonal faceted morphologies of the as-grown ZnO nanorods indicate that the synthesized products have the wurtzite hexagonal phase with a preferential orientation (figure 4.14.d). As displayed, a high density of ZnO nanorods was formed on the full surface substrate as illustrated in figure 4.14.a.

Figure 4.15 (A-G) shows SEM images, with different magnifications, of ZnO nanowires grown, using zinc acetate dihydrate precursor, on the surface of the glass substrate. The ZnO nanowires are with a low density, irregular in size and are horizontally aligned to the substrate.

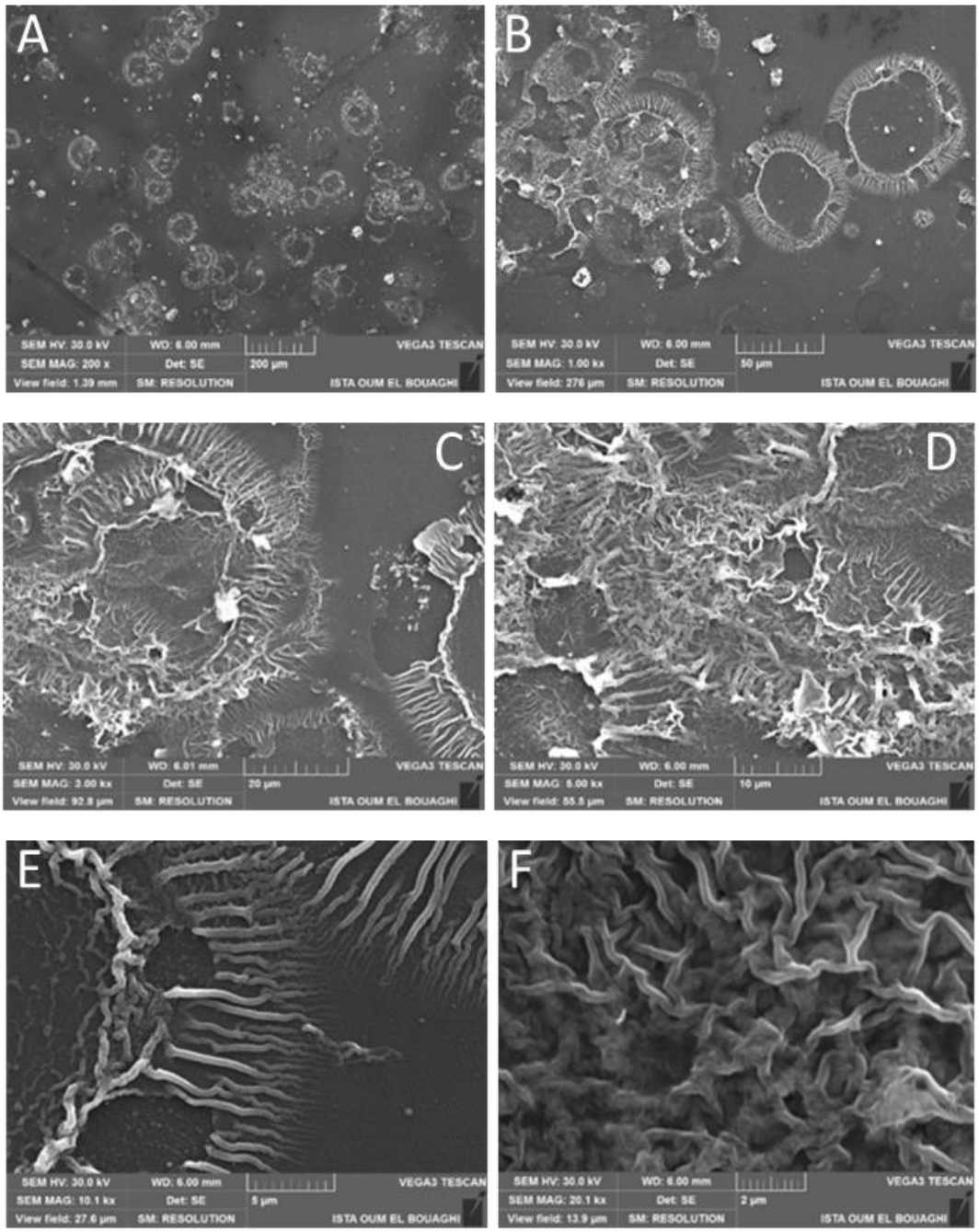

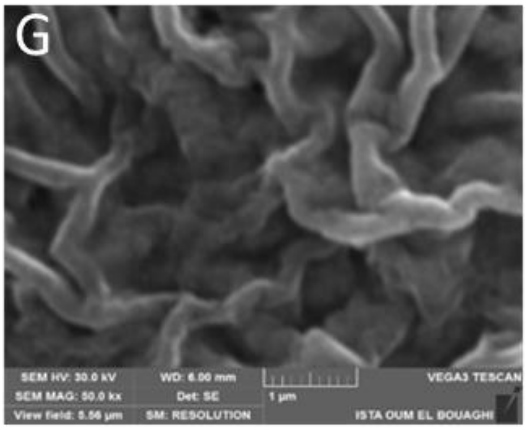

Figure 4.15: SEM images of ZnO nanowires at different magnifications

4.3.5 Energy dispersive spectroscopy (EDS) analysis

The EDS analyses of ZnO nanowires and ZnO nanorods are given in figure 4.16 with the summary of quantitative information from these analyses (4.16.a: ZnO nanowires; 4.16.b: ZnO nanorods). EDS spectra clearly confirm the existence of Zn and O elements these results indicated the successful synthesis of ZnO with deferent nanostructures. We observed the abundances of Zn (54.15 %) element in ZnO nanorods sample; this observation is in agreement with UV-Vis results (figure 4.12) (the oxygen deficiency (45.85 %) could be used to explain the low transmittance of ZnO nanorods thin films).

(a)

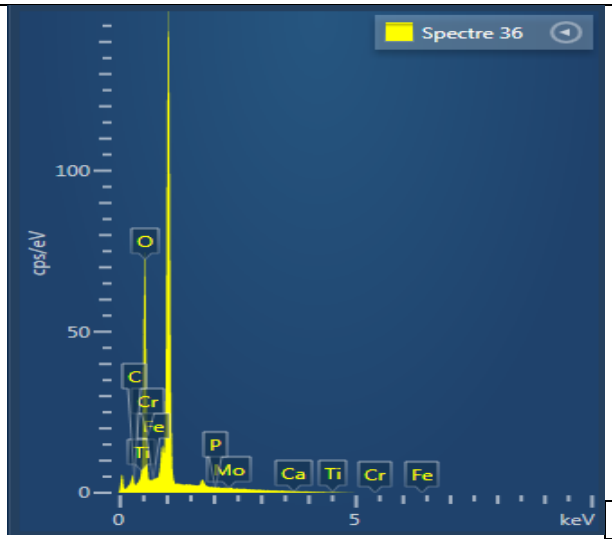

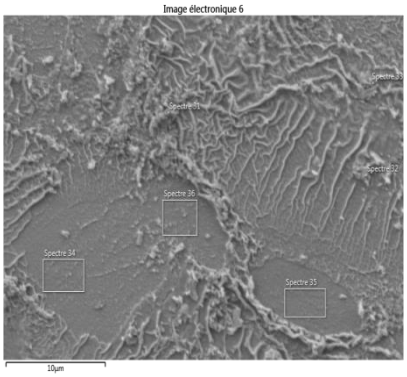

Elements	Atoms %
Zn	49.49
O	50.51

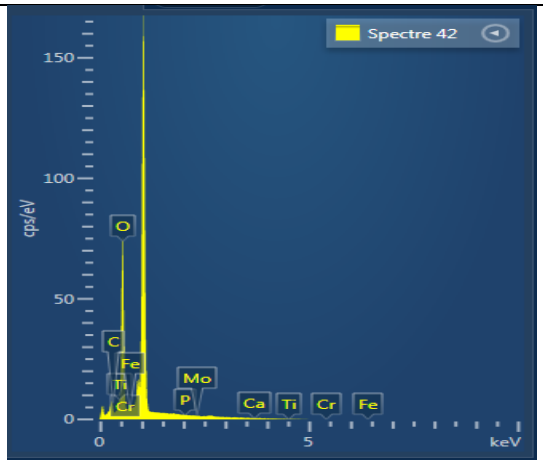

(b)

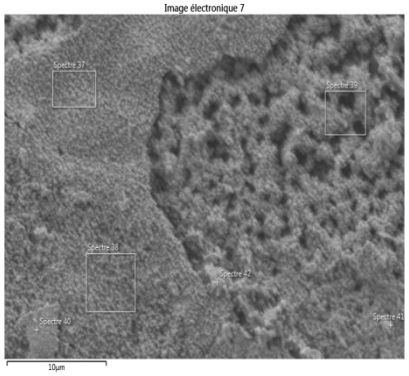

Elements	Atoms %
Zn	54.15
O	45.85

Figure 4.16: EDX spectrum, Selected Areas and atomic percentage table, (a) ZnO nanowires (b) ZnO nanorods.

4.3.6 Electrical properties

ZnO nanowires and ZnO nanorods thin films I-V are measured using commercial four-point probe at room temperature is shown in figure4.17, (4.17.a: ZnO nanowires ; 4.17.b: ZnO nanorods).The conductivity values were derived from this measuring is shown in (table 4.10).As we can see from table 4.10 there is a difference in the electrical conductivity for ZnO nanowires and ZnO nanorods thin films this may be mainly due to the difference of charge carriers where it is an insufficient number of charge carriers for ZnO nanowires thin films [10]. It is well known that the thin films microstructure plays an important role in the electrical properties of a semiconductor oxide, we found from MEB results (figure 4.15) the low density and the irregular in size, which increases the grain boundaries that reduce carrier mobility [8].

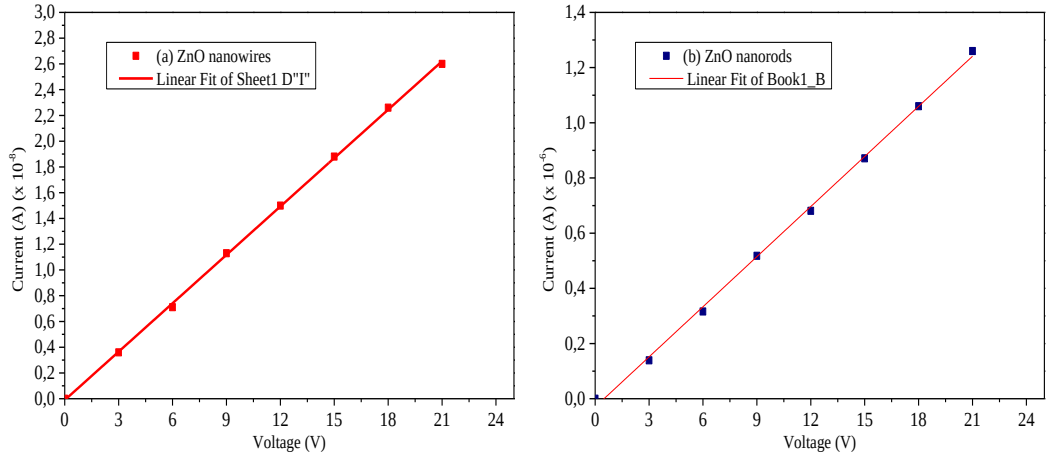

Figure 4.17: I-V measurement for ZnO nanowires and ZnO nanorods thin films.

Table 4.11: Summary of the electrical conductivity of ZnO nanowires and ZnO nanorods thin films.

Sample Name	**Electrical conductivity δ $(\Omega.cm)^{-1}$**
ZnO nanowires	$2x10^{-5}$
ZnO nanorods	$5.77x10^{-4}$

4.3.7 Photocatalytic activity

The nanostructures ZnO; ZnO nanowires thin films forming by zinc acetate dihydrate precursor and ZnO nanorods thin films forming by zinc chloride precursor, deposited on glass substrates used as photocatalysts, were immersed in the MG solution which was irradiated under UV light. Magnetic stirring was maintained in order to homogenize the solution. As can be seen in figure 4.18, the degradation rate of MG increases with UV irradiation time and the high photocatalytic degradation efficiency was achieved at 80 % by ZnO nanorods, with a constant rate K = 0.0134 min^{-1} and half-life time $T_{1/2}$= 51 min for 120 min irradiation time (figure 4.19). However, ZnO nanowires as photocatalyst could degrade only 60 % of MG during the same time of irradiation (figure 4.18) with a rate constant K = 0.0079 min^{-1} and a half-life $T_{1/2}$ = 87 min (figure 4.19). As a result, ZnO nanorods are more suitable than ZnO nanowires as photocatalyst for organic dye photodegradation (MG).

Table 4.12: Summary of the kinetic parameters of ZnO nanowires and ZnO nanorods.

Sample Name	**Degradation efficiency (%)**	**constant rate k (min^{-1})**	**Half-life time $T_{1/2}$(min)**
ZnO nanowires	60	0.0079	87
ZnO nanorods	80	0.0134	51

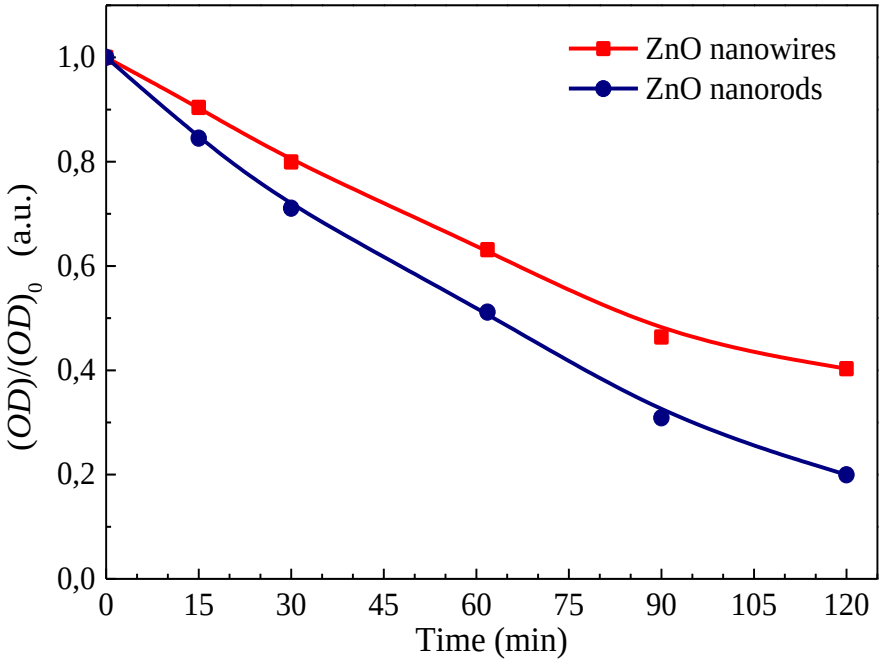

Figure 4.18: Photodegradation kinetic of MG dye by ZnO nanowires and ZnO nanorods photocatalysts

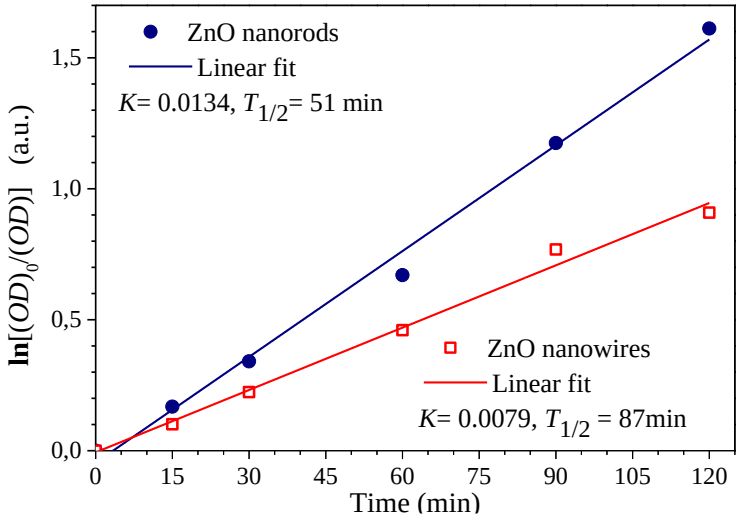

Figure 4.19: ln[(OD)0/(OD)] variation as a function of time for ZnO nanowires and ZnO nanorods photocatalysts.

The difference in the photocatalytic activity of ZnO photocatalysts may be explained by the difference between their nanostructures .Zuo et al. proved that facet effect is an important factor for heterogeneous photocatalysts due to the surface atom arrangement and coordination which intrinsically determine the reactant adsorption on the surface of molecules, surface distribution between photoexcited electrons and reactant molecules [18].The structure, gap energy, lifetime of electron-hole pairs, and $OH^{\cdot}$ radical concentration are fundamental parameters to ameliorate the efficiency of photocatalyst [19].Morphology also acts as a potential factor that influences the final degradation efficiency which was reported earlier [19,

20], and according to Ohtani et al. The degradation phenomenon is explained as follows: the high activity of photocatalyst should satisfy a requirement: large surface area for absorbing dye [12].The explanation that we propose to this phenomenon will be based on the highest of the active surface.Indeed, as shown on the SEM images of ZnO nanorods (paragraph 4.3.4) the appearance of ZnO with smaller size; a huge number of atoms are accumulated on the surface of a catalyst which leads to increase in surface to volume ratio. This property enhances number of active sites and interfacial charge carrier transfer rates thereby achieving higher catalytic activities [21].

4.3.8 Conclusion

From our comparative study (II) between ZnO nanowires and ZnO nanorods thin films, it appears that an enhancement of 20% in the photocatalytic activity of ZnO nanorods thin films was achieved compared to ZnO nanowires thin films. The results indicated that ZnO nanorods thin films are more suitable for water treatment.

4.4 Comparative study between undoped ZnO nanorods and 5% Al doped ZnO nanorods thin films

4.4.1 X-ray diffraction analysis

XRD patterns of undoped ZnO and ZnO: Al thin films nanostructures are shown in figure 4.20.All deposited films diffraction peaks are consistent with the standard data of typical wurtzite structure of ZnO according to the JCPDS 36–1451 [1]. All of the XRD peaks were attributed to ZnO, and no other undesired peaks which results from the secondary phases such as spinels like $ZnAl_2O_4$, Al_2O_3 for ZnO: Al [22].

The highest peak intensity is most appropriated for calculation of some crystallographic parameters which is (002) for both undoped ZnO and ZnO:Al.

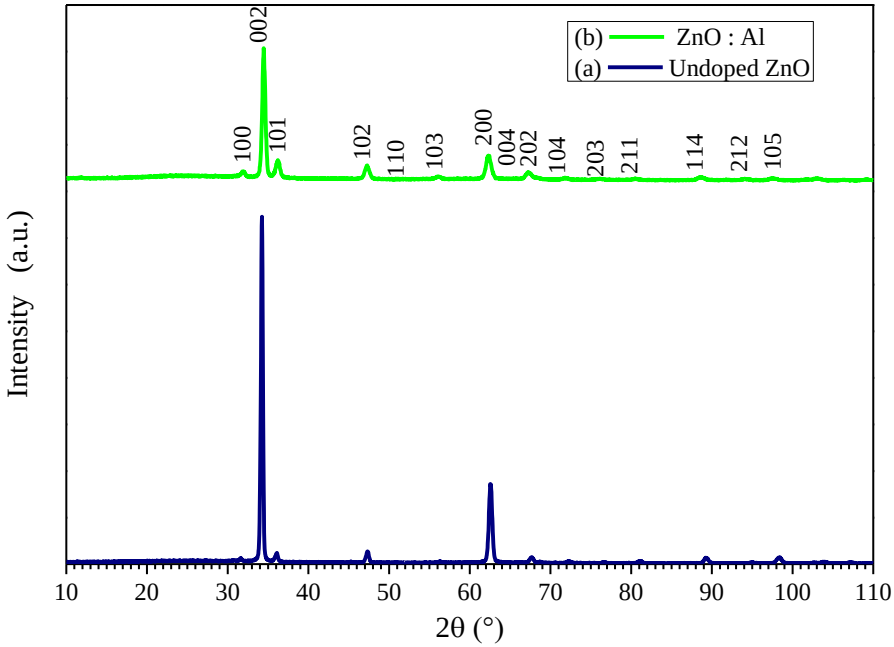

Figure 4.20: XRD patterns of ZnO nanostructures: (a) Undoped ZnO (b) ZnO: Al

Table 4.13: Some crystallographic parameters determined from undoped ZnO and ZnO:Al. XRD data.

Sample label	(hkl) plane	FWHM (°)	*D* (nm)	*ε (%)*
undoped ZnO	(002)	0.265	36	0.360
ZnO:Al	(002)	0.32	29	0.44

Table 4.14: The lattice parameters of undoped ZnO and ZnO:Al.

Sample label	Lattice constants (Å)	
	Calculated	**Standard**[23]
undoped ZnO	$a = b = 3.48$ $c = 4.96$ v = 60 Å ^{3}	$a = b = 3.24$ $c = 5.20$ $v = a^2c = 55Å^3$
ZnO:Al	$a = b = 3.76$ $c = 5.22$ v = 74 Å ^{3}	

The XRD peak positions did not change significantly by doping with Al. But, the intensity and width of these peaks changed, which indicated interesting variations in the lattice parameters (i.e. a and c) and the lattice volume (V) (Table 4.14).

The average crystal size for undoped ZnO and ZnO:Al are presented in (Table 4.13). Due to the smaller ionic radius of Al^{3+} (0.053 nm) than that of Zn^{2+} (0.074 nm) [24], the lattice parameters slightly increase with doping this transition metal. This result suggests that the dopants atoms are incorporated in the ZnO lattices with little or no effect on the overall crystal

structure [25], it can be also explained by interstitial or substitution of doped atoms for Zn atoms [26].

4.4.2 UV-Vis spectroscopy analysis

All the obtained thin films were well adherent to the glass substrates and presented the powdery aspect for both undoped ZnO and ZnO: Al thin films (figure 3.4 in chapter3).Optical transmittance spectra for undoped ZnO and ZnO: Al thin films show in figure 4.21 in the wavelength range from 200 to 1100 nm. We found that the Undoped ZnO and ZnO: Al thin films have a low transmission in the visible range and an absence of interference fringes it can be explained by the surface roughness and the presence of more defects [5, 6]. The region of strong absorbance was observed below 380 nm. In this region, the decrease of the transmittance is due to the excitation and the migration of the electrons from the valence band to the conduction band and also to oxygen deficiency [4], this observation is in agreement with the EDS resultsas we shall see in figure (4.25)

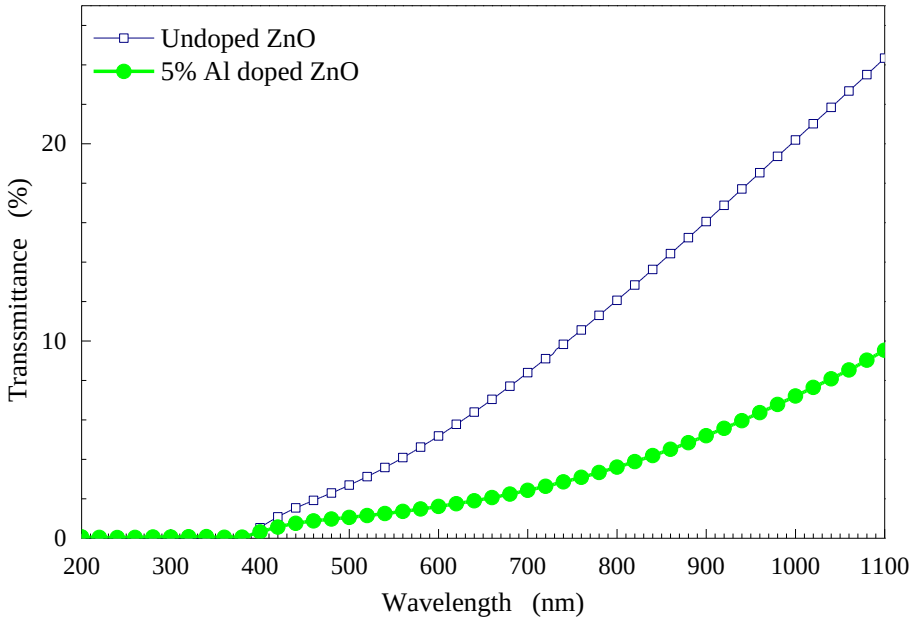

Figure 4.21: Optical transmittance spectra for undoped ZnO and ZnO: Al thin films.

Also as explained in Chapter 2 (paragraph 2.1.5 and paragraph 2.1.6) for the determination of band gap energy and Urbach energy parameter from UV-vis spectra we deduced the band gap energy values Eg = 3.22 eV for undoped ZnO and E_g = 3.01 eV for ZnO:Al. These values are somewhat smaller than the bulk value for ZnO equal to 3.3 eV (Table 4.15) [17]. Also, the low Urbach energy parameter, deduced for undoped ZnO (E_{Urb} =186 meV), can be ascribed to less defects compare with ZnO:Al (E_{Urb} =537 meV) (Table 4.15) [5].

Table 4.15: Optical data of undoped ZnO and ZnO: Al.

Sample Name	E_g (eV)	E_{Urb} (meV)
undoped ZnO	3.22	186
ZnO:Al	3.01	537

4.4.3 Optical profilometer analysis

Three-dimensional optical profilometer images of (a) undoped ZnO and (b) ZnO:Al thin films surface morphology are displayed in figure 4.22. All thin films show homogenous grain distribution characterized by columnar growth perpendicular to the substrate. Furthermore, the films exhibit different surface topographies, which seem to be dependent on the non-uniform films thickness this observation is in agreement with the SEM cross section images morphology results (paragraph 4.4.1).

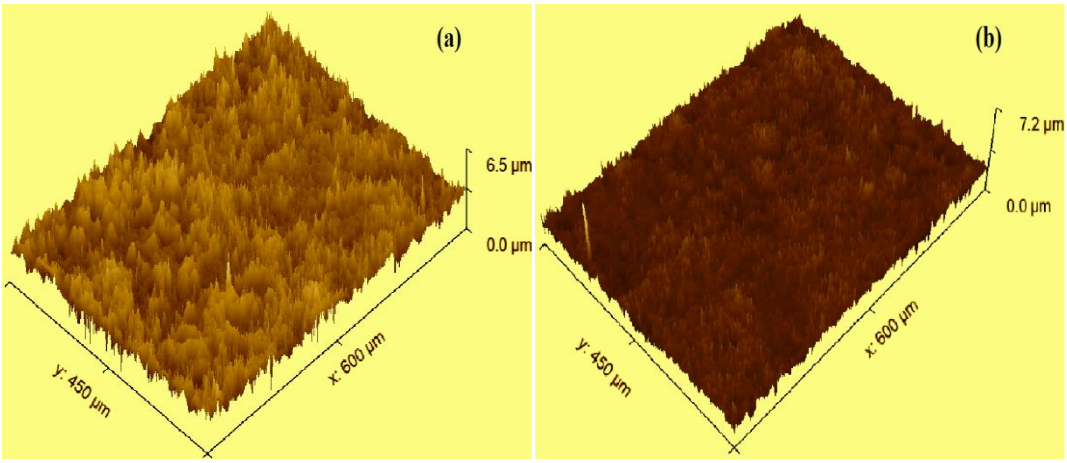

Figure 4.22: Three-dimensional (3D) topography images of (a): undoped ZnO and (b): ZnO: Al thin films.

The root mean square roughness (RMS) and Mean roughness (Ra) were deduced from these images and their values are shown in Table 4.16.

Table 4.16: Morphological parameters for undoped ZnO and 5% Al doped ZnO thin films.

Sample Name	RMS roughness (nm)	Mean roughness Ra (nm)
undoped ZnO	486.3	383.6
ZnO:Al	361.3	272.9

The decrease in root mean square (RMS) and average roughness (Ra) of the ZnO:Al samples (Table 4.16) can be primarily attributed to the presence of Al particles. This is supported by the SEM images, which show the presence of small-sized Al particles (paragraph 4.4.1).

4.4.4 Electron spectroscopy (SEM) analysis

The morphological arrangement of sprayed ZnO:Al thin films were examined using scanning electron microscopy.

Figures 4.23 (a-b-c) show SEM images of ZnO:Al top surface at different magnifications including (x250, x1500andx3000) with 5kV indicate clearly that the morphology of the undoped ZnO thin films Figures 4.23 (a-b-c) is influenced by Al doping (there is appearance of Al particles). We observed that in the presence of Al, the surface morphology of ZnO included many agglomeration compared to those in the undoped ZnO (figure 4.24), also observed a small difference in the particles size between undoped ZnO and 5% doped with Al (figure 4.23 (b and c)).According to Liu.J et al,doping using various transition metals affects the morphology, structure and the shape of semiconductor [25].

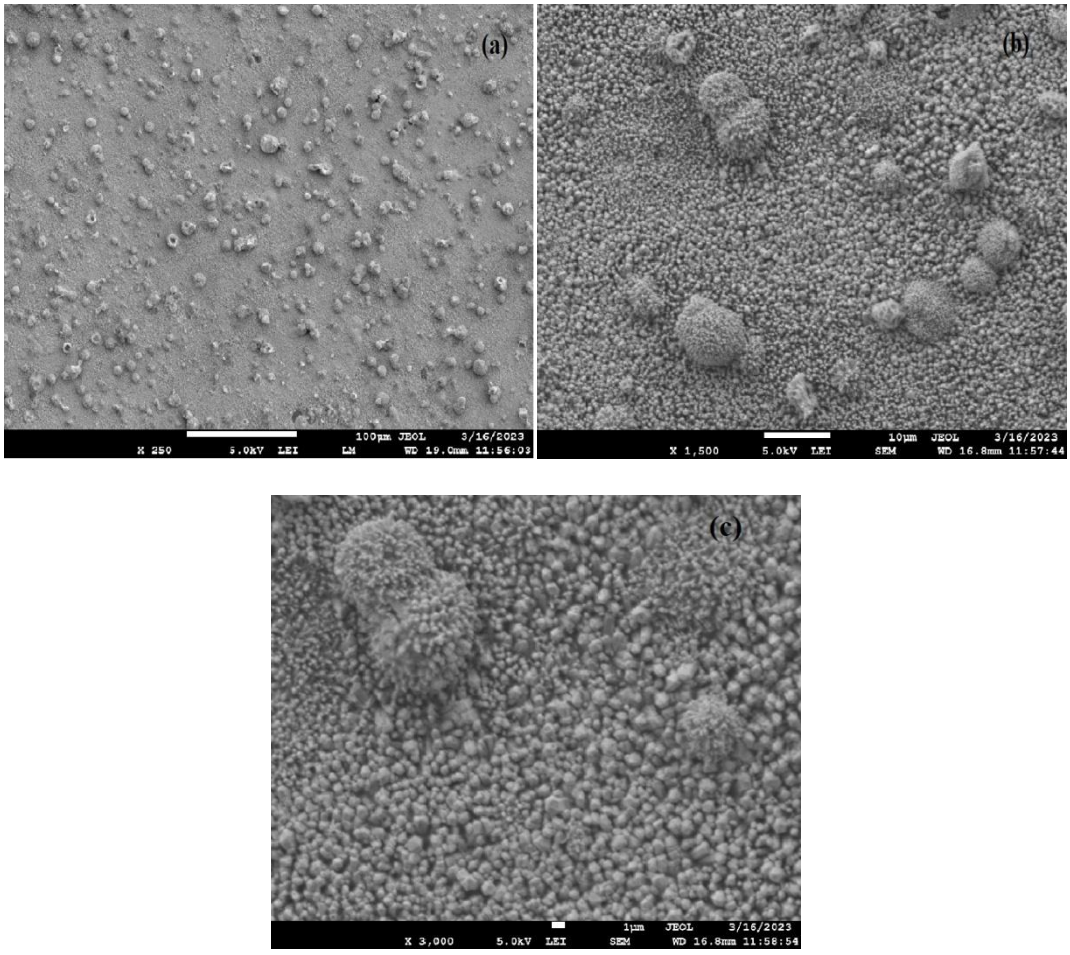

Figure 4.23: SEM images of ZnO:Al thin films at different magnifications

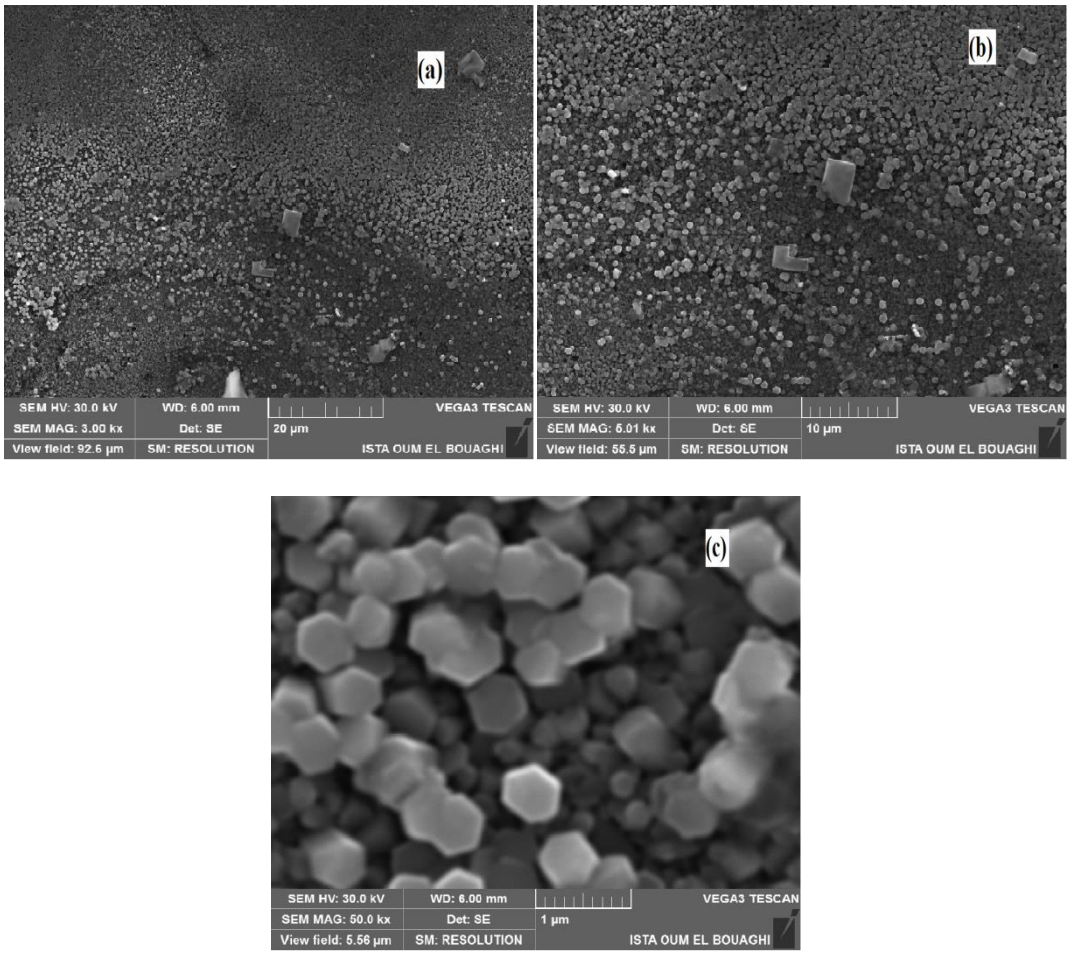

Figure 4.24: SEM images of undoped ZnO thin films at different magnifications.

4.4.5 Energy dispersive spectroscopy (EDS) analysis

In order to know the elemental composition of the undoped ZnO and ZnO: Al thin films, EDS analysis was carried out as shown in the figure 4.25, (4.25.a: undoped ZnO; 4.25.b: ZnO: Al). EDS spectra clearly confirm the existence of Zn (54.86%), O (43.69%) and Al (1.45%) elements in the deposited thin films. These results indicated the successful synthesis of Al doped ZnO thin film using the spray pyrolysis technique. The low Al content in the thin film, relative to the other elements present, suggests that a significant portion of the Al atoms did not incorporate into the ZnO nanostructure. This finding is consistent with the results obtained from X-ray diffraction (XRD) (paragraph 4.4.1).

(a)

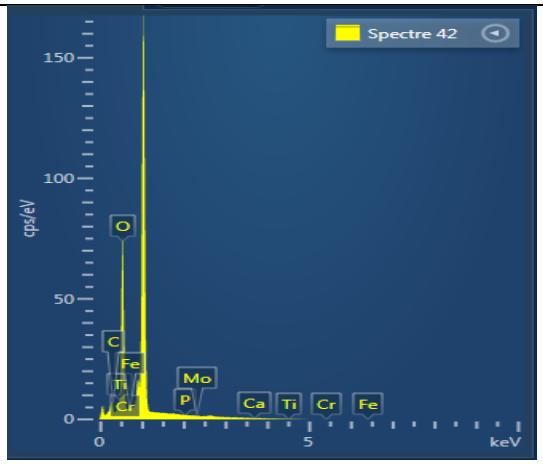

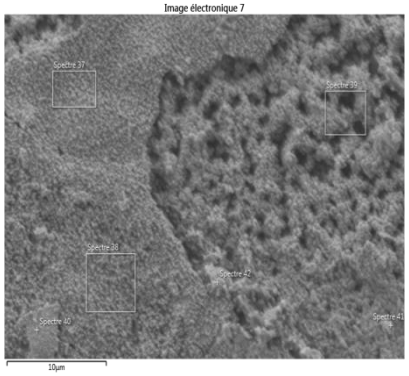

Elements	Atoms %
Zn	54.15
O	45.85

(b)

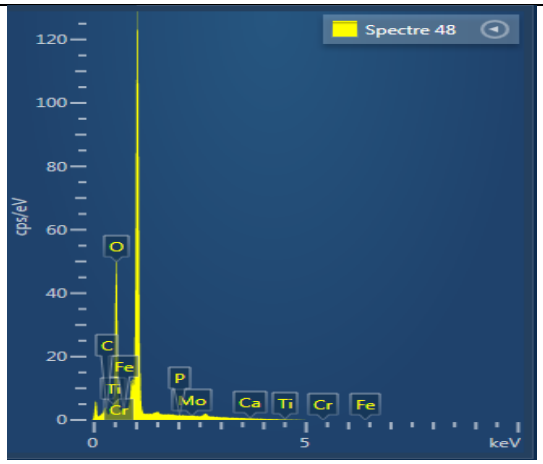

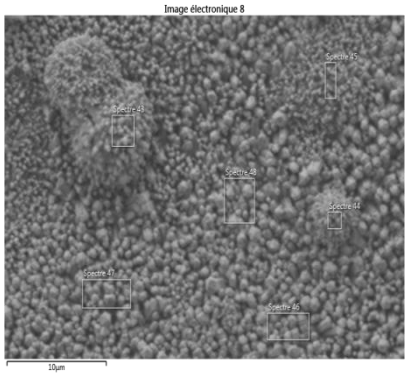

Elements	Atoms %
Zn	54.86
O	43.69
Al	1.45

Figure 4.25: EDX spectrum, Selected Areas and atomic percentage table, (a) Undoped ZnO (b) Al: ZnO thin films

4.4.6 Electrical properties

Undoped ZnO and ZnO:Al thin films I-V are measured using commercial four-point probe at room temperature is shown in figure 4.26, (4.26.a: undoped ZnO ; 4.26.b: ZnO:Al).The conductivity values were derived from this measuring is shown in (Table 4.17). As we can see the electrical conductivity decreases with doping Al particles. This behavior can be justified, on the one hand, by the difference in mobility between holes and electrons, on the other hand,

it is well known that the thin films microstructure plays an important role in the electrical properties of a semiconductor oxide, We found in the MEB results (paragraph 4.4.4) the presence of small-sized grains of Al particles, which increases the grain boundaries that reduce carrier mobility [8].

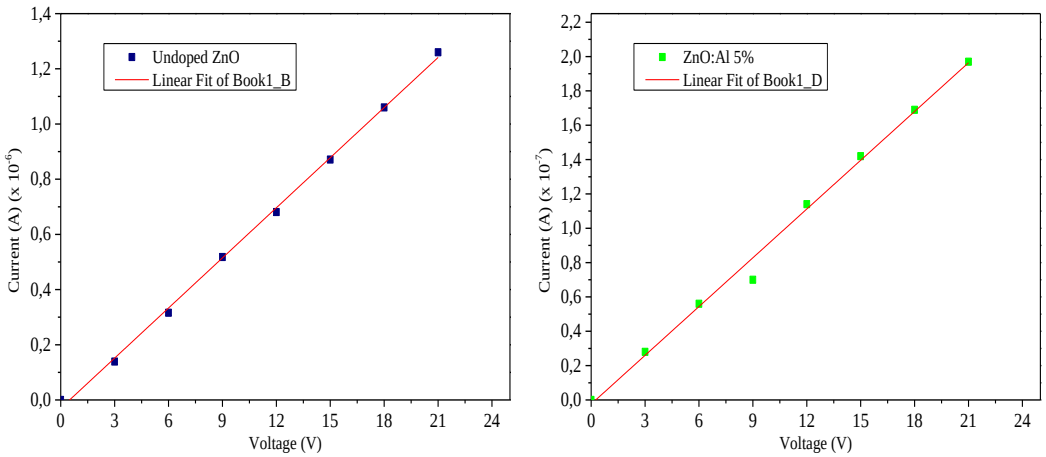

Figure 4.26:I-V measurement for undoped ZnO and ZnO: Al thin films

Table 4.17: Summary the variation of the electrical conductivity with 5% Al dopants element.

Sample Name	**Electrical conductivity δ $(\Omega.cm)^{-1}$**
undoped ZnO	$5.77x10^{-4}$
ZnO:Al	$1.06x10^{-4}$

4.4.7 Photocatalytic activity

UV light photocatalytic activities of the as-synthesized undoped ZnO nanorods and ZnO:Al nanorods catalysts were evaluated by the degradation of MG aqueous solution. Figure 4.27 shows photodegradation of MG as it can be seen, the degradation rate of MG increases with UV irradiation time and the photocatalytic activity is improved when ZnO is doped with Al atoms. ZnO nanorods shows 80% degradation of MG after ≈ 120 min of UV exposure, whereas, doped ZnO sample shows 82% degradation after the same time Figure 4.27. ZnO doped Al samples gave the highest degradation efficiency for this study.

According to Ohtani et al. The degradation phenomenon is explained as follows: the high activity of photocatalyst should satisfy a requirement: large surface area for absorbing dye [12]. The explanation that we propose to this phenomenon will be based on the highest of the active surface.Indeed, as shown on the SEM images for ZnO doped Al samples, there is appearance of Al particles, which is with smaller size and According to Cernuto et al. When the size of the catalyst is smaller, a huge number of atoms are accumulated on the surface of a catalyst which

leads to increase in surface to volume ratio [21]. This property enhances number of active sites and interfacial charge carrier transfer rates thereby achieving higher catalytic activities [21].

The results given above for the degradation of MG, which is the most important for ZnO:Al is confirmed with the calculation of the reaction rate constant k and half-life time $T_{1/2}$(min) (Figure 4.28)(Table 4.18), which is the largest for this study.

Table 4.18: Summary of the kinetic parameters for undoped ZnO nanorods and ZnO:Al photocatalysts.

Sample name	**Degradation efficiency %**	**Constant rate k (min^{-1})**	**Half-life time $T_{1/2}$(min)**
undoped ZnO	80	0.0134	51
ZnO:Al	82	0.0137	50

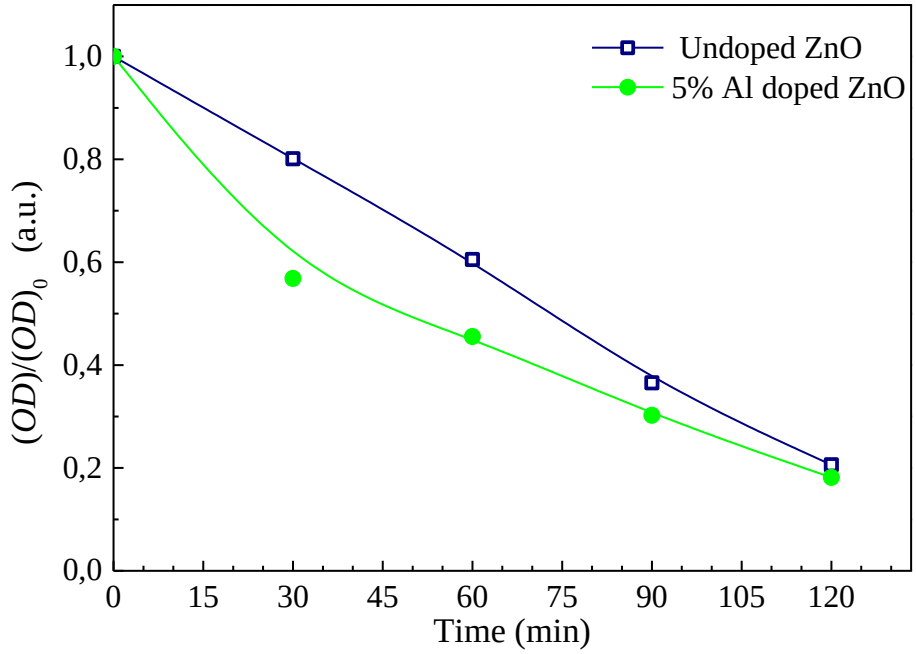

Figure 4.27: Photodegradation kinetic of MG dye by undoped ZnO and ZnO:Al photocatalysts

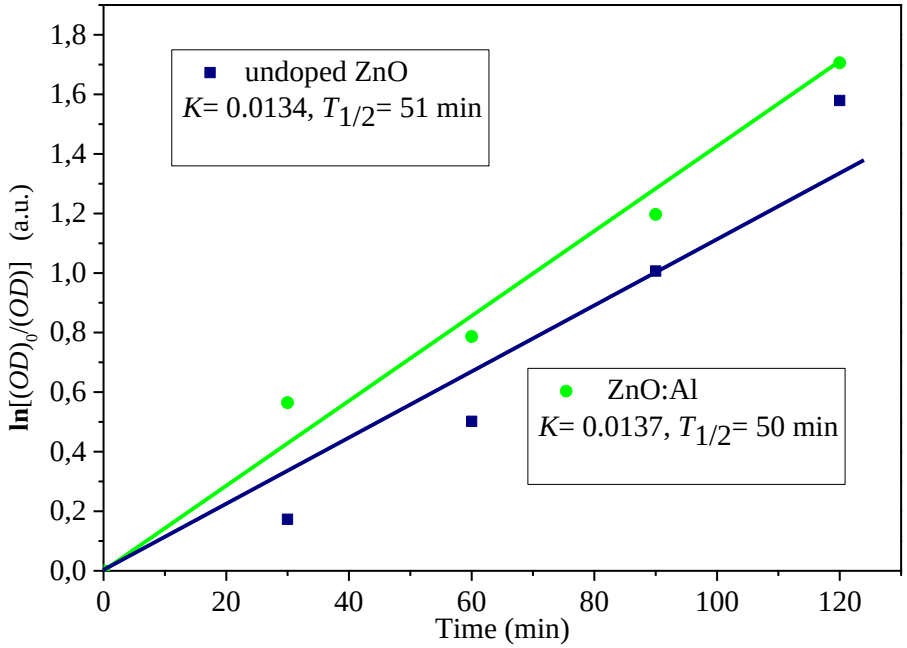

Figure 4.28: Ln $[(OD)_0/(OD)]$ variation as a function of time for undoped ZnO and ZnO:Al photocatalysts.

4.4.8 Conclusion

From our comparative study (III) between undoped ZnO and ZnO:Al thin films, it appears that an enhancement of 2% in the photocatalytic activity of ZnO:Al thin films was achieved compared to undoped ZnO thin films. The results indicated that ZnO:Al thin films are more suitable for organic dye photodegradation (MG).

References of chapter 4

[1] Y-H. Zhang, L.Y.Liang, L.Gong, K. Xie , M. Liu, H. Zhang , S. Fang , Al doped narcissus-like ZnO for enhanced NO_2 sensing performance: an experimental and DFT investigation, Sensors and Actuators: B. Chemical (2019),DOI: https://doi.org/10.1016/j.snb.2019.127489.

[2]H. Mansour, et al, Structural, optical, magnetic and electrical properties of hematite (α-Fe_2O_3) nanoparticles synthesized by two methods: polyol and precipitation, Applied Physics A (2017) 123:787,https://doi.org/10.1007/s00339-017-1408-1.

[3] Avinash V. Rokade, et al, Realization of electrochemically grown α-Fe_2O_3 thin films for photoelectrochemical water splitting application, Engineered Science (2022), DOI: https://dx.doi.org/10.30919/es8d532.

[4] L. Herissi, L. Hadjeris, M.S. Aida, S. Azizi, A. Hafdallah and A. Ferdi, Ni-Doped ZnO Thin films deposited by pneumatic spray pyrolysis, Nano Hybrids Compos, 27 (2019) 21 29 (2019).

[5] T. Prasada Rao, M.C. Santhoshkuma, Effect of thickness on structural, optical and electrical properties of nanostructured ZnO thin films by spray pyrolysis, Appl. Surf, Sci. 255 (2009) 4579 4584 (2009).

[6] L. Hadjeris, L. Herissi, M B. Assouar, T. Easwarakhanthan, J. Bougdira, N. Attaf, M. S. Aida, Transparent and conducting ZnO films grown by spray pyrolysis, Semicond, Sci. Technol. 24 (2009) 035006 (6pp) (2009).

[7] R. Ben Ayed, M. Ajili, A. Thamri, N. T. Kamoun, and A. Abdelghani, Substrate temperature effect on the crystal growth and optoelectronic properties of sprayed αFe_2O_3 thin films: application to gas sensor and novel photovoltaic solar cell structure, Mater Technol. 33 (2018) 769–783 (2018).

[8] L. Herissi, Élaboration et caractérisation de couches minces d'oxydes métalliques destinées à des applications optoélectroniques, Dissertation for the Philosophy Doctor degree, Labi ben M'Hidi University (2016).

[9] D. Perednis, Thin film deposition by spray pyrolysis and the application in solide oxide fuel cells. Ph.D. Thesis, Swiss Federal Institute of Technology Zurich (2003)

[10] Z. Moussa, et al., Zn-Doped Iron Oxide Thin Films Prepared by Spray Pyrolysis Technique and Characterized for Use as an Efficient Photocatalyst for Methyl Green Organic Dye.Nano Hybrids and Composites (2022) , ISSN: 2297-3400, Vol. 35, pp 95-109.

[11] J. Simfukwe, R.E. Mapasha, A. Braun, M. Diale, Exploring the stability and electronic properties of Zn-doped hematite surfaces for photoelectrochemical water splitting, J. Phys. Chem. Solids 136 (2020) pp 109159-9 (2020).

[12] Jr. Ingler, J.P. Baltrus, and S.U. Khan, Photoresponse of p-type zinc-doped iron (III) oxide thin films, Journal of the American Chemical Society, 2004. 126(33): p. 10238-10239 (2004).

[13] B. Ohtani, Y. Ogawa, Sei-ichi. Nishimoto, Photocatalytic activity of amorphous anatase mixture of Titanium (IV) oxide particles suspended in aqueous solutions, J. Phys. Chem. B 101 (1997) 3746–3752, https://doi.org/10.1021/jp962702 (1997).

[14] Fox MA, Dulay MT (1993) Heterogeneous photocatalysis. Chem Rev 93(1):341–357

[15] A. Fujishima, K. Honda, Electrochemical photolysis of water at a semiconductor electrode. Nature (1972) 238(5358):37–38 (1972).

[16] E. Karaköse, H. Çolak, Effect of substrate temperature on the structural properties of ZnO nanorods, Energy 141 (2017) 50–55 (2017).

[17] M. Can Akgun, Y.E. Kalay, H.E.Unalan, Hydrothermal zinc oxide nanowire growth using zinc acetate dihydrate salt,J. Mater. Res. 27 (2012) 1445 1451 (2012).

[18] S. Oktik, Low cost, non-vacuum techniques for the preparation of thin/thick films for photovoltaic applications, Prog. Cryst. Growth Charact.17 (1988) 171 240.

[19] MM. Khan, SF. Adil, A. Al-Mayouf, Metal oxides as photocatalysts. J Saudi Chem Soc (2015) 19 (5):462–464 (2015).

[20] F. Bourfaa, A. Boutelala, M.S. Aida, N. Attaf, Y.S. Ocak, Influence of seed layer surface position on morphology and photocatalysis efficiency of ZnO nanorods and nanoflowers, J. Nanomater. 20201-9 (2020).

[21] G. Cernuto, N. Masciocchi, A. Cervellino, G.M. Colonna, A. Guagliardi, Size and shape dependence of the photocatalytic activity of TiO_2 nanocrystals: a total scattering Debye function study, J. Am. Chem. Soc. 133 (2011) 3114-3119 (2011).

[22] M. Baradaran, F.E. Ghodsi, C. Bittencourt, E. Llobet, The role of Al concentration on improving the photocatalytic performance of nanostructured ZnO/ZnO:Al/ZnO multilayer thin films, J. Alloys Compd. 788 (2019) 289-301 (2019).

[23] G.S. Thool et al., Facile synthesis of flat crystal ZnO thin films by solution growth method: A micro-structural investigation, Journal of Saudi Chemical Society (2014), http://dx.doi.org/10.1016/j.jscs.2014.02.005.

[24] M. R. Islama, M. Rahmana , S.F.U. Farhadb , J. Poddera, Structural, optical and photocatalysis properties of sol–gel deposited Al doped ZnO thin film, Surfaces and Interfaces (2019),https://doi.org/10.1016/j.surfin.2019.05.007.

[25] Liu, J., et al., General strategy for doping impurities (Ge, Si, Mn, Sn, Ti) in hematite nanocrystals. The Journal of Physical chemistry c, 2012. 116(8): p. 4986-4992.

[26] F. Ajala, A. Hamrouni, A. Houas, H. Lachheb, B. Megna, L. Palmisano, F. Parrino, The influence of Al doping on the photocatalytic activity of nanostructured ZnO: the role of adsorbed water, Applied Surface Science (2018), doi: https://doi.org/10.1016/j.apsusc.2018.03.141.

General Conclusion

General conclusion

Undoped ZnO, Al doped ZnO and Fe_2O_3thin films were elaborated by ultrasonic spray pyrolysis and their properties were studied by using various characterizations in order to determine the optimized conditions leading to good quality thin films which can be used in several applications. The investigations were summarized in three different comparative studies: 1st between ZnO and Fe_2O_3 thin films, 2nd between ZnO nanowires and ZnO nanorods thin films and 3rd between undoped ZnO and Al doped ZnO thin films.

The results of the1st comparative study showed that the structure of the thin films was polycrystalline and the as-grown ZnO films have the hexagonal structure (wurtzite type), while the as-grown Fe_2O_3 films have the rhombohedral structure of a hematite Fe_2O_3phase. The crystallite size was found to be 22.88 nm for $Fe_2O_3$and 26.88 nm for ZnO. The lattice parameters of ZnO and Fe_2O_3 were in close agreement with the reported standard data. The UV-Vis spectroscopy analysis showed a low transmittance and the absence of interference fringes due to a high surface roughness. The optical band gapvalues found were E_g = 3.12 eV for ZnO and E_g = 2.10 eV for Fe_2O_3. The optical profilometer images of ZnO and Fe_2O_3 thin films showed homogenous grain distribution characterized by columnar growth perpendicular to the substrate and the films exhibited different surface topographies. The SEM micrographs showed that the deposited Fe_2O_3thin films had spherical shape grains with nanometer size; however the deposited ZnO thin films were composed of nanowiresgrown onto the substrate surface with a low density and irregular sizes.The SEM images of Fe_2O_3thin films cross section morphology revealed the surface roughness and showed that the thickness of the Fe_2O_3 film is heterogeneously distributed which confirms the non-uniformity of thin films deposited by spray pyrolysis technique. The EDS spectra analysis confirmed the formation of the two metal oxides. The electrical conductivity was found to be $9.18x10^{-7}(\Omega.cm)^{-1}$for Fe_2O_3thin films and $4.39x10^{-6}(\Omega.cm)^{-1}$forZnO thin films. The photocatalytic activity was improved in the presence of ZnO photocatalyst which showed 55% degradation of MG after ≈2h of UV exposure, whereas, Fe_2O_3sample showed only39% degradation after 2h.These results led to conclude that ZnO thin films composed of nanowires are more suitable than Fe_2O_3 thin films as photocatalyst for organic dye photodegradation (MG).

The XRD analysis in the 2nd comparative study between ZnO nanowires and ZnO nanorods thin films indicated that the as-grown ZnO thin films were highly c-axis-oriented corresponding to hexagonal (wurtzite) structures indexed by all diffracted peaks (JCPDS NO. 036-1451).The crystallite size of the studied films was found to be 36.32 nm for ZnO nanorods and 24.88 nm

for ZnO nanowires. The UV-Vis spectroscopy analysis showed that the ZnO thin films deposited from zinc chloride (nanorods) had a low transmission of about 30 %and an absence of interference fringes which is due to the surface roughness and the presence of defects. The ZnO thin films deposited from zinc acetate (nanowires) had a higher transmission of about 60 % in the visible range. Theband gap energy values were Eg = 3.22 eV for ZnO nanorods and E_g = 3.23 eV for ZnO nanowires. The optical profilometer images of ZnO nanowires and ZnO nanorods showed homogenous grain distribution characterized by columnar growth perpendicular to the substrate and the films exhibited different surface topographies. The SEM images ofZnO nanorods thin films showed hexagonal nanorods grown onto the whole substrate surface with a high density and which were vertically aligned to the substrate,however the ZnO nanowires were grown onto the substrate surface with a low density and were irregular in size. The EDS spectra clearly confirmed the existence of Zn and O elements and these results indicated the successful synthesis of ZnO with deferent nanostructures. The electrical conductivity was found to be $2x10^{-5}$ $(\Omega.cm)^{-1}$for ZnO nanowires thin films and $5.77x10^{-4}$ $(\Omega.cm)^{-1}$forZnO nanorods thin films. The high photocatalytic degradation efficiency was achieved at 80 % by ZnO nanorods with a constant rate K = 0.0134 min^{-1} and half-life time $T_{1/2}$= 51 min for 120 min irradiation time. However, ZnO nanowires as photocatalyst could degrade only 60 % of MG during the same time of irradiation with a rate constant K = 0.0079 min^{-1} and a half-life $T_{1/2}$ = 87 min. We conclude that ZnO nanorods are more suitable than ZnO nanowires as photocatalyst for organic dye photodegradation (MG).

In the 3rd comparative study, we have investigated the influence of 5% aluminum (Al) transition metal doping ZnO nanorods. We found from XRD analysis that all deposited filmsdiffraction peaks are consistent with the standard data of typical wurtzite structure of ZnO according to the (JCPDS 36–1451) and the XRD peaks were attributed to ZnO and no other undesired peaksfor ZnO:Al. The crystallite size of the studied films was found to be 36.32nm for ZnO nanorods and 29.42 nm for ZnO: Al. The lattice parameters slightly increased with doping. The UV-Vis spectrophotometry analysis showed a low transmission in the visible range and an absence of interference fringes for undoped ZnO nanorods and ZnO:Al which could be attributed to the surface roughness and the presence of defects. Theband gap energy values Eg = 3.22 eV for undoped ZnO and E_g = 3.01 eV for ZnO:Al. The optical profilometer images of undoped ZnO and ZnO:Al showed homogenous grain distribution characterized by columnar growth perpendicular to the substrate and the films exhibited different surface topographies and the decrease in root mean square (RMS) and average roughness (Ra) of the ZnO:Al samples could be primarily attributed to the presence of Al particles. We observed from SEM images

that in the presence of Al, the surface morphology of ZnO included many agglomerations compared to those in the undoped ZnO also observed a small difference in the particles size between undoped ZnO and 5% doped with Al. the EDS spectra confirmed the existence of Zn (54.86%), O (43.69%) and Al (1.45%) elements in ZnO:Al deposited thin films. These results indicated the successful synthesis of Al doped ZnO thin film using the spray pyrolysis technique. The electrical conductivity was found to be $5.77x10^{-4}$ $(\Omega.cm)^{-1}$for Undoped ZnO nanorods thin films and $1.06x10^{-4}(\Omega.cm)^{-1}$for ZnO: Al thin films. ZnO nanorods shows 80% degradation of MG after ≈120 min of UV exposure, whereas, doped ZnO sample shows 82 %degradation after the same time. ZnO doped Al samples gave the highest degradation efficiency for this study.

Finally, we can conclude that ZnO:Al thin films are more suitable to realize highest degradation efficiency of organic dye photodegradation (MG).

Careful attention can be made to the preparation of different thin films are necessary. This is an ambitious task which is a perspective and will be a continuity of the present thesis.

Base on the obtained results, some suggestions for future work are proposed:

- Detailed investigation of other doped ZnO such as Fe, Mg and Sn dopants for improving their photocatalytic performance
- Investigation of more semiconducting materials prepared by spray pyrolysis such as: SnO_2, TiO_2, MoO_2 and CuO for photocatalytic applications.

Abstract

In the present work, metal oxidesFe_2O_3, ZnO and Al doped ZnO (ZnO:Al) thin films were elaborated by the simple and economic ultrasonic spray pyrolysis (USP) technique and used as catalysts for the degradation of methyl green (MG). For this purpose, the films were deposited on glass substrates using various deposition conditions in order to prepare suitable films devoted to photocatalytic applications. The parameters varied were the oxide type, the precursor nature and doping rate. Their effects on the structural, optical, morphological, electrical properties and on the photo-catalytic activity were studied. The best results were obtained for 5% ZnO:Al thin film leading to82% of MG degradation compared to Fe_2O_3, ZnO nanowires and ZnO nanorods thin films.

Key Words: Thin films; Metal oxides; ZnO; Fe_2O_3; ZnO nanowires; ZnO nanorods; ZnO:Al; Ultrasonic spray pyrolysis; Photocatalytic.

ملخـــــص

في هذا العمل قمنا بتحضير و دراسة اكاسيد معدنية في شكل شرائح رقيقة من Fe_2O_3، ZnO وZnO المطعم بـAl باستعمال تقنية سهلة و اقتصادية و التي تتمثل في تقنية الرش الحراري فوق صوتي (USP pyrolysis spray) لجعلها محفزات لتحلل الميثيل الأخضر(MG).لهذا الغرض حضرت شرائح على ركائز من الزجاج مع تغيير الشروط التجريبية من اجل إيجاد أفضل الشروط التي تؤدى إلى شرائح ذات خصائص فيزيائية جيدة يمكن استعمالها للنشاط التحفيزي الضوئي. العوامل التي قمنا بتغييرها هي نوعية الأكسيد، طبيعة الملح ونسبة التطعيم و تم دراسة تأثير هذه الشروط على الخواص البنيوية، البصرية، التضاريسية، الكهربائية و على النشاط التحفيزي الضوئي، حيث تم الحصول على أفضل النتائج في حالة ZnO: Al5%تطعيم التي أدت إلى82%من نسبة تحللMGمقارنة بـ Fe_2O_3، ZnO nanowires و ZnO nanorods.

الكلمات الدالة: شرائح رقيقة؛ أكاسيد معدنية؛ZnO ؛ Fe_2O_3 ؛ZnO nanowires؛ZnO nanorods؛ZnOمطعم بـAl؛ الرش الحراري فوق صوتي؛ التحفيز الضوئي.

RESUME

L'objectif de ce travail porte sur l'élaboration et la caractérisation des oxydes métalliques sous forme de couches minces de Fe_2O_3, ZnO, et ZnO dopé Al (ZnO:Al) par la simple et économique technique de dépôt par spray pyrolyse ultrasonique (SPU) utilisables comme catalyseurs pour la dégradation du vert de méthylène (VM). A cet effet, des couches minces ont été déposées sur des substrats en verre avec différentes conditions de déposition en vue d'obtenir des films avec de bonnes propriétés afin d'être appliquées en photocatalyse. Les paramètres de déposition vairés sont le type d'oxyde, la nature du précurseur et le taux de dopage. L'effet de ces paramètres sur les propriétés structurales, optiques, morphologiques et électriques et sur l'activité photocatalytique a été étudié. Les meilleurs résultats sont été obtenus par ZnO:Al avec un taux de dopage de 5% qui a conduit à la dégradation de 82% du VM, par comparaison avec Fe_2O_3, les nanofils de ZnO et les nanotubes de ZnO.

Mots-clés : Couches minces ; Oxydes métalliques ; ZnO ; Fe_2O_3 ; ZnO nanofils ; ZnO nanotubes ; ZnO:Al ; Spray pyrolyse ultrasonique ; Photocatalyse.